FORSCHUNGSZENTRUM ROSSENDORF
Mitglied der Wissenschaftsgemeinschaft Gottfried Wilhelm Leibniz

WISSENSCHAFTLICH-TECHNISCHE BERICHTE
FZR-342
Juni 2002
ISSN 1437-322X

Institute of Safety Research

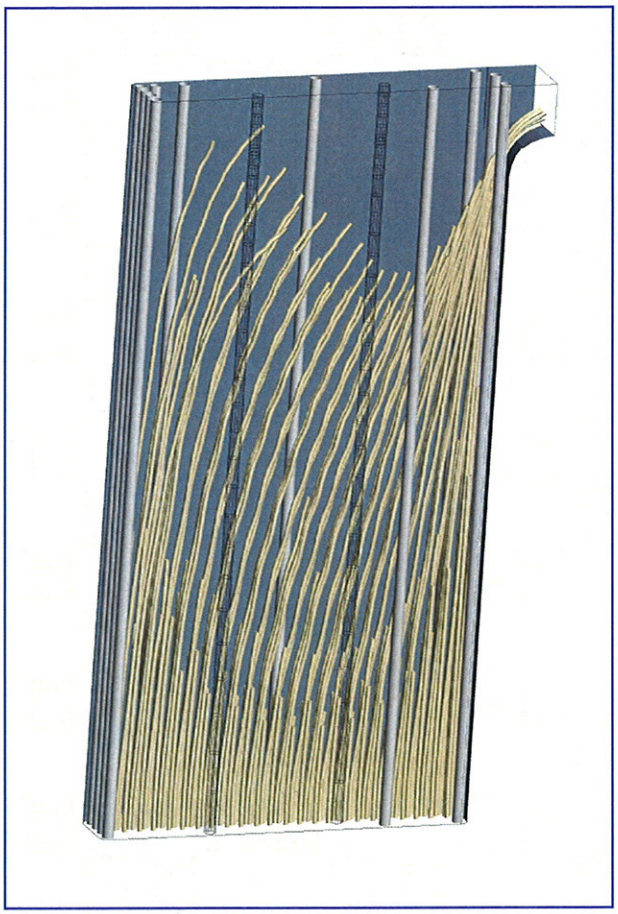

Annual Report 2001

FORSCHUNGSZENTRUM ROSSENDORF
Mitglied der Wissenschaftsgemeinschaft Gottfried Wilhelm Leibniz

WISSENSCHAFTLICH-TECHNISCHE BERICHTE

FZR-342

Juni 2002

Annual Report 2001

Institute of Safety Research

Editors:

Prof. Frank-Peter Weiß

Priv.-Doz. Dr. Udo Rindelhardt

CONTENTS

Preface

The Institute of Safety Research (ISR) is one of the five scientific institutes of Forschungszentrum Rossendorf e.V.. The Forschungszentrum Rossendorf is a member of the scientific association named after Gottfried Wilhelm Leibniz. As such it is basically funded by the Federal Ministry of Education and Research and by the Saxon Ministry of Science and Arts with 50% each.

The work of the institute is directed to the assessment and enhancement of the safety of technical plants and to the increase of the effectiveness and environmental sustainability of those facilities. Subjects of investigations are equally nuclear plants and installations of process industries. To achieve the goals mentioned, the institute is mainly engaged in two scientific fields, i.e. thermal fluid dynamics including magneto - hydrodynamics (MHD) and materials/components safety.

Together with the Dresden Technical University and with the Zittau University of Applied Sciences the ISR represents the East German Center of Competence in Nuclear Technology being a member of the national nuclear association (Kompetenzverbund Kerntechnik). As such the ISR also takes care for the conservation and promotion of expertise in nuclear engineering. That efforts found their expression in the “Karl-Wirtz-Preis” award of the German Kerntechnische Gesellschaft (KTG) to A. Schaffrath for his contributions to the development of a passive heat removal system for advanced BWRs.

At the end of 2001, the institute can look back again at the acquisition of many research grants and scientific contracts with the industry. 29% (4.7 Mio DM) of the total budget stem from such external funding sources with 20% coming from research grants of the Federal Government, the Free State of Saxony and the European Union. 4% of the funding originates from Deutsche Forschungsgemeinschaft (DFG) and 5% from contracts with the industry (see also the attached graphs). The absolute level of external funding is the same as in previous years.

In the reporting period, the ISR performed 9 meetings and workshops with international participation. It is especially worth mentioning the workshop on "Process Control and Condition Monitoring in Chemical Plants" that was conducted for the first time, and the concluding conference of the DFG Innovationskolleg "Magneto-Hydrodynamics of Electrically Conducting Fluids".

It also belongs to the scientific and technological successes of the institute that the construction of our new two phase flow test facility TOPFLOW has well progressed. In particular, the reconstruction of the building and the mounting of the technological part could almost be finished, so that the installation of the control and instrumentation system can be started in the beginning of 2002. TOPFLOW is to strengthen the national and international position of the ISR in the field of two phase flow modeling. The work is substantially supported by a project granted by the coordinating unit for reactor safety research of Bundesministerium für Wirtschaft (BMWi).

At the ROCOM test facility (Rossendorf Coolant mixing facility), a large series of experiments was performed dedicated to coolant mixing phenomena in PWRs during boron dilution and cold water transients. CFD models were validated against those experiments and

a so called semi-analytical mixing model was developed. By coupling that semi-analytical model with the DYN3D reactor dynamics code it could be shown that a shut down reactor gets re-critical when a plug of 36m^3 deionated water enters the core after switching on the first main coolant pump. However, that deionated plug does not lead to non-allowed high coolant pressure or fuel temperatures.

The analytical method of neutron small angle scattering was applied to irradiated VVER pressure vessel material to reveal the micro-structural changes induced by high neutron fluence. In that way, the correlation between the irradiation induced degradation of the mechanical properties and the micro-structural changes could be shown for the first time. These results yield the physical substantiation of the empirically based Russian rules for the dependence of the materials toughness loss on the received neutron fluence.

The behavior of a RPV lower callotte during a severe accident with melt slumping into the lower plenum is studied in 1:10 tests at Royal Institute of Technology Stockholm. At the ISR computational methods were developed for pre- and post-test calculations of those experiments in order to predict the time and mode of RPV failure. The temperature, as well as location, and time of the RPV failure were found in good agreement with the experiment. Two patents resulted from those studies. One of them proposes a creep stool to mechanically support the RPV deformed by creeping, and the flooding of the reactor pit for ex vessel cooling of the melt inside the vessel. Such measures extend the time till RPV failure and offer the possibility for additional accident management procedures that can prevent the RPV melt-through.

The MHD department of ISR was especially successful in 2001. In the framework of the Bundesministerium für Bildung und Forschung (BMBF) initiative "Innovative Gründerla-bore" they were granted an amount of 750,000 DM to be able permanently to create the conditions for applied and market relevant developments that allow young scientists to found their own private technology business.
Moreover, the DFG accepted a common application with the Dresden Technical University and other partners for a so called "Sonderforschungsbereich" (SFB) on the electromagnetic influencing of flows in metallurgy, crystal growth, and electro-chemistry. 5 from 14 single projects arranged in that SFB are headed by the Rossendorf MHD department.
But above all the ISR is proud of the fact that its members G. Gerbeth, F. Stefanie, and Th. Gundrum received the research award 2001 of Forschungszentrum Rossendorf for their work on the experimental prove of magnetic field self excitation in liquid metal flows that was accomplished in close cooperation with the Institute of Physics of the University of Latvia, Riga. The experiments demonstrated for the first time world wide that a magnetic field can emerge from a flow with a high magnetic Reynolds number without any external excitation. That outstanding result was regarded by the American Physical Society to be one of the 3 most important in 2001.

Distribution of funding sources 2001

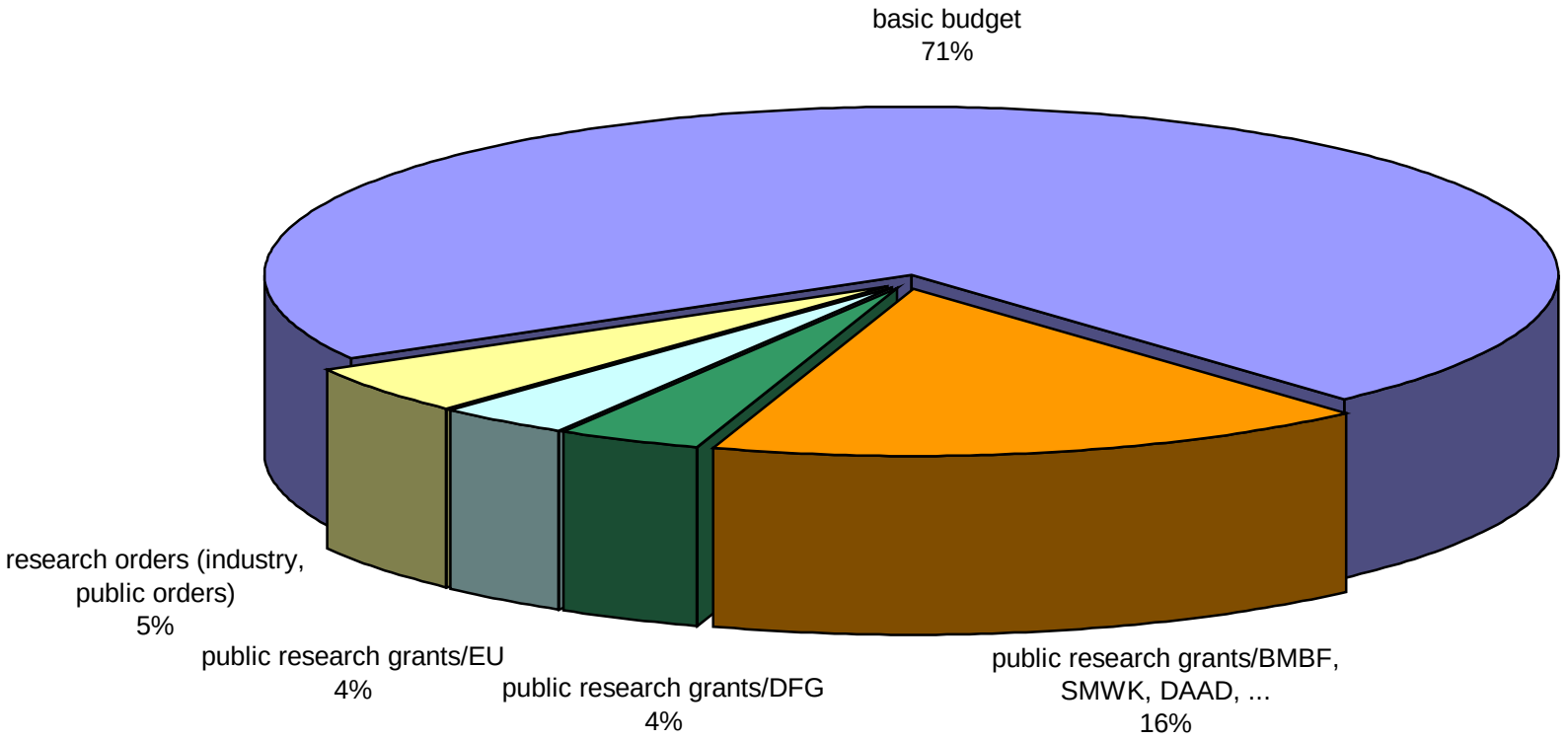

Deployment of funding on the task/projects 2001

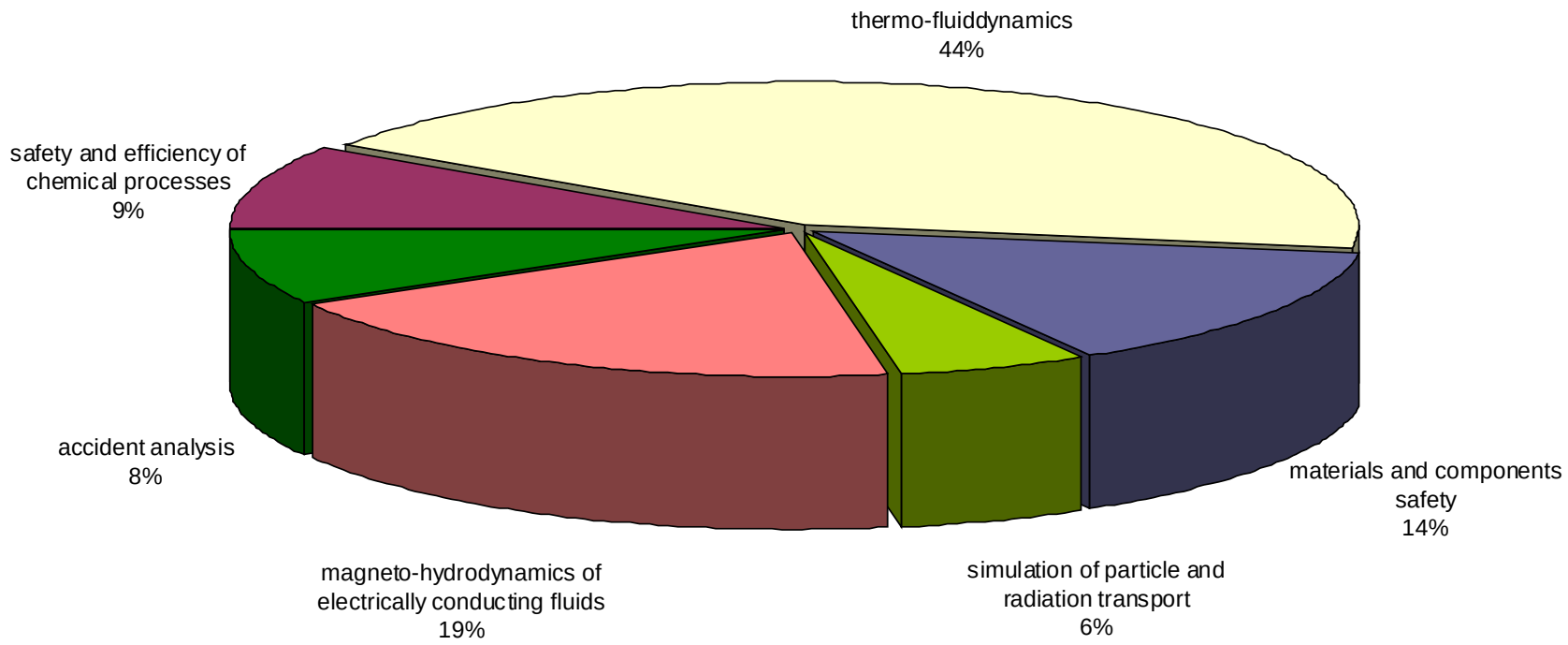

Selected reports

THE INFLUENCE OF HYDROGEN ON THE TOUGHNESS OF REACTOR PRESSURE VESSEL STEELS

Margitta Uhlemann[1], Juergen Boehmert and Gudrun Mueller

1. Introduction

Low-alloyed ferritic steels are, just like high-alloyed austenitic steels, susceptible to H-embrittlement. In a nuclear reactor, corrosion or radiolysis lead to the formation of H-atoms on the inner surface of the reactor pressure vessel and thus to a H-uptake during reactor operation.

In case the structural defects which arise as a result of irradiation become trapping centres for the H-atoms, safety-affected synergisms between irradiation- and hydrogen-embrittlement need to be considered.

Earlier investigations have shown that a H-content larger than 2.5 – 4 ppm effects a clear decrease in toughness and above all causes total embrittlement for high strength steels ($R_m \geq$ 1200 MPa) [1]. After several years of exposure in the pressurized water of the reactor near the core, these critical concentrations are not reached [2].

Pachur [3] developed a hypothesis which postulates an immediate link between radiation embrittlement and the presence of hydrogen. Knowing that the phenomenon is not encompassed by the surveillance programmes, makes it of high relevance with regard to technical safety.
Notwithstanding many findings which contradict Pachur's hypothesis [4], the results described above should be seen as an incentive to reexamine earlier data on a more advanced experimental basis.

The paper reports about new experiments in this field and portray data about hydrogen diffusion behaviour, the solubility of hydrogen and the influence of hydrogen on mechanical properties. These data were taken from experiments on a variety of unirradiated pressure vessel steels under conditions corresponding to those present in pressurized water reactors.

2. Experimental programme

The following reactor pressure vessel steels were investigated:

- A 508 Cl. 3 (Code: JFL)
- A 533 B Cl. 1 (Code: JRQ)
- 15 Xh2NMFAA (Code: WWER) and
- 22NiMoCr 3.7 (Code: A2).

As was one weld material:

- 10XhMFT.

[1] Institut für Festkörperphysik und Werkstoffforschung Dresden

The diffusion of hydrogen was evaluated from permeation experiments after electrochemical charging in two stages: i = -0.5 and -5mA/cm² in 0.1 n NaOH with $5 \cdot 10^{-5}$ mol/l As_2O_3 in the 25 – 80 °C temperature range.

An assessment of the amounts of differently bound hydrogen and their dependence on the temperature and charging parameters was made by means of a hydrogen analyser (LECO-RH 402) or using a mass spectrometer after thermo-desorption at constant heating rates. Besides charging in 0.1 n NaOH (+ As_2O_3), charging in boric acid/KOH - corresponding to PWR-operating conditions - was carried out.

In order to characterize the influence of hydrogen on the strength and toughness of the materials, tensile tests were performed at strain rates of 10^{-6} - 10^{-4}/s in a temperature range of 25 – 250 °C after electrolytic H-precharging and during H-charging at a cathodic flux ranging from –0.5 to –5 mA/cm² in a simulated environment representing the water in a reactor pressure vessel. Finally, H-precharged Charpy-specimens were tested in an instrumented Charpy V-notch test up to temperatures of 50 K.

3. Results and conclusions

The effective diffusion coefficient and the lattice diffusion coefficient are shown in an Arrhenius plot in Fig. 1. The experiments were performed in two steps with different cathodic current. In the first slep the H-diffusion is ingreated by lattice defects which traps the H-atoms (effective diffusion coefficient). After saturation of the potential traps the diffusion is an order of magnitude faster and characterizes the lattice diffusion.

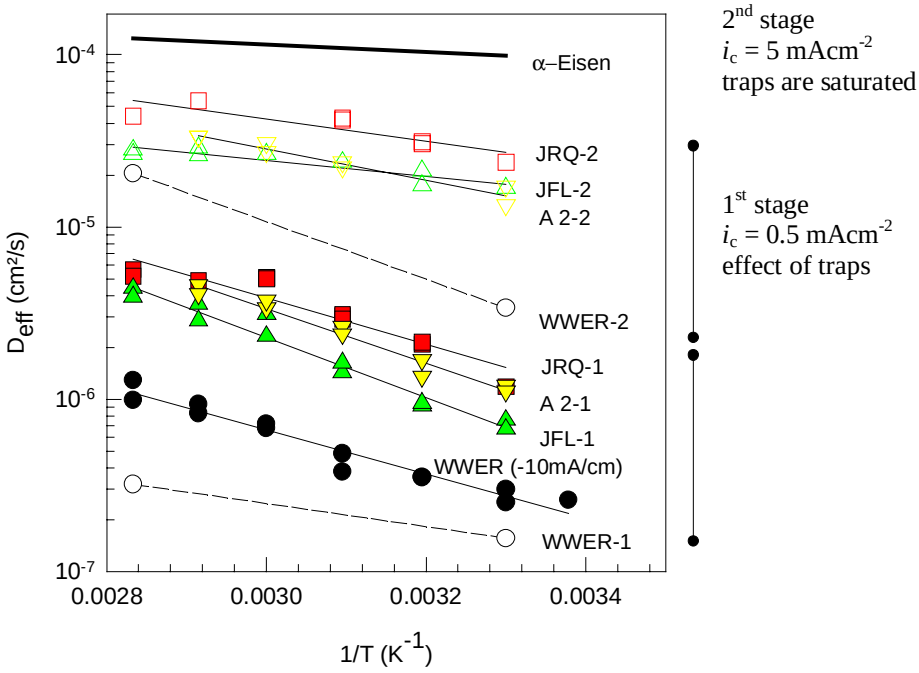

Fig. 1: H-diffusion after electrochemical charging in 2 stages, in 0.1 n NaOH and $5 \cdot 10^{-5}$ mol/l As_2O_3.

Table 1: H-concentration [ppm] in the initial condition and after charging and effusion at room temperature and 250 °C (inaccuracy: ± 0.025 ppm)

Material	Initial condition	Boric acid / KOH i_c = -0.5 mA/cm² solved + trapped RT	trapped 250°C	Boric acid / KOH i_c = -5 mA/cm² solved + trapped RT	0.1n NaOH + As_2O_3 i_c = -5 mA/cm² solved + trapped RT	trapped RT
15Xh2NMFA	0.78	1.14	0.75	1.17	1.82	1.07
A533 - JRQ	0.39	0.64	0.5	0.81	0.81	1.21
A508 – JFL	0.90	1.47	0.74	0.81	1.36	1.36
22NiMoCr3.7	0.75	0.66	0.67	1.3	1.68	1.49

The JFL, JRQ and A2 steels show a diffusion behaviour which is comparable in both permeation steps. In the 15Xh2NMFAA (WWER) steel, however, the diffusion is clearly slower, in the first, as well as in the second permeation step. This may be related to a higher defect concentration and a different alloy composition (higher Cr-content) for this steel. The H-concentration after charging at room temperature and at 250 °C and the effusion at room temperature are given in table 1. Independently of the charging parameters and the material, the H-concentrations vary very little and remain well below the critical concentration of about 3 ppm.

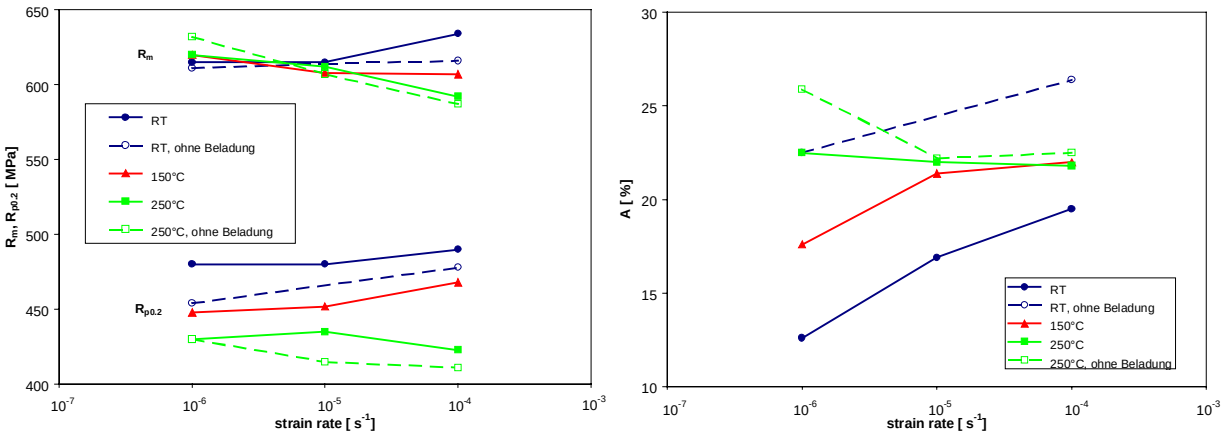

Fig. 2: Ultimate tensile strength R_m, yield stress $R_{p0.2}$ and total elongation A as a function of the strain rate under H-charging with –5 mA/cm² in 0,1 n NaOH + $5 \cdot 10^{-5}$ As_2O_3 for A508 Cl. 3 (JFL)

Accordingly, no or hardly any influence of H-charging on the mechanical properties can be evidenced. A small decrease of the fracture toughness with increasing H-charging can be observed, but is considered negligible. Fig. 2 reveals the dependence of the ultimate tensile strength, the yield stress and the total elongation on the strain rate and temperature for the A508 Cl. 3 steel under in-situ charging at –5mA/cm².
The total elongation remains high and independent of the temperature and strain rate. Similar results were obtained also for the other materials. The temperature-dependence is influenced by strain ageing effects which are also observed in the uncharged condition. For the Charpy V-notch tests at temperatures in the ductile-to-brittle transition range, the results for uncharged and H-charged specimens lie within the material inhomogeneity scatter (Fig.3).

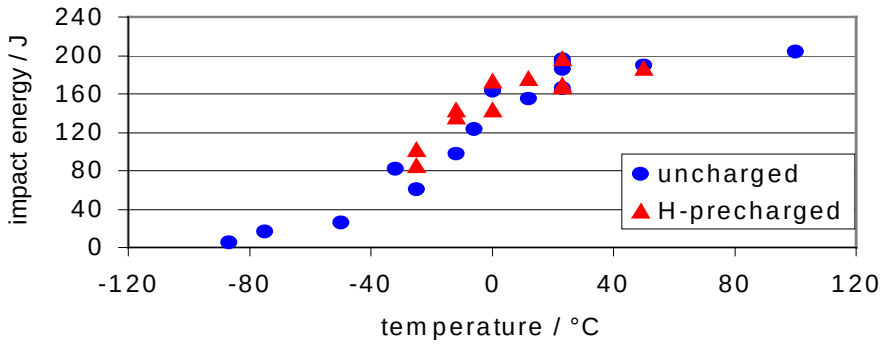

Fig. 3: Charpy V-notch impact-temperature-curve for un- and H-precharged A508 Cl 3 (JFL) specimens

Through the experiments prove an uptake of H under PWR-like conditions of water chemistry and operation temperature, an essential effect on the toughness cannot be observed for reactor pressure vessel steels in unirradiated condition. The H-concentrations remain far below the critical values. Even radiolytically induced H-concentrations under flowing coolant conditions are insufficient to create an effect of embrittlement.

On the basis of the above experiments, however, we cannot exclude that for an irradiated material and/or under stagnating coolant conditions, H-induced or –assisted embrittlement takes place.

An extension of the experimental programme to irradiated RPV steels was therefore be initiated.

References

[1] C. R. Brinkman, J. M. Beeston, The Effect of Hydrogen on the Ductile Properties of Irradiated Pressure Vessel Steels, IN-1359, Nuclear Cooperation, Idako (1970)

[2] K. Splichal, M. Ruscak, J. Zdarek, Intern. J. of Pressure Vessel Piping, 55 (1993) 361

[3] D. Pachur, The Effect of Hydrogen and Oxygen on Irradiation Embrittlement of Reactor Pressure Vessel Steels, paper on the 18th Intern. Symp. on „Effects of Radiation on Materials“, July 1996, Hyaunis (Mass.)

[4] J. Böhmert, M. Uhlemann, Consideration of Environment Degradation of Reactor Pressure Vessel Steels for the Safety Assessment, in EDEM 99, Intern. Conf. on Environmental Degradation of Engineering Materials, Gdansk-Jurata, Sept. 1999, Vol. II, pp. 167

MICROSTRUCTURAL ANALYSIS OF THE REACTOR PRESSURE VESSEL STEEL A533B Cl.1 BY SMALL ANGLE NEUTRON SCATTERING

Andreas Ulbricht, Jürgen Böhmert, Hans-Werner Viehrig

1. Introduction

The microstructures that evolve in the reactor pressure vessel (RPV) steels during neutron irradiation, primarily as a consequence of radiation-enhanced diffusion and defect clustering, are extremely fine-scaled, i.e. in the magnitude of a few nanometres. Small angle neutron scattering (SANS) experiments are able to detect such small clusters and can provide not only qualitative but also quantitative information about the microstructure after neutron irradiation and so help to develop physical understanding of the irradiation-induced ageing mechanisms.

The following paper reports about results of SANS experiments on an A533B Cl.1-type reactor pressure vessel steel, designated JRQ. This steel has been used as IAEA reference steel [1] and shows a high sensitivity against radiation embrittlement. Specimens from this material were irradiated to three different levels of neutron fluences and then mechanically tested by several testing methods. Thus, the investigation allows to realize the dependence of the microstructure and mechanical behaviour on the fluence. Similar investigations were executed on VVER-type RPV steels, which differ from the Western RPV steel design [2, 3]. The comparison of the irradiation behaviour of steels of both provenances is included.

2. Experimental

The investigated material comes from the 1/4 to 3/4 thickness location of the East German contribution of the 227 mm thick rolling plate JRQ (3JRQ 57) made by Nippon Steel Corporation. The material meets the ASTM A533B Cl.1 steel specification. The chemical composition is given in Table 1.

Table 1: Chemical composition of the steel A533B Cl.1 (values in wt.-%, rest Fe).

C	Si	Mn	Cr	Mo	Ni	P	Cu	S	Al
0.18	0.24	1.42	0.12	0.51	0.84	0.02	0.14	0.007	0.02

Charpy V-notched specimens according to the standard or modified for fracture mechanics tests (pre-cracked and side-grooved) and small-size tensile test specimens were machined and irradiated in the Rheinsberg VVER-2 prototype reactor. The reactor is equipped with two types of irradiation channels, core-near high flux channels (neutron flux: $1 - 4 \cdot 10^{12}$ $cm^{-2}s^{-1}$) and core-far surveillance channels of lower neutron flux ($1 - 2 \cdot 10^{11}$ $cm^{-2}s^{-1}$, $E_n > 1$ MeV). The high flux channels have a large cross section and, as the consequence of that, a large radial neutron flux gradient. Considering both the different channel types and the radial gradients, it was possible to group three sets of specimens with three levels of neutron fluences. The irradiation was accompanied by an extended spatial analysis of the neutron fluences based on sophisticated Monte Carlo calculation and neutron-dosimetry measurements. The details of the irradiation and the determination of the neutron fluences are presented in [4, 5].

Mechanical tests after irradiation comprise tensile tests, Charpy impact tests and 3-point bend tests for T_0-determination according to the master-curve concept. Furthermore the Vickers hardness HV 10 was determined. The results of the mechanical testing will be reported elsewhere. Discs of thickness of about 0.8 mm were cut from tested Charpy specimens and used for SANS measurements.

The SANS measurements were carried out at the spectrometer V4 at HMI Berlin [6]. The samples were placed in a saturating magnetic field (B = 1.4 T) perpendicular to the neutron beam direction (wavelength λ = 0.6 nm; beam diameter 7 mm). Two distances of 1.1 and 4 m between the 2-dimensional position sensitive detector consisting of 64×64 cells with a size of 1×1 cm^2 and the sample were adjusted, covering a range of the scattering vector Q from 0.2 to 3.0 nm^{-1}. A comprehensive description of the raw-data treatment formula, including the transmission measurement, background, sensitivity corrections and calibration, is given in [7].

Steel is a polydisperse system, i.e., the particles (defect clusters, precipitates, carbides etc.) in the scattering volume (matrix) have several sizes, shapes and internal structures. Thus, the differential macroscopic scattering cross section separated in a coherent and incoherent term is given by

$$\frac{\mathrm{d}\Sigma}{\mathrm{d}\Omega}(Q) \;=\; a\int_0^\infty D_\mathrm{V}(R)\,R^3 F^2(Q,R)\,\mathrm{d}R \;+\; \left.\frac{\mathrm{d}\Sigma}{\mathrm{d}\Omega}\right|_\mathrm{INC}\quad, \tag{1}$$

where

$$D_\mathrm{V}(R) \;=\; \frac{\mathrm{d}c(R)}{\mathrm{d}R}\left(\Delta\eta^2_\mathrm{nuc} + \Delta\eta^2_\mathrm{mag}\sin^2\alpha\right) \tag{2}$$

is the size distribution function of particles with radius R and volume content c weighted with the scattering contrast $\Delta\eta^2$. Here, nuclear ($\Delta\eta^2_\mathrm{nuc}$) and magnetic ($\Delta\eta^2_\mathrm{mag}$) contributions are distinguished. α is the angle between the scattering vector and magnetization direction of the sample. The value of the scattering vector is

$$Q \;=\; \frac{4\pi}{\lambda}\sin\frac{\Theta}{2} \tag{3}$$

with the angle Θ between incident and scattered beam. $F^2(Q, R)$ is the shape factor, where

$$F(Q,R) \;=\; \frac{3\left(\sin QR - QR\cos QR\right)}{Q^3R^3} \tag{4}$$

and the constant $a = 4\pi/3$ in the case of spherical particles. Generally, $\Delta\eta$, the difference of the scattering length density of the particle and matrix, depends on R if the particles have different internal structures. For particles with known and identical shape $D_\mathrm{V}(R)$ can be estimated by the indirect Fourier transformation method derived by Glatter [8]. If the scattering contrast is known the absolute value of the size distribution relating to the number density or the volume fraction of the particles can be calculated.

The irradiation-induced defect content is

$$\Delta c \;=\; \int_0^\infty \left.\frac{\mathrm{d}c}{\mathrm{d}R}\right|_\mathrm{irr}\mathrm{d}R \;-\; \int_0^\infty \left.\frac{\mathrm{d}c}{\mathrm{d}R}\right|_\mathrm{unirr}\mathrm{d}R\;. \tag{5}$$

The so-called A-ratio, the ratio between the coherent SANS cross section perpendicular and parallel to the direction of magnetization, contains information about the chemical composition or the structure of the particles respectively. It is a function of Q in the cases that there are particles of different types (internal structures) and sizes.

3. Results

The total scattering intensity measured perpendicular to the direction of magnetization is depicted in Fig. 1 for the unirradiated and the three irradiated samples. The dpa-values of 0.010, 0.078 and 0.133 correspond to neutron fluences of 7 to 96 $\cdot 10^{18}$ cm^{-2} [E_n > 1 MeV]. The scattering intensity contains a considerable contribution of incoherent scattering which mainly appears in the nuclear scattering and is caused by the different Fe isotopes. The incoherent magnetic scattering is approximately one order of magnitude lower. By means of the Porod law establishing a dependence of Q^{-4} for the coherent scattering contribution, the incoherent one can be determined and subtracted. The results of this operation are shown in Fig. 2.

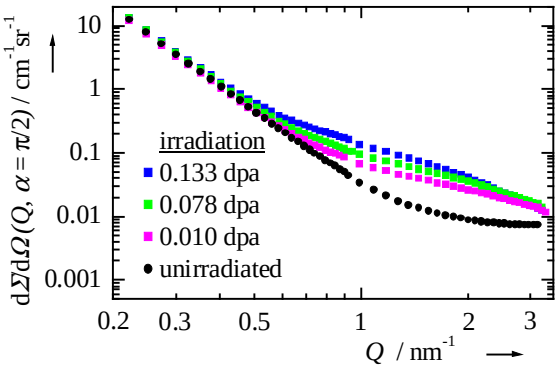

Fig. 1: Measured scattering cross section of different states of the steel A533B.

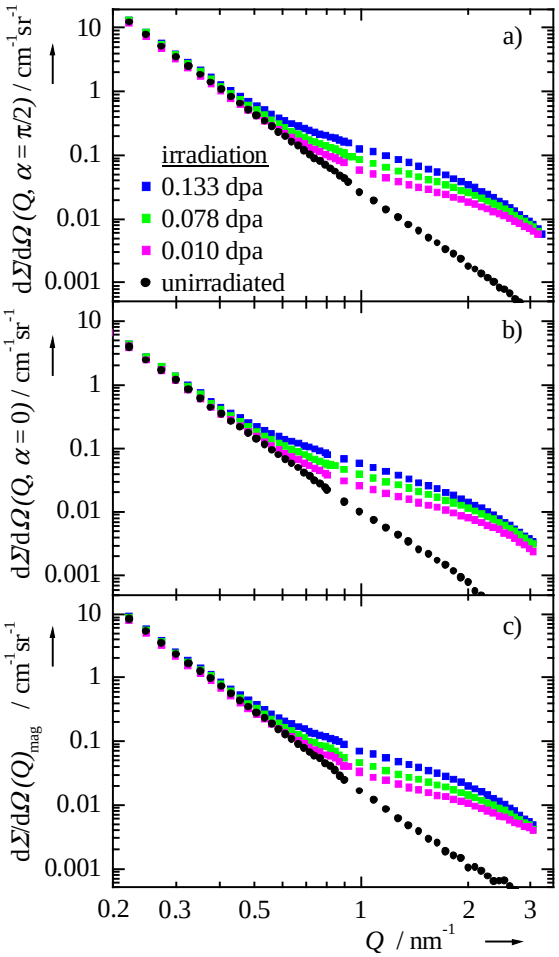

Fig. 2: Coherent SANS cross section of the steel A533B a) nucl.+mag. b) nucl. c) mag. scattering contribution.

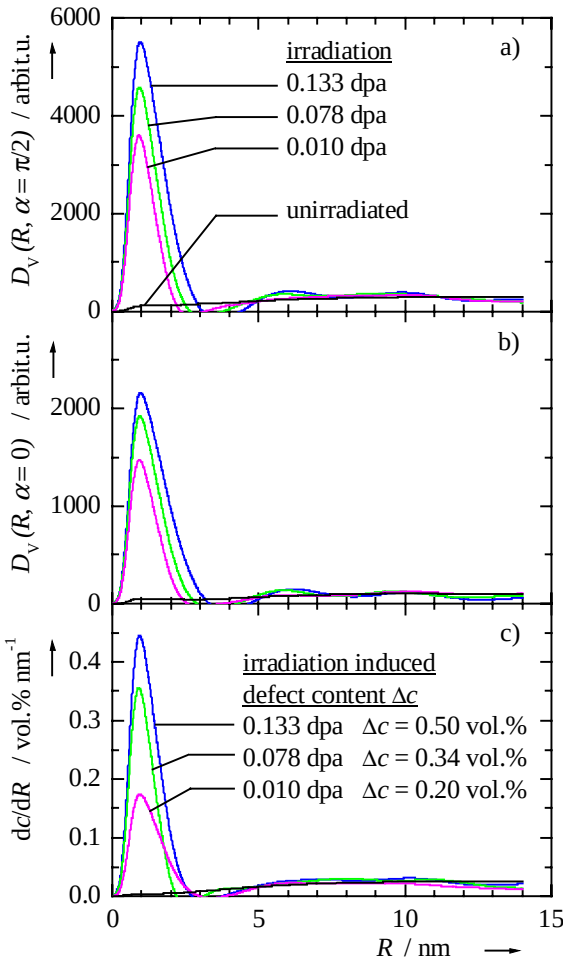

Fig. 3: Volume distribution functions of defects calculated from Fig. 2. a) and b) weighted with scattering contrast c) non-ferromag. defects.

Irradiation enhances the coherent scattering intensity for Q > about 0.4 nm^{-1} in every case. The effect increases with increasing neutron fluence. In the lower Q-range there are hardly differences between the different material conditions. The volume fraction-related size distributions calculated from the coherent SANS cross section curves are shown in Fig. 3. As mentioned above the magnetic contribution provides absolute volume fractions. Both magnetic and nuclear SANS cross section provide similar size distribution functions. In the unirradiated state the size distribution possesses only a weak broad peak for particles with R > 5 nm. This course is not affected by irradiation. Additionally and as a clearly distinguishing mark, the irradiation provokes a sharp peak between 0 < R < 3 nm with the maximum near R = 1 nm. The location of the maximum does not depend on the fluence within the accuracy. Instead, the height of the maximum clearly increases with increasing fluence. Furthermore, in the case of size distribution calculated from the nuclear cross section the range of the peak shifts up to a larger radius. This can be interpreted as indication of irradiation-enhanced growth of the particles. The volume fraction adds up 0.01 % for the unirradiated state and 0.21 %, 0.35 % and 0.51 % for the irradiated condition of dpa-values 0.010, 0.078 and 0.133.

The A-ratio varies between 2.2 and 3.1 in the Q-range from 0.2 to 3 nm^{-1} for all material conditions. In the range between 0.8 and 2.5 nm^{-1}, in which the particles of about 1 nm radius specially scatter, the A-ratio is nearly constant and amounts to 2.2 - 2.4.

4. Discussion

The evolution of nanoscaled microstructural defects with a mean radius of about 1 to 2 nm due to neutron irradiation is also proven for other type of RPV steels and in other investigations [9] and seems to be a characteristic feature independent of composition and initial microstructure.

For the material investigated, there is a really strong effect that approximately linearly increases with the fluence for dpa > 0.01 as shown in Fig. 4. The material has a relatively high Cu content of 0.14 wt.-% and should be specially sensible against neutron embrittlement. At least partly, the high effect is caused by the low irradiation temperature of about 255°C.

The mechanical properties show a comparable dependence on the neutron fluence. This is presented for the Vickers hardness HV 10 and yield stress $R_{p0.2}$ in Fig. 5 as examples. The high irradiation sensitivity as established by the microstructure is also recognizable in the change of the mechanical properties.

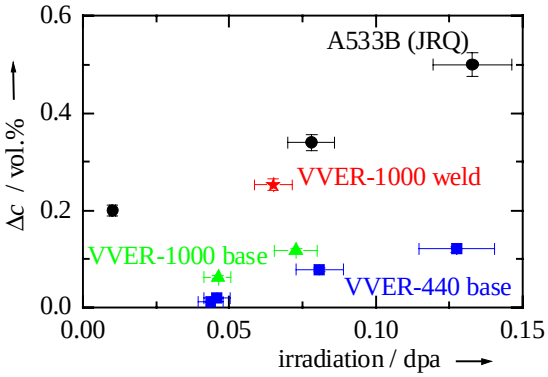

Fig. 4: Irradiation induced non-ferromagnetic defect cluster content Δc versus displacement per atom.

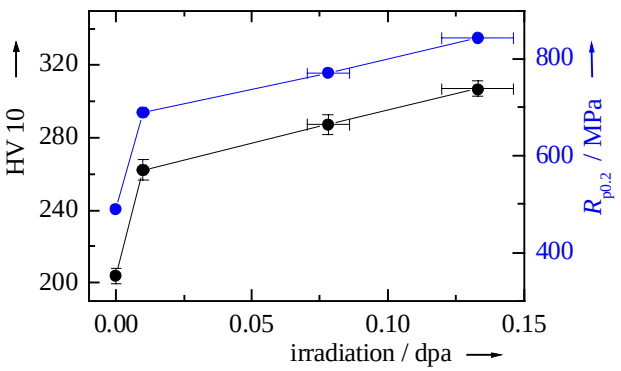

Fig. 5: Vickers hardness HV 10 and yield stress $R_{p0.2}$ versus displacement per atom.

In comparison with the irradiation sensitivity of the JRQ material the VVER RPV steels exhibit a clearly lower sensibility under identical irradiation condition and in spite of comparable Cu contents. This is evident from Fig. 4. Here the volume fractions of the irradiation-induced particles for several types or heats, respectively, of VVER RPV steels are also presented and are considerably lower than the values for JRQ. The Cu content of the VVER heats amounts to 0.10 - 0.13 wt.-%. Only the Cu content of 0.04 % of the VVER-1000 weld investigated is much lower. However, just this material has comparable radiation sensitivity.

The A-ratio of 2.2-2.4 is typical for RPV steels with not too high Cu content (< 0.20 %) and cannot be explained by pure Cu precipitates. It is in the same range as for the VVER steels and rather indicates the formation of vacancy-rich foreign atom clusters or precipitates as found by APFIM investigations [10].

Regarding the mean radius of the irradiation-induced nanoscaled particles instead of the position of the peak maximum there is a weak growth of the particles with increasing fluence for the JRQ material. The phenomenon is not observed at the VVER RPV steels. Particle growth is often found at steels with high Cu content [9] and seems to be connected with the irradiation-enhanced diffusion due to the production of vacancies and interstitials by the neutron impact.

5. Conclusion

SANS measurements prove a high microstructure-related radiation sensitivity of the IAEA reference material designated JRQ. The high sensitivity is confirmed by the change of the mechanical properties. The effect is much higher than for VVER RPV steels. Up to now there has been no explanation for this different response. The existing models do not offer parameters which clearly differ for both types of material. Some details of the results point out to differences in the role of copper. Apparently, copper is important for the nucleation of the irradiation-induced particles although there is no evidence for a higher Cu content within the particles.

References

[1] M. Brumovsky, A. Kruykov, F. Gillemot, V. Levin: Results form the Phase III of the IAEA Coordinated Research Programme „Optimizing of Reactor Pressure Vessel Surveillance Programmes and Their Analysis", Irradiation Embrittlement and Mitigation, Proc. of an IAEA Specialists Meeting, Espoo (Finland), October 1995, IWG-LMNPP-95/5, Vol. II

[2] J. Böhmert, H.-W. Viehrig, A. Ulbricht: Irradiation effects on toughness behaviour and microstructure of VVER-type pressure vessel steels, J. Nucl. Mater. 297 (2001) 251-261

[3] A. Ulbricht, J. Böhmert, H.-W. Viehrig: Beziehungen zwischen Mikrostruktur und Zähigkeitseigenschaften an neutronenbestrahlten WWER-Reaktordruckbehälterstählen, Jahrestagung Kerntechnik 2001, Tagungsbericht, S. 697-700

[4] H. U. Barz, B. Böhmer, J. Konheiser, I. Stephan: Ermittlung der Neutronendosis von bestrahlten WWER-Reaktordruckbehältermaterialien, Forschungszentrum Rossendorf e.V., Wissenschaftlich-technische Berichte, FZR-87, 1995

[5] H.-W. Viehrig, H. U. Barz, J. Böhmert, B. Böhmer: Consideration of Neutron Flux Gradients for Sophisticated Evaluation of Irradiation Experiments, Irradiation Effects and Mitigation, Proc. of a IAEA Specialists Meeting, Vladimir (Russia), September 1997, IWG-LMNPP-97/2, pp. 230-239
[6] U. Keiderling, A. Wiedenmann: Physica B 213 & 214 (1995) 895
[7] P. Strunz, J. Saroun, U. Keiderling, A. Wiedenmann, R. Przenioslo: J. Appl. Cryst. 33 (2000) 829
[8] O. Glatter: J. Appl. Cryst. 13 (1980) 7
[9] G. R. Odette: Radiation Induced Microstructural Evolution in Reactor Pressure Vessel Steels, Mat. Res. Soc. Symp. Proc. Vol. 373 (1995), pp. 137-148
[10] A. Gokhman, J. Böhmert, A. Ulbricht: Contribution to the Determination of Microstruc-tural Parameters from Small Angle Scattering Experiments at Reactor Pressure Vessel Steels, Forschungszentrum Rossendorf e.V., Wissenschaftlich-technische Berichte, FZR-288, Febr. 2000

SCALED VESSEL FAILURE EXPERIMENT ANALYSIS AND INVESTIGATION OF A POSSIBLE VESSEL SUPPORT

Hans-Georg Willschütz, Eberhard Altstadt, Frank-Peter Weiß, and Bal Raj Sehgal [1]

1. Introduction

Scaled coupled melt pool convection and vessel creep failure experiments are being performed in the FOREVER program at the Royal Institute of Technology, Stockholm. These experiments are simulating the lower head of a pressurized reactor vessel under the thermal load of a melt pool with internal heat sources [1]. Due to the multi axial creep deformation of the three-dimensional vessel with a highly non-uniform temperature field these experiments offer an excellent opportunity to validate numerical creep models. A Finite Element model is developed and using the Computational Fluid Dynamic module, the melt pool convection is simulated and the temperature field within the vessel wall is evaluated. The transient structural mechanical calculations are then performed applying a new creep modeling procedure. Additionally, the material damage is evaluated considering the creep deformation as well as the prompt plasticity [2, 3].

Pre- and post-test calculations of at least 4 FOREVER experiments have been performed successfully [4]. Taking into account both - experimental and numerical results - gives a good opportunity to improve the simulation and understanding of real accident scenarios. After analyzing the calculations, it seems to be advantageous to introduce a vessel support which can unburden the vessel from a part of the mechanical load and, therefore, avoid the vessel failure or at least prolong the time to failure. This can be a possible accident mitigation strategy. Additionally, it is possible to install an absolutely passive automatic control device to initiate the flooding of the reactor pit to ensure external vessel cooling in the event of a core melt down.

2. Experimental setup and status of simulation technique

The hemispherical bottom head of the experiments considered here was made of the French RPV steel 16MND5 with an internal diameter of 188mm and a wall thickness of 15 mm (Fig. 1). The applied oxidic melt was a CaO-B_2O_3 mixture (30-70 wt.-%), which has a solidus temperature of T_s = 1250 K. To model the internal decay heat generation special designed heater rods fixed to an internal insulation-reflector-lid are immersed into the melt from the top. To initiate the creep process the vessel is pressurized by Argon.

According to the experience gained in the 3 prior experiments the following issues were related to the pre-test calculations:

- Evaluation of the temperature field, for assessment of the thermocouple readings.
- Expected transient displacement at the positions where the displacement is measured.
- Evaluation of the risk of a prompt plastic failure, due to high temperatures in the welding between hemisphere and cylinder and the cylinder itself, especially at the pressurization beginning.

[1] Royal Institute of Technology, Division of Nuclear Power Safety, Stockholm

- Calculation of the melt level drop due to the expansion of the vessel, so that the critical time of uncovering of the heater is known. And finally:
- Time and location of failure

For the evaluation of the temperature field within the vessel wall the CFD-module FLOTRAN® of the FE-code ANSYS® is used. A 2D-axisymmetric model with appropriate boundary conditions and material properties is developed. A detailed description of the CFD-analysis and the comparison with the experimental results can be found in [2, 3, 4].

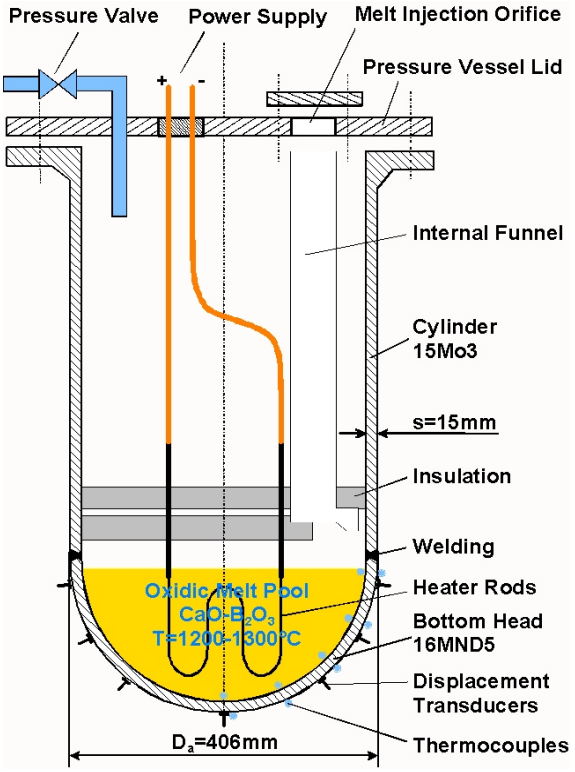

Fig. 1: Principal experimental setup - not to scale

The mechanical 2D-axis-symmetric model of the vessel wall consists of nearly 450 elements with 4 to 8 element layers over the wall thickness. The transient body load due to the temperature field is taken from the CFD analysis. Especially the steep temperature gradient over the vessel wall in the hot focus region must be modeled with a sufficient number of elements over the wall thickness.

Because of the large spatial and transient temperature and stress changes within the vessel wall an advanced approach for the numerical creep modeling has been developed. Usually creeping is described by analytical formulas (creep laws) with a number of free coefficients. The coefficients are used to adapt the creep laws to creep test results performed at constant load and temperature. However, it is difficult to achieve a satisfying adjustment for a wide range of temperatures and stresses with only one set of coefficients. Therefore, a supplementary tool for the ANSYS® code has been developed which allows to describe the creep behavior of a material for different stress and temperature levels independently. Moreover, it is possible to calculate the creep damage and deactivate elements whose accumulated damage is greater or equal to one. A detailed description of this approach can be found in [3]. Fig. 2 shows for example the FE-results for the experiment EC-FOREVER-2 at failure time [4].

3. Analysis and insights to possible accident mitigation measures

Evaluating the observations made in the experiments and in the calculations the following statements can be drawn:

- The creep process is only initiated by the combination of high temperatures (>600°C) and pressure (>1MPa), i.e., at low pressure and high temperature we observe only the reversible thermal expansion, because loads due to the dead-weight of the lower head and the melt pool are negligible, at high pressure and low temperature the material strength is high enough to keep the pressure load.

- If the creep process is initiated, the weak region is the hot focus area, where the highest local creep strain rate occurs, this leads to wall thinning, which accelerates the creep geometrically.
- The overall temperature level and the pressure level influence mainly the failure time, but not the failure position.
- Failure will occur at the position of highest temperatures. Additionally, there is a small influence of the vertical position of the focus region: closer to the cylinder it is more dangerous than at lower positions of the bottom head, this can be understood analyzing the simple vessel formulas for a cylinder and for a sphere.
- Contrary to the hot focus area a large "bowl"-shaped region at the lower head bottom center shows relatively high material strength due to the lower temperatures. This bowl keeps it shape and relocates only vertically downwards. (Some asymmetric movement is possible in reality, but the 2D-Model allows only ideal symmetry.)

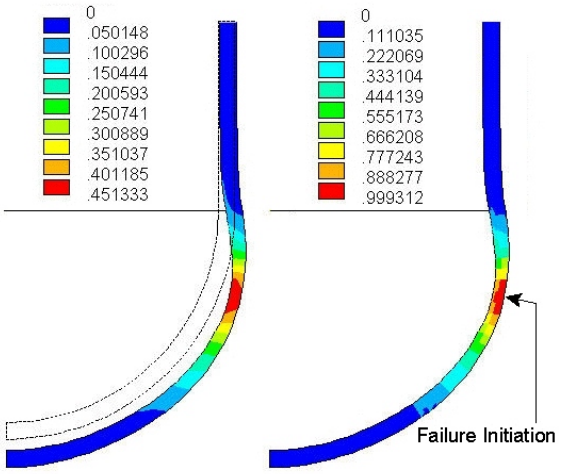

Fig. 2: Local creep strain (left side, max. 45.13%) and damage (right side, max. 0.9993) at the calculated rupture begin after t=4:05h (38kW, 25bar). The expected crack initiation position is indicated.

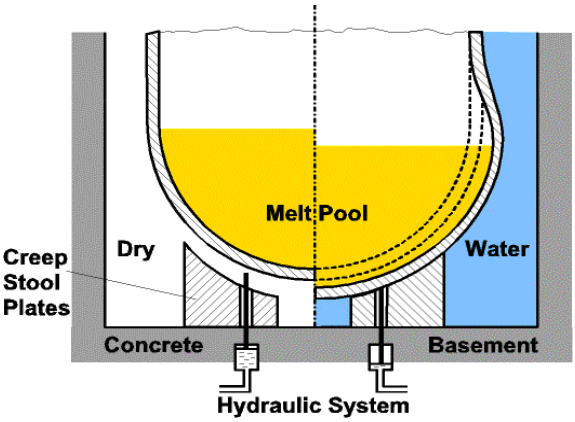

Fig. 3: Possible arrangement for a vessel support in case of a vessel creep. Additionally a passive control device for the initiation of the reactor pit flooding is shown

From these insights one can assume that it should be possible to prolong the failure time or even avoid the failure, if the mechanical loads within the weakest region are reduced. A possible arrangement to ensure this is shown in Fig. 3. On the left the figure shows the vessel at the beginning of a possible in-vessel-retention stage after melt relocation to the lower head. A configuration of 3 or more support plates is positioned between the lower head and the basement. In a top view this "creep stool plate"-configuration would look star-shaped. The plates start at the basement, but at the top end they form a gap to the vessel wall, so that the vertical distance becomes constant between the inner- and the outermost radial position. This should ensure that there are no negative influences during normal operation or other accidents. When the creeping process starts the lower part of the vessel will relocate vertically until the gap is closed. Then a main part of the vertical forces is transferred from the vessel wall to the creep stool plates, as shown on the right side of the Fig. 3. Additionally the force of the downward moving bottom can be used to move one or several vertically arranged rods like shown in the figure. This effect can be used to open a gate or a valve to flood the reactor pit with water, e.g. from the In-Containment Water Storage Tank (IRWST), by means of a hydraulic system or other mechanical devices.

The advantage of this system is that it works absolutely passively and can be realized at rather low cost. The temperature at the vessel wall outside will be decreased by several

hundred degrees and the margin to failure will be increased significantly. The disadvantage are possible steam explosions if the vessel fails anyhow.

4. Dry creep stool calculation at experimental scale

To get an impression about the possible benefits introducing a vessel support like the above described creep stool, it was assumed that there were one in the EC-FOREVER-2 experiment, scaled 1:10, too (cf. Fig. 2). Although the FE-model is 2D, it is reasonable to proceed with this model, because the material strength in the lower part is very high, so the space between each support plate can be managed by the vessel itself.

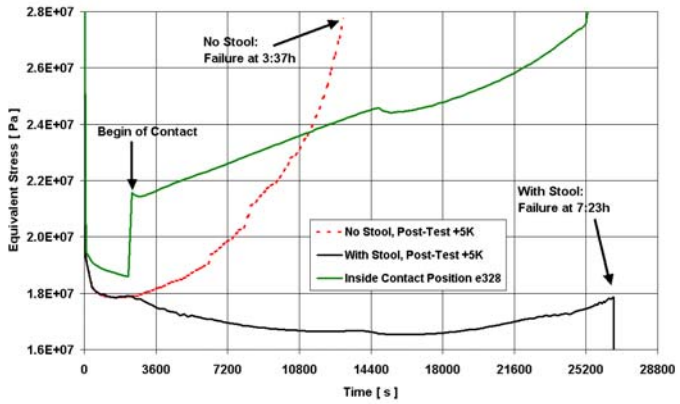

Fig. 4: Development of the equivalent stress in the most damaged element

Assuming a spherical coordinate system at the origin of the bottom head, a radial gap of 7mm is modeled between the vessel wall outside and the creep stool. The modeled creep stool extends in polar direction from 5° to 45°, where 0° refers to the very bottom center. Sliding is allowed, i.e., if the tangential force exceeds the product of the perpendicular contact force and the coefficient of friction, the surfaces move against each other.

All other conditions were the same as in the run shown in Fig. 2. A comparison of the results is given in Fig. 4, which shows the equivalent stress of the most damaged element in both cases. It is interesting to recognize, that the position of the most damaged element did not change, i.e., the expected failure position is the same. The solid red line represents the "no stool"-condition. Failure is calculated after 3:37h (the time scale is referred to t=12,360s in the experiment, i.e., the starting point for all calculations in Fig. 4). The calculation shows a relaxation within the first 30min which is due to the relocation of the stress field. After that the stress increases with some acceleration until failure.

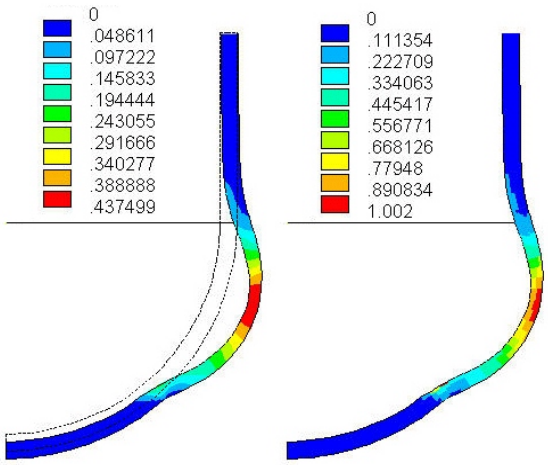

Fig. 5: Creep stool calculation: local creep strain (left side, max. 43.75%) and damage (right side, max. 1.002) at the calculated rupture begin after t=7:24h (38kW, 25bar)

But the calculation entitled "with stool", which represents the behavior if the vessel support is introduced, shows a decreasing stress level after the first 40min. The stress level decreases or keeps relatively constant over 4h, then it increases slowly over 2:20h and after 7:23h the vessel fails. The reason for the stress reduction can be explained by the thin curve in Fig. 4. It shows the equivalent stress in an element at the vessel inside at the uppermost position of contact between vessel and creep stool. It shows clearly the first contact time: after 40min there is a steep increase of the stress. But this element has a much lower

temperature and therefore a much higher strength, so it is not endangered to fail.

According to this simple calculation it can be assumed that a doubling of the failure time is possible, if the stress at the weakest positions of the wall is reduced by a simple vessel support of bottom head center area. Finally the shape, including the local creep strain, and the damage of the vessel are shown at failure time in Fig. 5, which makes the different deformation compared to Fig. 2 obvious.

5. Conclusions

Pre- and post-test calculations of the FOREVER-experiments have been performed. It can be stated that the developed Finite Element Model is quite well validated by this scaled experiments. The failure location and vessel geometry was predicted very well, while there are minor uncertainties concerning the time of failure. Introducing a vessel support facility it is shown that the failure time for this arrangement can be doubled even without flooding the vessel outside, if the lower bottom head is supported by a creep stool, which reduces the mechanical load at the hot focus region just below the melt level surface.

References

[1] Sehgal, B.R., Nourgaliev, R.R., Dinh, T.N., Karbojian, A., 1999, "FOREVER experimental program on reactor pressure vessel creep behavior and core debris retention", Proceedings of the 15-th International Conference on Structural Mechanics in Reactor Technology (SMiRT-15), Seoul, Korea, August 15-20, 1999.

[2] Willschütz, H.-G., E. Altstadt, B.R. Sehgal, and F.-P Weiss, 2001, “Coupled thermal structural analysis of LWR vessel creep failure experiments”, NUCLEAR ENGINEERING AND DESIGN, vol 208, pp 265-282.

[3] Altstadt, E., Moessner, Th., 2000, “Extension of the ANSYS® creep and damage simulation capabilities“, Report, FZR-296, Forschungszentrum Rossendorf, Dresden, Germany

[4] Willschuetz, H.-G., E. Altstadt, F.-P. Weiss, and B. R. Sehgal, 2001, “Pre-test Calculations for the EC-FOREVER-2-Experiment”, Jahrestagung Kerntechnik 2001, Proceedings, pp 187-192, Dresden, Germany, May 2001.

Acknowledgement

The FOREVER experiments are performed under the sponsorship of the ARVI Project of the 5th-Framework Programme of the EU and the APRI Project jointly supported by SKI, Swedish and Finish Power Companies, USNRC, and HSK. This work is supported by the ARTHUR UND AENNE FEINDT-STIFTUNG, Hamburg. This work is also supported by BMWi (project number 1501254).

LEVEL MEASUREMENT SYSTEM FOR BOILING WATER REACTORS

Horst-Michael Prasser, Arnd Böttger, Peter Schütz, Jochen Zschau
Albert Bschor[1], Joachim Henkel[1], Joseph Hubensteiner[1]

1. Introduction

The coolant level in the reactor pressure vessel is a safety parameter of high relevance. In case of boiling water reactors the emergency core cooling injection systems are activated by level signals. Another important task of the level measurement is the prevention of the reactor overfeed. Standard level measuring systems in light water reactors base on the hydrostatic method. The level is deduced from the reading of a differential pressure transducer connected to the reactor pressure vessel by pulse tubes at two different elevations. These systems deliver the so-called collapsed level within the measuring range given by the locations of the lower and upper connections of the pulse pipes to the vessel. In case of two-phase mixture in the vessel the collapsed level is a virtual water level, which would establish in case of a perfect stratification of water and steam. Its calculation from the pressure difference requires a knowledge about the densities of both water and steam in the reactor, which are mostly calculated from pressure and temperature.

Since the differential pressure is measured against a reference water column standing in the plus-line of the differential pressure transducer (reference leg), the system is sensible to failures leading to density changes in the plus-line and/or to the depletion of it. This can happen, for example, as a consequence of evaporation of the water or a release if dissolved non-condensable gases (e.g. radiolysis gases) during a pressure decrease, or of a small leakage at the differential pressure transducer. Unfortunately, there are common-mode scenarios, where these effects can occur in redundant measuring points at the same time. This gave the reason for the German Reactor Safety Commission to issue a recommendation to develop diversified level measuring systems.

Diversified means that the working principle is based on a different physical effect. VGB Power Tech Service asked the Institute of Safety Research to develop a level indication device using an electrical conductivity signal. Laboratory samples of the device were built and tested at an experimental vessel in the Gundremmingen nuclear power station under conditions close to the working parameters at the reactor. The developed system has the potential to maintain function after pressure transients.

2. General requirements

The parts of the measuring sensor, which are in contact with the measuring medium have to withstand the nominal pressure and temperature of the reactor over a long period (typical parameters are 7 MPa, 286 °C). Degradation of the sensor materials must neither lead to a loss of the function nor to a coolant leakage. It was planned to achieve an operation duration of at least 5 years at nominal reactor parameters.

It was furthermore determined to design the level monitor in accordance to the requirements for reactor safety instrumentation. This includes that the device must maintain function during design

[1] Kernkraftwerke Gundremmingen Betriebsgesellschaft

base accidents. The conditions for a qualification as a reactor safety system are described in the KTA-rules 3505 in detail. In particular, the level monitor has to withstand

- an environment of the containment atmosphere during a loss-of-coolant accident (10 Bar, 180 °C, 95 % relative humidity),
- an integral radiation dose of $2 \cdot 10^5$ Gy,
- the mechanical vibration loads during earthquake and airplane crash.

This implied that electronic parts of the measuring transducer cannot be placed inside the containment respectively safety tank. As a consequence great cable lengths (~200 m) were required in order to place the measuring transducer outside the containment. For the sensor, which has to withstand the mentioned conditions, only radiation resistant materials could be used. A self-check procedure indicating the breakdown of the sensor caused either by loss of insulation properties or by signal line breakdown had to be implemented in the measuring transducer. By avoiding on-board processors for the data processing favourable conditions for a qualification according to the KTA rules were created, i.e. complicated qualification procedures for software components were not necessary.

3. Working principle of the diversified level monitor

The task was set to develop a local level monitor for the installation into a standpipe. In most of the boiling water reactors there are standpipes - vertical pipes of approximately 25 - 50 mm inner diameter - which are parallel connected to the reactor pressure vessel. In these standpipes a water level establishes which is characterising the coolant level in the reactor. In most of the cases, the hydrostatic level measuring systems are connected to these standpipes. The diversified level monitor has to deliver a binary information about the presence of water in the standpipe at the axial position of the sensor. If the level in the standpipe is above the sensor, the indicator has to generate a signal LEVEL HIGH, in the opposite case the signal LEVEL LOW has to appear.

The information about the presence of the liquid phase is deduced from an electrical current between two electrodes put into the measuring medium. The conductivity of the coolant is high enough for being detected. Even super-pure water at room temperature has at least a conductivity of about 0.045 µS/cm. Compared to this, the conductivity of steam can be neglected as long as the pressure is still distant from the critical point, which holds for the boiling water reactors in all operational and accidental regimes.

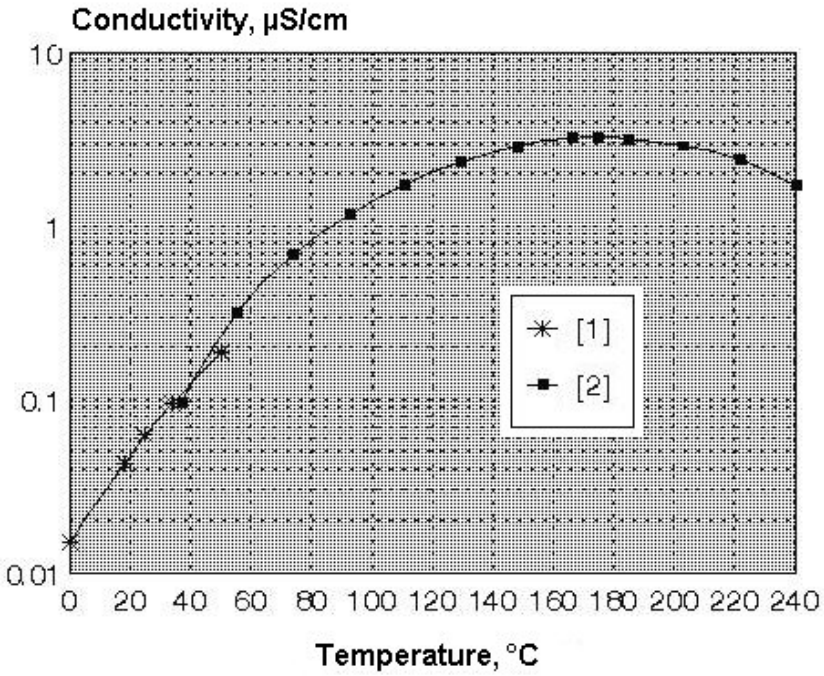

Fig. 1: Conductivity of very pure water over temperature

The main concern is a robust and reliable function of the level monitor with a minimum of false alarms. It was a challenge to find a method to derive the binary level information correctly without the need of an adaptive correction of a threshold over the entire expected range of the water conductivity (Fig. 1). The increase of temperature from room to reactor conditions alone leads to a growth of the conductivity to about 3.4 µS/cm at 180 °C. Additionally, dissolved ions, like corrosion products, may cause a further increase. It was assumed that the level indication has to operate up to a conductivity of 5 µS/cm at 25 °C, which corresponds to approximately 80 µS/cm at high temperature. It must be avoided that a false indication LEVEL HIGH appears, when the level is low in reality. This can happen if it is possible that liquid films (e.g. condensate films) form a connecting contact between the electrodes. In case of high water conductivity the current through thin water films can potentially be higher than the current through plain liquid with low water conductivity in case of high water level. This effect makes it impossible to use a fixed discrimination threshold to transform the analogue current signal into the desired binary output information, i.e. the discrimination level has to be adapted to the instantaneous conductivity of the liquid. The latter had to be avoided for reliability and qualification reasons.

The problem was solved by using a level sensor consisting of two probes mounted on the standpipe from opposing sides. Each probe consists of an electrode, which is insulated from ground and put into the standpipe through a sealed bushing. One of the probes is supplied with a small voltage (~3 V). An electrical current appears at the second one, if the water level is above the sensor position. This current is transformed into the binary level signal. The signal LEVEL HIGH is generated if the probe current in this so-called foreign excitation mode exceeds a certain threshold.

If, on the contrary, the level is below the sensor, there is still the possibility of a liquid layer (e.g. condensate) being in contact with both electrodes in the same time. Nevertheless the current is then zero, since any imaginable liquid layer has a big contact area with the grounded surface of the standpipe and the current from the excited electrode cannot reach the opposite electrode.
To avoid electrolysis effects, such as anodic corrosion or electrode polarization, an alternating voltage has to be applied. Usually, a sinusoidal voltage is used, which makes it difficult to suppress the influence of the high capacitance in cables of the high required lengths. For this reason, the excitation is carried out by a symmetrical, DC free rectangular voltage pulse. The capacitive loads of probes and cables cause a transient behaviour of the current signal. The current is sampled after this transient has settled (Fig. 2). In this way the sampled value reflects only the real part of the complex impedance of the sensor, i.e. the influence of the imaginary part, which contains the effect of capacitance loads, is eliminated.

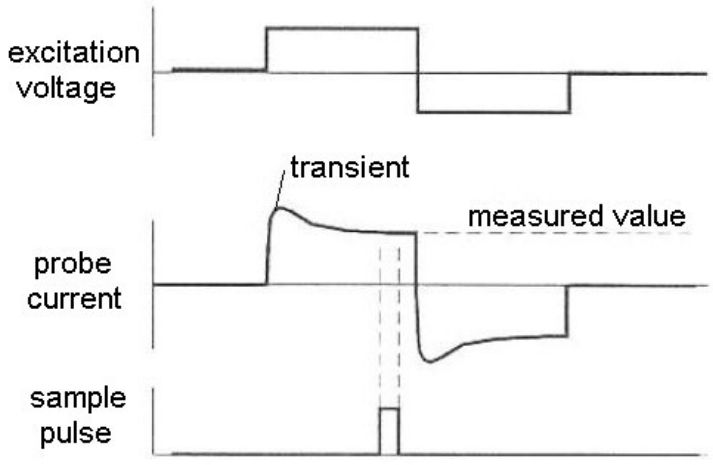

Fig. 2: Rectangular excitation pulse and probe current measurement

Another important property of the measuring transducer is a low-impedance output of the driver cascades. So the excitation voltage is kept constant even if the

insulation of the probe deteriorates, provided that the output impedance is still significantly lower than the insulation resistance. A similar effect is achieved by low impedance inputs of the amplifiers used to detect the current at the receiving electrode, which is not excited. Due to the low impedance the potential of the receiving electrode cannot depart from ground potential. A deterioration of the insulation cannot cause a significant parasitic current towards ground, which would diminish the wanted signal. The low-impedance operation of the probes is therefore a powerful measure to maintain the function of the level sensor as long as possible, when the insulation of the probes is deteriorating. This helps to achieve a high lifetime.

Finally, the self-check is carried out by additionally measuring the current at the excited electrode, too. This operation mode is called self-excited operation [3]. If the obtained signal exceeds a given upper threshold, a binary failure indication is generated (LEVEL MONITOR DEFECT). For the purpose to check the integrity of the signal lines between probes and measuring transducer, the probes are equipped with shunts of about 50 kΩ creating a certain self-exited probe signal. If the line is interrupted, the current decreases and the break is checked by comparing the self-exited signal to a lower threshold.

4. Measuring sensor

The sealed bushing element of the electrode is shown in Fig. 3. The insulation is made of aluminium oxide (Al_2O_3) sintered ceramic. It has the shape of a cylindrical rod with a central orifice for the electrode. At one end of the rod an inner and an outer steel sleeve are soldered to the ceramic surface. These sleeves serve as connecting elements between the ceramic and the body of the probe respectively the electrode.

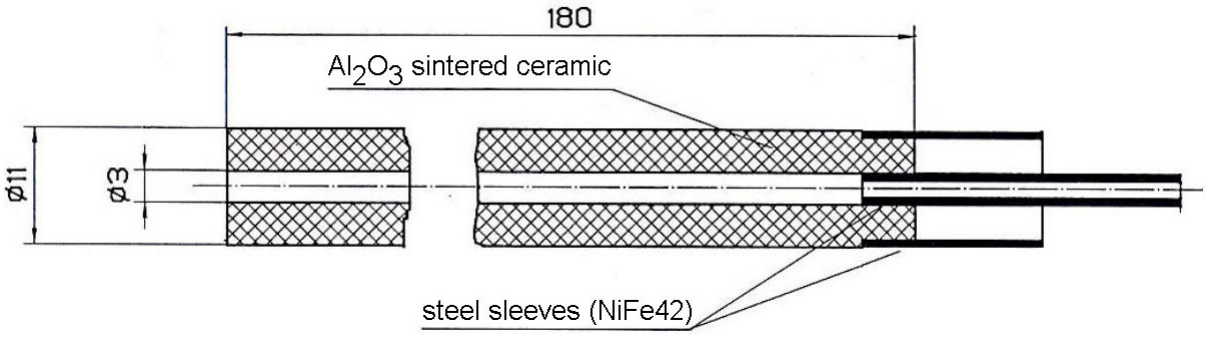

Fig. 3: Sealed bushing made from aluminium oxide sintered ceramic

Before soldering, the surface of the ceramic is plated with a metal layer. Both electrode and end-piece of the probe are laser-welded to the metallic sleeves. The end-piece is welded to the cylindrical body of the probe, both are made of stainless steel. A metal-clad cable is used to contact the electrode. The cable is welded into the back end of the end-piece. The metal-clad cable represents a second barrier against a leakage of the ceramic bushing. A view of the probe is shown in Fig. 4.

Two of the probes form the measuring sensor. They are mounted to the standpipe from opposing sides (Fig. 5). For the test of the level monitor, screwed fittings are used (Swage-Lock fittings). In order to keep the temperature low at the back side of the probe, a heat sink (see Fig. 5) is fixed to the outer surface. In this way, the corrosion attack of the measuring medium to the critical elements (metal-ceramic junctions) of the probes is minimized, since the hot medium can contact the ceramic insulation element only at the side of the mounting into the standpipe [4]. This strategy proved to be efficient to ensure a long lifetime of the measuring sensor.

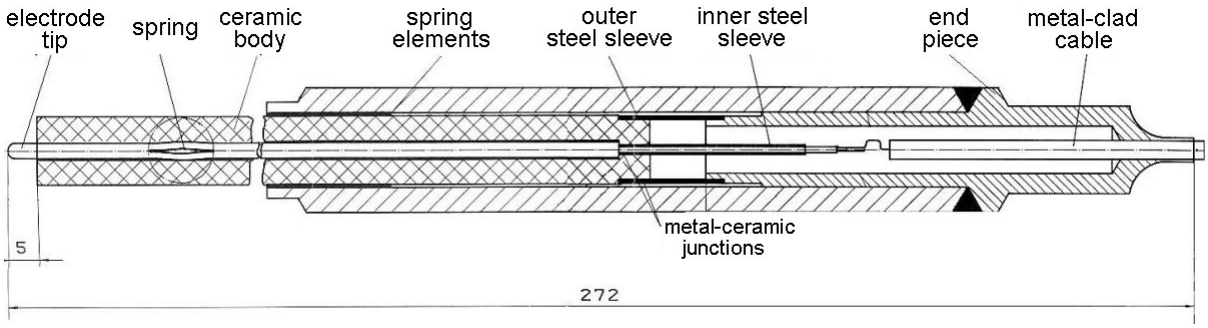

Fig. 4: Probe of the level measuring sensor

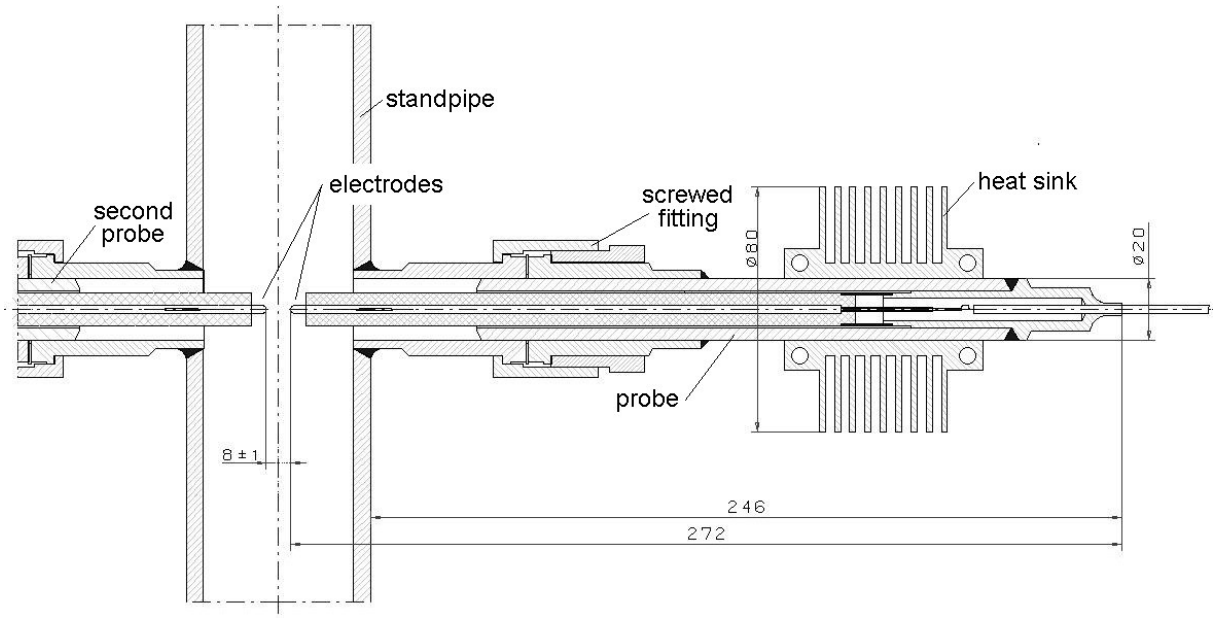

Fig. 5: Measuring sensor mounted on the standpipe

The measuring sensor is equipped with two spring elements preventing the ceramic rod and the electrode from mechanical oscillations in case of vibration loads. This is a precaution against damages due to earthquake and airplane crash loads. Since all elements of the measuring sensor are made either of metallic materials or of aluminium oxide sintered ceramic, the required stability against ionising radiation is maintained.

5. Measuring transducer

A simplified scheme of the measuring transducer is shown in Fig. 6, the most important signals in Fig. 7. Both probes of the measuring sensor are connected to pre-amplifier cascades of identical structure. The cascades consist of two operational amplifiers. The first is switched as an impedance transformer with a logarithmic characteristic. For the self-excited mode, the plus-input of this cascade is supplied with the rectangular pulse of the driving voltage, derived from the signal POS/NEG. Due to the feedback chain of the amplifier an identical pulse appears at the negative input pin and arrives at the electrode of the probe. The current flowing in self-excited mode brings the amplifier out of balance. After subtracting the driving voltage by the second amplifier, the output voltage is proportional to the logarithm of the instantaneous current of the excited probe. This signal is sampled by a sample&hold circuit (S/H) in the moment, when the transient has settled. This happens closely before the successive slope of the excitation voltage, controlled by the

signal S/H PULSES. In the result the signal for the self-check can be found at the output of the corresponding S/H circuit.

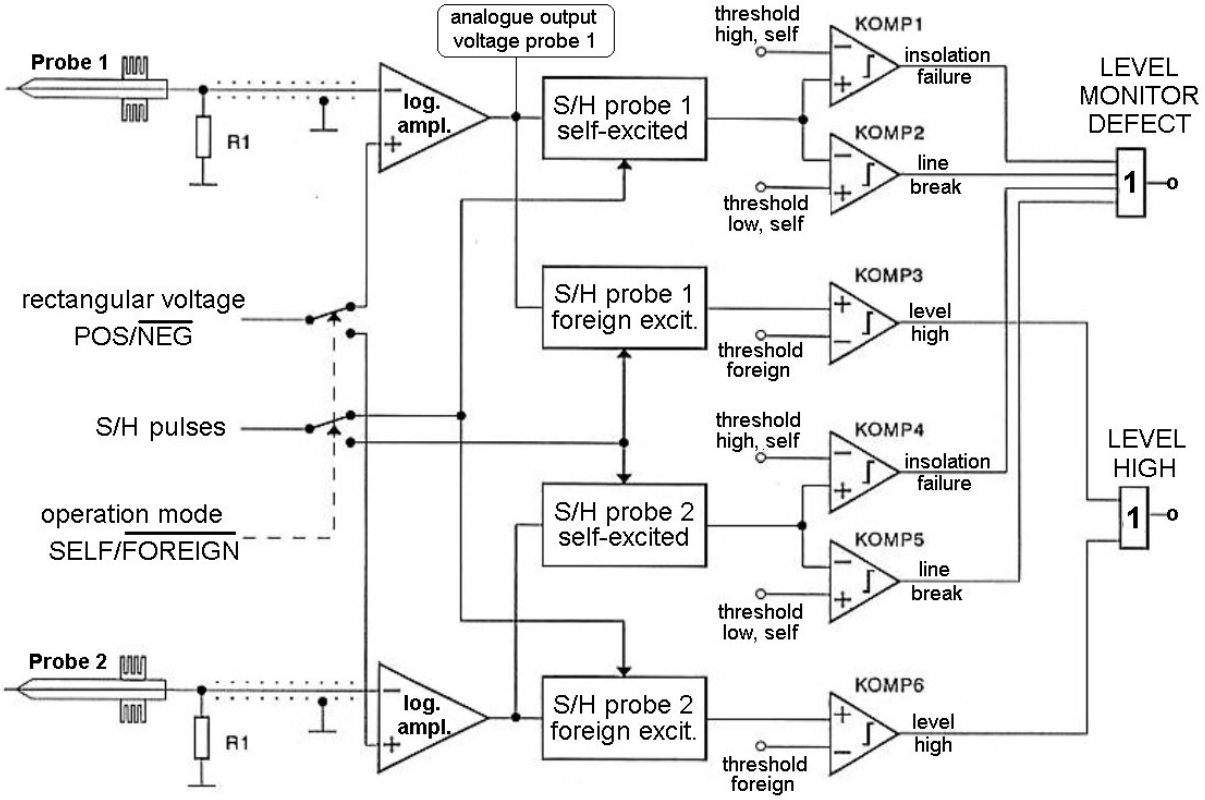

A)

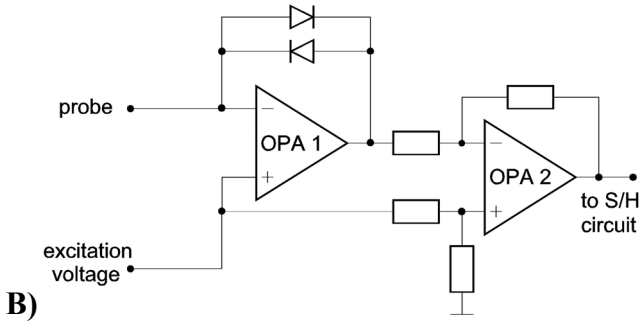

B)

Fig. 6: Simplified scheme of the measuring transducer

A - block scheme
B - logarithmic pre-amplifiers

When the first probe is operated in self-excited mode, the second probe is working in foreign excitation mode. The plus-input of the first cascade of the pre-amplifier is grounded in this case. The voltage at the output of the second amplifier is proportional to the logarithm of the current flowing through the measuring medium. After sampling, this signal is carrying the level information. It is compared to a fixed threshold in the

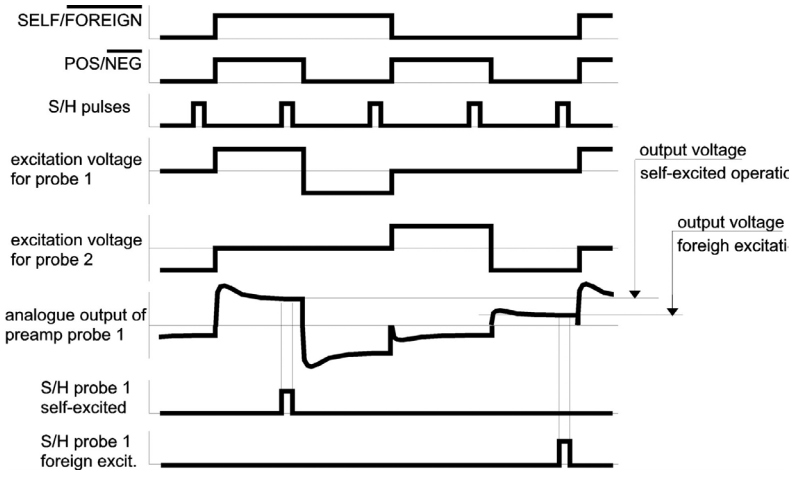

Fig. 7: Pulse diagram of the measuring transducer control

in the comparators COMP3 and COMP6. If the threshold is exceeded, the signal LEVEL HOGH is generated.

The operation mode of the two probes of the level sensor is periodically changed by the control signal SELF/ FOREIGN. There are in total four S/H circuits, two for each probe. One for each probe is activated during the self excited operation period of the corresponding probe, the second is activated during the foreign excitation period. In this way, both probes undergo the self-check. The signal LEVEL MONITOR DEFECT is generated by comparing the self excited signal with an upper and a lower threshold. The comparators COMP1 and COMP4 are responsible for the insulation check. COMP2 and COMP5 are detecting the line break. The signal LEVEL MONITOR DEFECT is generated if at least one of the four self test checks fail.

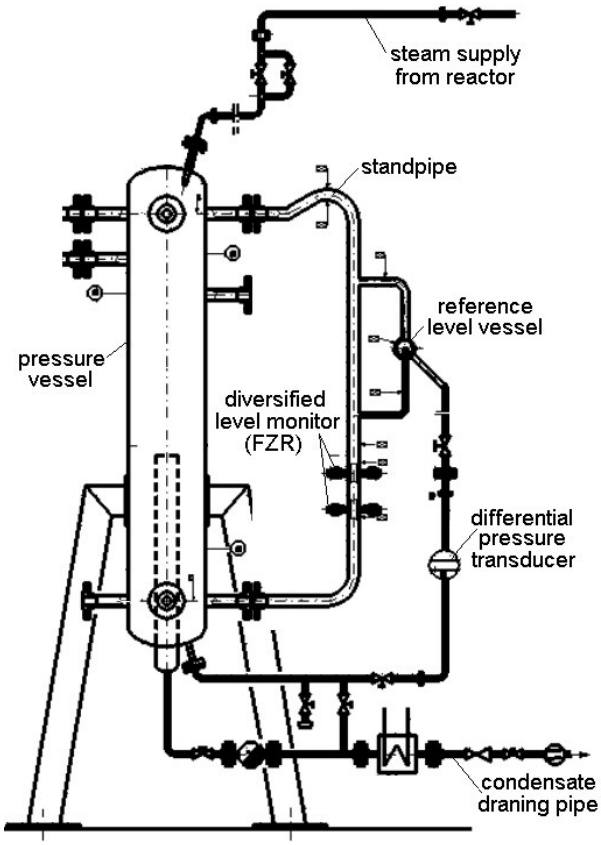

Fig. 8: Test facility for level measuring systems at the Gundremmingen NPP

6. Test facility in the Gundremmingen NPP

A facility for the test of different level measuring systems was built by Gundremmingen NPP (Fig. 8). A number of standpipes are connected to a pressure vessel (height 2.7 m, inner diameter 0.46 m, volume 0.45 m³), which is supplied with steam from the reactor of one of the Gundremmingen units (7 MPa, saturation). Due to condensation, the vessel is filling with water. At the standpipes, different versions of hydrostatic level measuring systems are tested. One standpipe was used for an endurance test of the described diversified level measuring system. Two level sensors (four probes) were mounted at two different axial positions, which have an axial distance of 0.2 m (Fig. 9). The binary outputs of the level monitors were used to control the condensate draining valve. When the upper level monitor delivered the signal LEVEL HIGH the valve was opened. Successively the level in the vessel dropped down. When the level falls below the lower measuring point, the valve is closed and the process repeats.

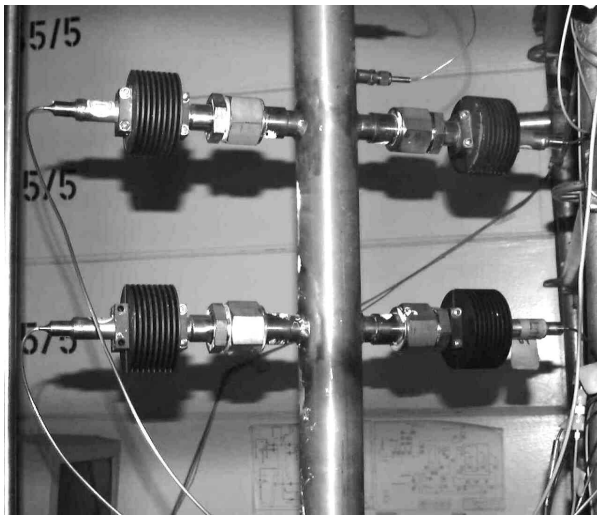

Fig. 9: Probes at the standpipe of the facility

7. Test results

Fig. 10 shows characteristic time histories of the binary level signals, the reading of an analogue

hydrostatic level transducer and the position of the condensate draining valve. As visible, the control of the level in the pressure vessel by the level monitors was functioning. Since the accuracy of the binary level indication is given by the accuracy of the axial position of the measuring detectors, the turning points of the level can be used to assess the error of the hydrostatic method , which, in this case, delivered a negative systematic error of about 3-4 cm.

The test was continued over 4.5 years without the breakdown of a probe. After 10550 hours of operation the measuring sensors were taken out and examined visually. No evidence of corrosion was found neither on the metallic nor on the ceramic parts of the probes. The test is continued.

8. Summary

A diversified level measuring system was developed for boiling water reactors. The design was elaborated under consideration of the German requirements to reactor safety instrumentation (KTA 3505). An endurance test under conditions close to the application in the reactor has shown that the planned lifetime of 5 years can be achieved.

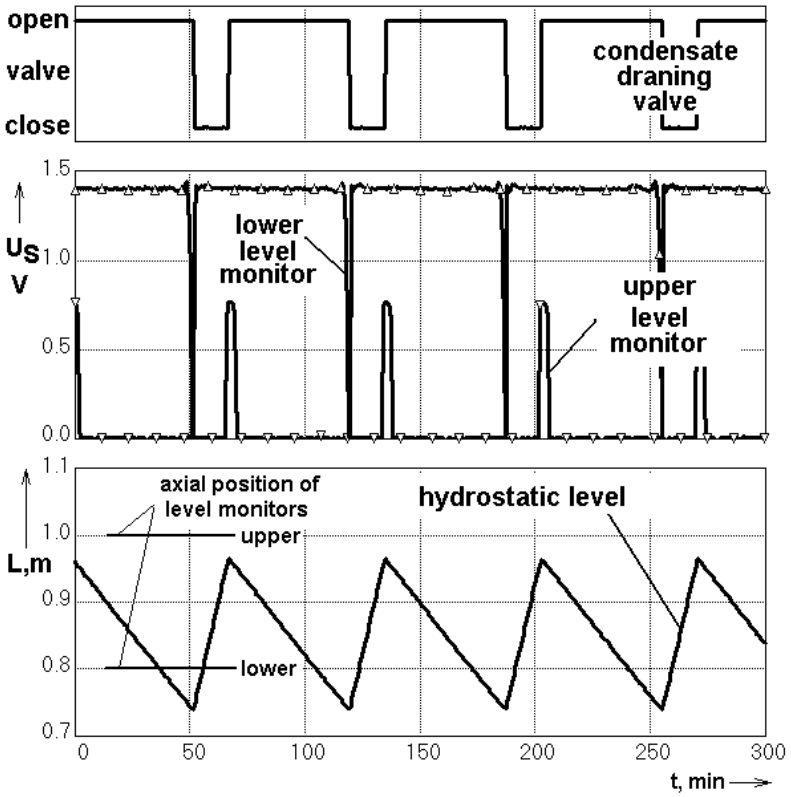

Fig. 10: Characteristic signals from the test of the diversified level monitors of FZR at the facility in Gundremmingen

The qualification procedure for an application at the reactor is under way. The corresponding work is carried out by Framatome ANP. It comprises final design work, the development of a technology for series production, the preparation of the documentation for the qualification and practical examinations according to KTA rules.

References

[1] W. I. Perelman, Taschenbuch der Chemie, Deutscher Verlag der Wissenschaften, Berlin 1959.

[2] P. Cohen, Water Coolant Technology of Power Reactors, Gordon & Breach, Science Publishers, New York 1969.

[3] A. Böttger, J. Zschau, H.-M. Prasser: Anordnung zur Messung der elektrischen Leitfähigkeit mittels Sonden sowie zur Sonden-Funktionskontrolle, Patentanmeldung vom 07.02.1997, Aktenzeichen 197 04 494.8.

[4] D. Baldauf, H.-M. Prasser, G. Tamme, W. Zippe: Nadelsonde zur Messung der Leitfähigkeit in Flüssigkeiten oder Mehrphasengemischen, Patent DE 43 20 116 A1, Anmeldetag: 16.06.1993, Offenlegungsschrift vom 22.12.94.

FLOW STRUCTURE DURING FLASHING IN THE CIRCUS TEST FACILITY MODELLING THE START-UP OF A BOILING WATER REACTOR

Horst-Michael Prasser, Annalisa Manera[1], Arndt Böttger and Jochen Zschau

1. Introduction

Natural circulation of the steam/water-flow is one of the options to operate Boiling Water Reactors. The reactor can undergo instabilities (so-called flashing-induced instabilities) if operated at low pressures and low powers, which are typical start-up conditions. To obtain experimental data needed for code validation, a test facility (CIRCUS) has been built at the Delft University of Technology in the Netherlands [1]. For detailed and high-frequency void-fraction measurements a wire-mesh sensor is used; the sensor has been developed by Forschungszentrum Rossendorf to measure two-dimensional void-fraction distributions in two-phase flow systems [2]. The sensor has been successfully applied to measure gas fractions, flow-pattern transitions and bubble-size distributions in air-water flows [3], for boron dilution measurements during transients occurring in Pressurized Water Reactors [4] and for cavitation experiments during rapid valve closure in pipelines [5]. Nevertheless, it has never been applied in water/steam flows under the condition of varying mixture temperature. Therefore, a set of measurements has been performed with the CIRCUS facility to study the performance of the wire-mesh sensor. Two gamma-transmission set-ups positioned just below and above the wire-mesh sensor respectively have been used for comparison. The work is part of the NACUSP project of the EU.

2. Flashing-induced instabilities in a natural-circulation loop

During operation of steam/water-flow natural-circulation systems characterised by a heated section and an adiabatic section, sudden void production (flashing) can take place in the adiabatic vertical section of the loop even if no boiling occurs in the heated section. The temperature at the exit of the heated section must be higher than the saturation temperature at the exit of the adiabatic section to allow flashing to occur. The process is more important at low pressures because the difference in saturation temperature between the heated and the adiabatic section of the loop is more significant and the ratio between liquid and vapour densities is larger. The process is schematically illustrated in Fig. 1.

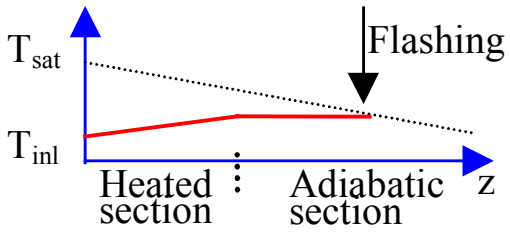

Fig. 1: Flashing in the adiabatic section

As a consequence of flashing, the natural-circulation flow rate will increase as a result of the increased buoyancy of the loop. The increase of the flow rate will lead to a decrease of the temperature of the fluid coming into the adiabatic section to values that can be low enough to suppress flashing. The suppression of flashing will cause a decrease of the flow rate in the loop, leading to a subsequent increase of the fluid temperature. Therefore, flashing can again take place in the riser causing a self-sustained flow oscillation characterised by periodical void production in the adiabatic section of the loop.

[1] TU Delft, Interfaculty Reactor Institute

3. CIRCUS

A scheme of the experimental facility CIRCUS is shown in Fig. 2. The heated section consists of four electrically heated channels and four parallel bypass channels. On the top of the heated section a cylindrical adiabatic section is present. The steam produced in the loop is condensed by means of a heat exchanger.

Table 1: Main characteristics of the CIRCUS facility

Power range per rod	0 - 3 kW
Pressure range	1 - 5 bar
Fuel channel diameter	20.4 mm
Fuel rod diameter	12.5 mm
Bypass channel diameter	10 mm
Heated section length	1.95 m
Riser diameter	47 mm
Riser length	3 m

A steam dome, in which a mixture of steam and water is kept at saturation conditions, is used to control the pressure of the system, while a buffer vessel assures a constant temperature at the inlet of the heated section during experiments. The main characteristics of the facility are reported in Table 1.

The facility is equipped with thermocouples, flowmeters, pressure sensors and pressure-drop sensors. Two Laser-Doppler-Anemometry set-ups are used to measure the flow velocity fluctuations in two parallel channels simultaneously. In addition, the void fraction in the riser is measured by means of a wire-mesh sensor (two-dimensional void-fraction measurements) and by two gamma-transmission set-ups (chordal void-fraction measurements). Details on the wire-mesh sensor and on the two gamma set-ups are given in the following sections.

To perform the experiments, first the facility is pressurised to the desired value of pressure by means of the pressure vessel and the required amount of steam is created in the steam dome. Then, the pressure vessel is disconnected from the loop and the measurement is started after a stationary limit-cycle oscillation is reached. For the study presented in this paper the temperature at the inlet of the heated section has been kept constant at about 98.5 °C and an initial pressure of 1.2 bar has been determined at the exit of the adiabatic section.

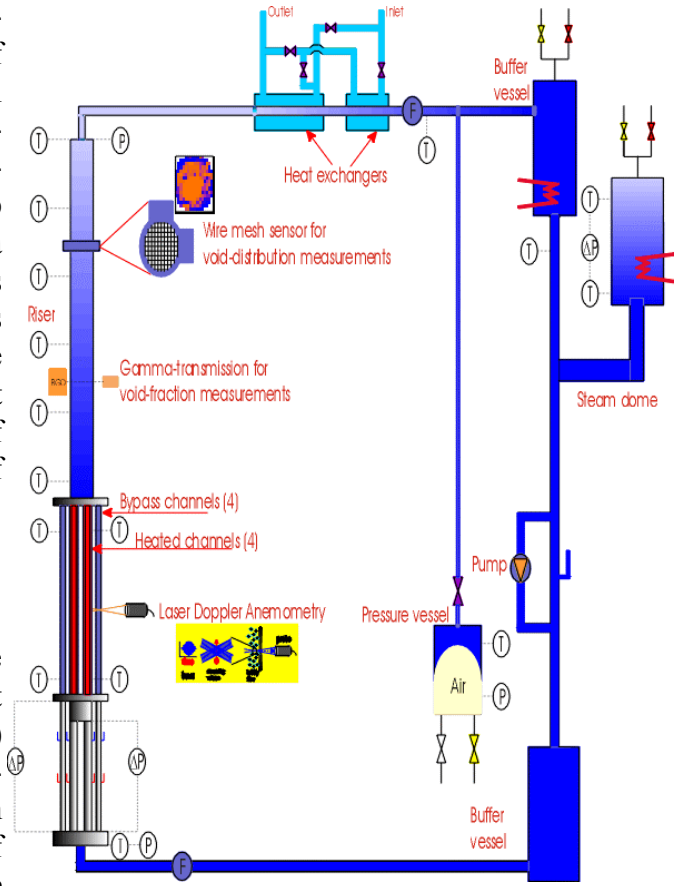

Fig. 2: Scheme of the CIRCUS facility

4. Wire-mesh sensors for CIRCUS

The wire-mesh sensor used in the CIRCUS facility has been developed at the Forschungszentrum Rossendorf (FZR) in Germany; it measures the two-dimensional void-fraction distribution over the section of a pipe on the basis of the local instantaneous conductivity of the fluid flowing in the pipe.

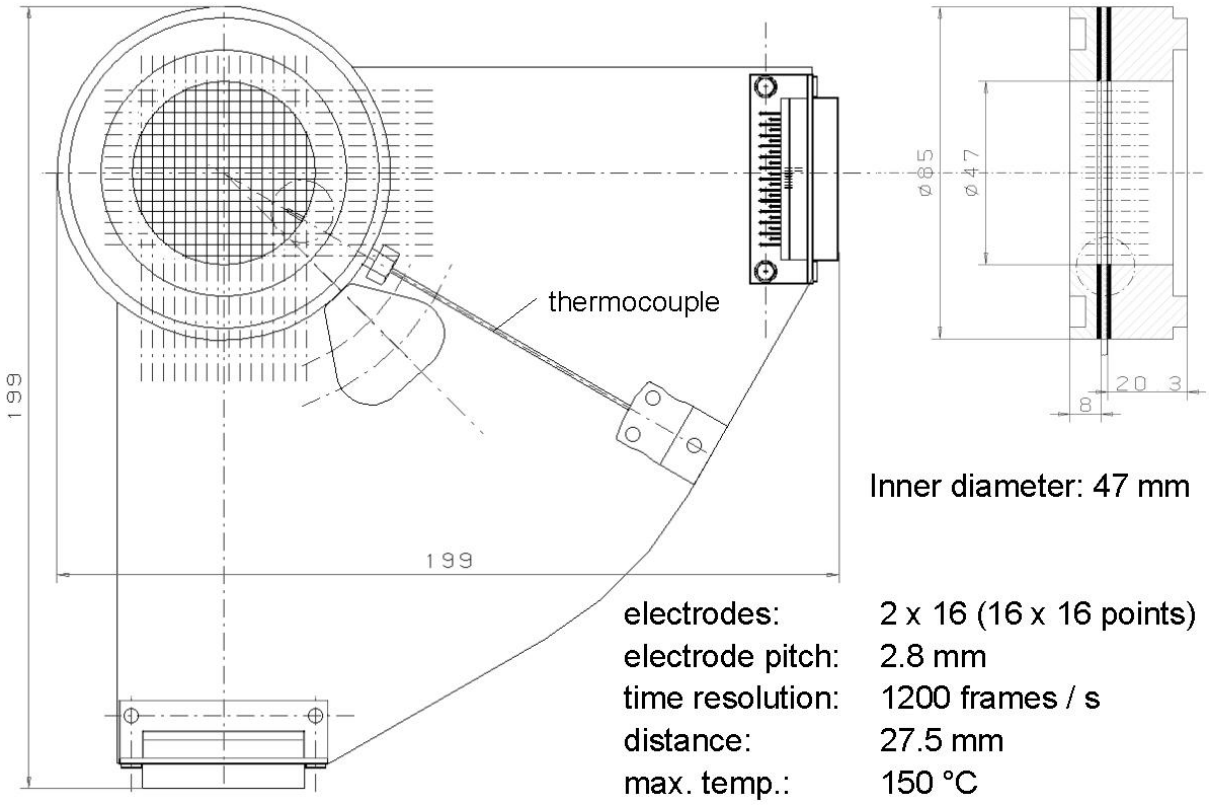

Fig. 3: Wire-mesh sensor

The sensor has a diameter of 47 mm (equal to the diameter of the adiabatic section on which it is mounted) and is made up of two electrode grids of 16 wires each placed at an axial distance of 1.5 mm. The two grids are positioned perpendicularly to each other in order to form a matrix of 16x16 cross-points (see Fig. 3). The distance between two successive parallel wires is 2.8 mm, this being the spatial resolution of the sensor. Details on the working principles of the sensor are given by Prasser [2]. The sampling frequency can be up to 1200 Hz.

The wire-mesh sensor measures the time-dependent fluid conductivity on a matrix of 16x16 points. The conversion to void fraction is performed assuming a linear dependence of the void fraction with respect to the fluid conductivity. For the conversion to void fraction it is necessary to calibrate the sensor in conditions of "tube completely filled with liquid" and "tube completely filled with gas". The calibration data are stored and used successively for the conversion of the measurement data. Additional corrections are needed if variations of the fluid temperature occur during the measurements.

To take fluid temperature variations into account, calibration data of the wire-mesh have been stored at different liquid temperatures and a linear regression has been used to describe the dependence of the conductivity as function of the temperature. The calibration coefficients are determined for each measuring point of the sensors individually. The fluid temperature is measured by means of a thermocouple positioned at the location of the wire-mesh sensor.

An example of the influence of the temperature correction on the spatial-averaged void fraction measured by the wire-mesh sensor during a flashing-induced oscillation is shown in Fig. 4. Without taking into account fluid temperature variations, a non-zero void fraction is measured by the wire-mesh even when one-phase flow is present in the section. The decrease of the conductivity

of sub-cooled water between two flashing cycles results in an erroneous void fraction increase, if the void fractions are calculated assuming a constant liquid conductivity. The effect vanishes when the described temperature calibration is applied.

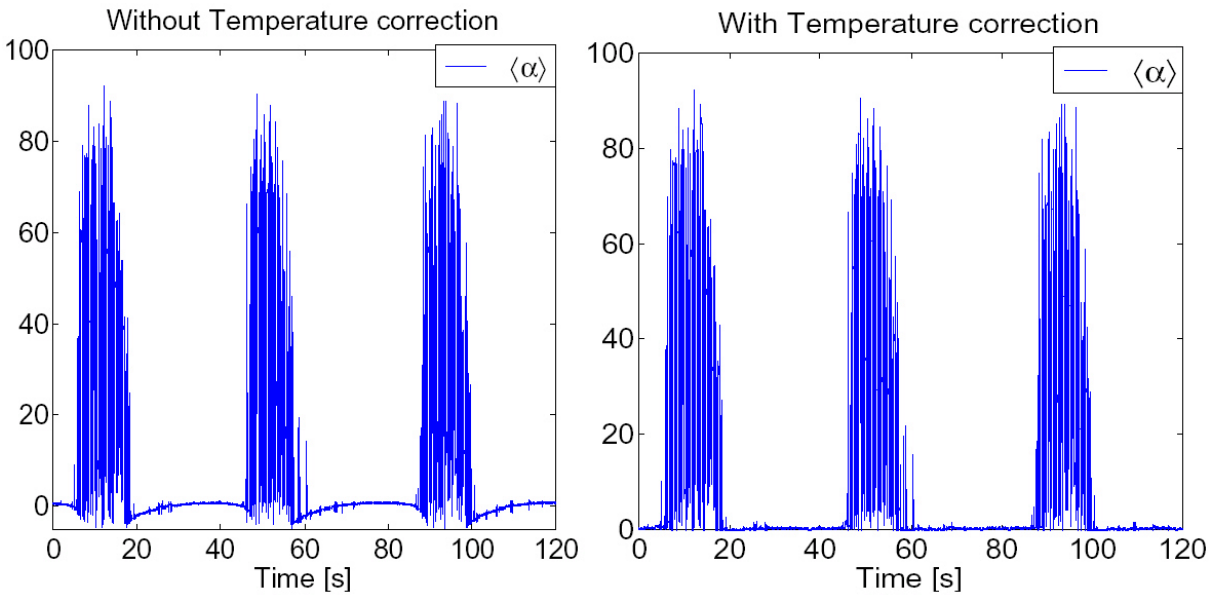

Fig. 4: Average void fraction without (left) and with (right) temperature correction

5. Gamma-transmission measurements at CIRCUS

Two gamma-transmission set-ups are mounted 17 cm above and below the wire-mesh sensor respectively. A 100mCi Cr-51 is used as gamma-source (one for each gamma-transmission set-up); this choice allows relatively small dimensions of the measuring device since only 3.5 cm lead are necessary for shielding purposes. NaI(Tl) scintillator detectors are used and only the Cr-51 gamma-peak (320 keV) is selected. A schematic top view of one of the two gamma-transmission set-ups and the wire-mesh sensor is schematically given in Fig. 5.

The gamma-source S emits a collimated γ-beam of 2 mm width (height equal to 8 mm). A collimator is present in front of the detector in order to measure the chordal void fraction along the 2 mm wide beam crossing the section from the source to the detector. Source and detector are joined together to preserve their relative alignment and they can be moved perpendicularly to the wires of one of the two grids of the wire-mesh sensor (always parallel to the x-direction as indicated in Fig. 6). A fine-step screw is used for a precise positioning of the source-detector system.

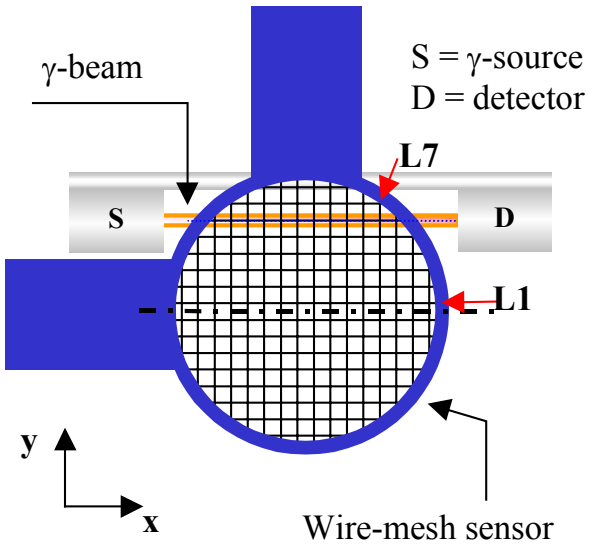

Fig. 5: Scheme of the experimental set-up (top view)

During each measurement the gamma beam is centred along a single wire of the wire-mesh sensor; an example is illustrated in Fig. 6. In this way the chordal void fraction measured by the gamma set-ups along a given path can be directly compared to the chordal void fraction measured by the wire-mesh sensor along the same path.
The chordal void fraction α_i measured by the wire-mesh at a time instant t_k along the i-th wire is evaluated as the sum of the void fraction $\alpha_{i,j}$ in each node belonging to the i-th wire weighted by a factor w_j, that takes into account whether the [i,j]-mesh contributes totally (central mesh) or only partially (mesh at periphery) to the total area intercepted by the sensor along the i-th wire.

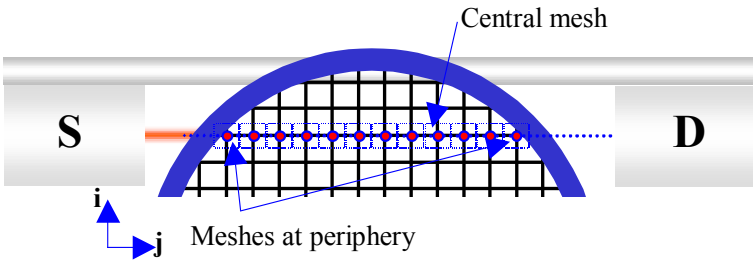

Fig. 6: Averaging for chordal void fraction calculations

Note that the spatial resolution of the wire-mesh sensor (2.8 mm) is somewhat larger than the beam width (2 mm).

6. Comparison between gamma-transmission and wire-mesh sensor

Two sets of measurements have been performed setting the time constant τ_R of the rate-meter of the gamma-transmission set-ups equal to 0.3 and 0.03 seconds respectively, leading to statistical error on the count-rate ranging from less than 2% (for τ_R=0.3 s) to less than 6% (for τ_R=0.03 s). The measurements have been carried out placing the gamma beams along different wires of the wire-mesh sensor, going from the centre of the section (central wire of the wire-mesh sensor L1) to the periphery (wire L7), as indicated in Fig. 5. A trigger is used to synchronise the mesh sensor with the gamma-transmission measurements.

The chordal void fractions measured by the gamma-transmission set-ups and the wire-mesh sensor are shown in Fig. 7 for the measurement performed at position L1 (see Fig. 5) and with a rate-meter time constant equal to 0.3 seconds. The highly detailed structure of the wire-mesh sensor measurement, due to the high sampling frequency achievable, makes a direct comparison with the gamma-transmission measurements difficult. To compare the wire-mesh sensor and the gamma-transmission set-

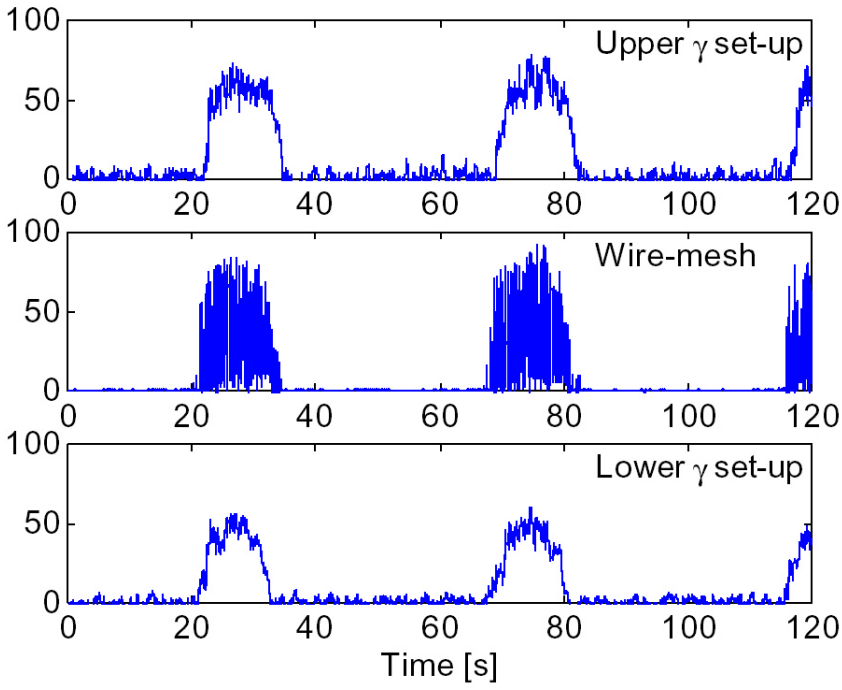

Fig. 7: Chordal void fraction measured by the two gamma-transmission set-ups (τ_R = 0.3 s) and by the wire-mesh sensor at position L1

ups signals, it has to be taken into account that the wire-mesh sensor measures instantaneous void fraction, while the gamma-transmission set-ups behave like a first order integrator with a certain time constant set on the rate-meter used to digitalise the count rate.

If the wire-mesh signal is treated with a filter, the properties of which are identical to the transfer function of the gamma transmission measurement together with the rate meter and its time constant, the result shown in Fig. 8 can be obtained. Here, chordal void fractions are shown for a single flashing cycle. Due to the low-pass behaviour of the filter, the wire-mesh signal is now very similar to the signals of the two gamma transmission devices. The so-called *simulated chordal void fraction* at the wire-mesh sensor is furthermore in a very good quantitative agreement with the gamma transmission measurements, since it blends well into the time history of the two void fractions measured by the neighbouring gamma transmission devices. The evaluation of an entire flashing cycle reveals that the time-averaged chordal void fraction measured by the wire-mesh sensor is in between the time-averaged chordal void fractions measured by the gamma-transmission set-ups for each of the analysed chords L1 - L7.

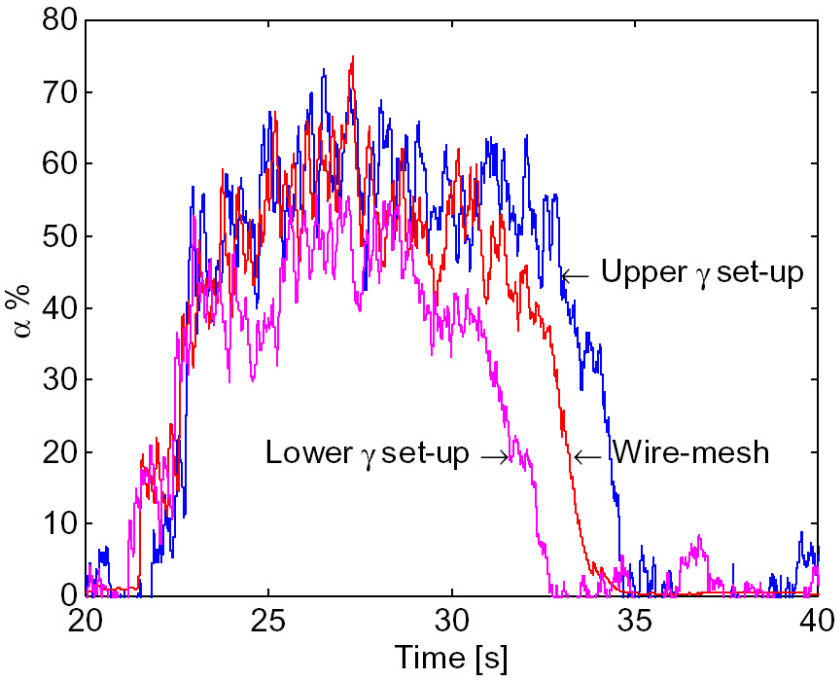

Fig. 8: Chordal void fraction measured by the gamma-transmission set-ups and simulated chordal void fraction at the wire-mesh sensor (τ_R = 0.3 s, position L1)

In addition, experiments have been performed after removing the wire-mesh sensor from the experimental loop to study the possible undesired effect of the wire-mesh sensor on triggering of void production. No notable differences have been found between the measurements performed with and without the sensor in the main characteristics of the flashing-induced instability (i.e. oscillation period, flow rate oscillation, pressure, etc.) and in the void-fraction measurements carried out with the two gamma-transmission set-ups [6].

7. Evolution of the flow structure during the flashing cycle

A very illustrative method to visualise the structure of a gas-liquid flow is the construction of virtual side views, as described in [3]. For this purpose, a time sequence of instantaneous gas fraction distributions over the tube diameter is plotted in a vertical column. An average phase velocity of the gas was used to define a virtual z-axis to construct virtual sectional views of the flow.

This technique was further developed for the representation of the data obtained during flashing. The first problem, which had to be solved, was the determination of the gas velocity in the tran-

sient situation of a flashing cycle. This was carried out by the help of the two wire-mesh sensors mounted one above the other in an axial distance of 27.5 mm. An average phase velocity was calculated for time intervals of 0.5 s from the instantaneous, cross-section averaged void fractions measured by the sensors. In order to guarantee sufficient statistics, the cross correlation was ensemble-averaged over 10 flashing cycles.

The result is shown in Fig. 9. The points were afterwards approximated by a polynomial regression curve of 4th order, which was used to perform the transfer from time to virtual z-axis in the following virtual side views.

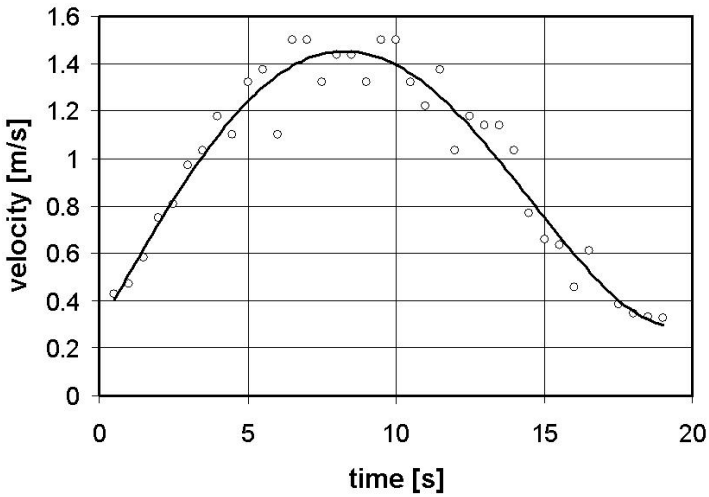

Fig. 9: Time history of the steam velocity obtained by cross correlation, result of an ensemble averaging over 10 flashing cycles

The technique of sectional side views was replaced by the creation of virtual side views on the basis of a simplified light-ray tracking algorithm. The data column was assumed to be illuminated from the left side by parallel white light. For both water and steam phases individual absorption and dispersion coefficients for the three colour components red, green and blue were assumed, and composition and intensity of the light departing in the direction of the observer was calculated.

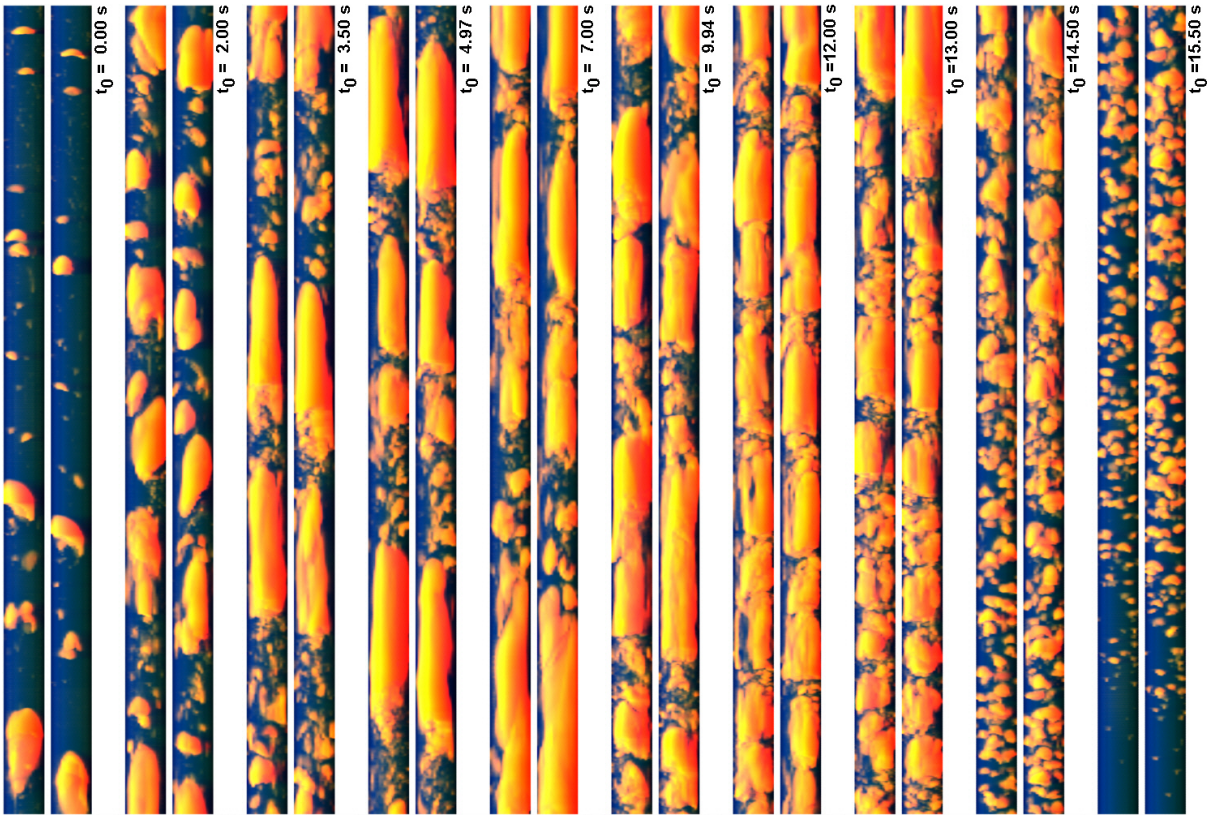

Fig. 10: Virtual side views of the flow structure during a flashing cycle (t_0=0 – begin of flashing)

The result is presented in Fig. 10. Here, after using the velocity data to scale the vertical axis of the columns, height and width of the column correspond to the same geometric scale, so that the bubbles are displayed in their realistic shape (with the accuracy of the velocity assumption).

The light-ray tracking supplies a very illustrative, spatial impression of the shape of the bubbles in the different stages of the flashing cycle. In the beginning just a few bubbles appear; some of them soon reach the size of cap bubbles. The flow soon transits to slug flow with gas plugs, which are over 6-7 pipe diameters long (≅ 300-350 mm). Before the flashing stops, the flow regime again transits to bubble flow.

In the next step, bubble size distributions were obtained using the algorithms described in [3]. The histograms were averaged over 10 flashing cycles. This was necessary to obtain a sufficient statistic reliability, since the transient character of the flow required small integration periods (0.5 s). The distributions (Fig. 11) clearly show the transition from bubble to slug flow and back, characterised by the appearance and vanishing of a bimodal distribution, which contains bubbles with an effective diameter which exceeds the inner diameter of the riser. The appearance of bubbles exceeding this size was earlier found to be a quantitative criterion for the bubble-to-slug flow transition [7].

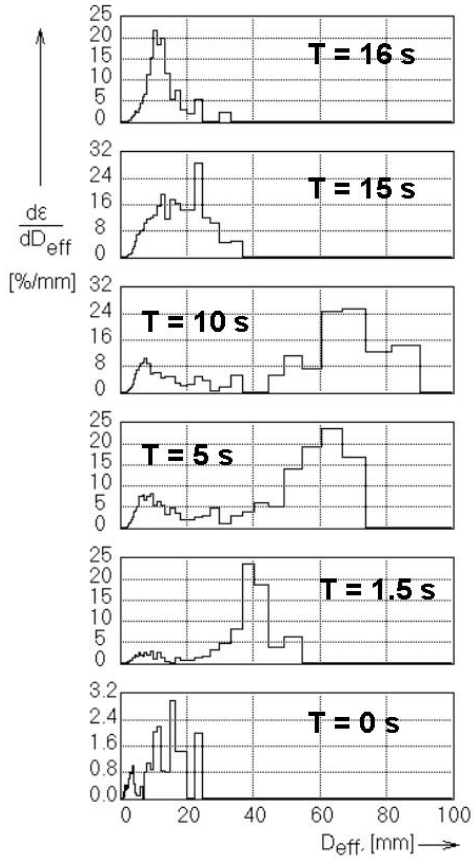

Fig. 11: Bubble size distributions in different stages of the flashing cycle

8. Summary

Wire-mesh sensors have proven to be applicable to studying transient steam-water flow. A comparison with gamma transmission measurements has shown, that the wire-mesh sensor can be used for quantitative void fraction measurements. The application to flashing experiments for boiling water reactors reveals new information about the flow structure, which are valuable for the understanding and modelling of the reactor start-up processes.

References

[1] A. Manera, W. J. M. De Kruijf, T. H. J. J. Van der Hagen (2000), Experiments with the CIRCUS-facility on flashing-induced instabilities during start-up of natural-circulation-cooled BWRs, Proceedings PHYSOR 2000, May 7-11, 2000, Pittsburgh, Pennsylvania, USA (on CDROM), 2000

[2] H.-M. Prasser, A. Böttger, J. Zschau (1998), A new electrode-mesh tomograph for gas-liquid flows, Flow Measurement and Instrumentation 9, 111-119

[3] H.-M. Prasser, D. Scholz, C. Zippe (2001), Bubble Size Measurement using Wire-Mesh Sensors, Flow Measurement and Instrumentation, Flow Measurement and Instrumentation 12 299-312

[4] G. Grunwald, T. Höhne, H.-M. Prasser, H.-M. (2000), Experimental investigations on the four-loop test facility ROCOM, Kerntechnik 65, 5-6

[5] Dudlik, A., Prasser, H.-M., Schlüter, S. (1999), Visualization of cavitating liquid flow behind fast acting valves, Second European Congress of Chemical Engineering - Montpellier 5-7 October (on CD-ROM)

[6] A. Manera, H.-M. Prasser, T.H.J.J. van der Hagen, R.F. Mudde, W.J.M. de Kruijf (2001), A comparison of void-fraction measurements during flashing-induced instabilities obtained with a wire-mesh sensor and a gamma-transmission set-up, ICMF-2001, New Orleans, May 27 - June 1, proceedings on CD-ROM, paper 463

[7] A.-K. Krüssenberg, H.-M. Prasser, A. Schaffrath, (2000), A new criterion for identification of the bubble slug transition in vertical tubes, Kerntechnik 65, 1

DENSITY EFFECTS ON COOLANT MIXING IN PRESSURIZED WATER REACTORS

Gerhard Grunwald, Thomas Höhne, Sören Kliem, Horst-Michael Prasser, and Ulrich Rohde

1. Introduction

During emergency core cooling (ECC) injection into the cold leg of a PWR, an incomplete mixing with the natural circulation flow in the loop takes place. Due to the higher density of the ECC water, a streak of cold water is flowing downwards the downcomer. This causes thermal loads on the reactor pressure vessel (RPV). Furthermore, in the case of inadvertent injection of low borated ECC water, a boron dilution transient would be initiated. The transient is determined by the resulting boron concentration distribution at the core inlet. For the investigation of the influence of density effects, generic experiments have been carried out at the ROCOM (**Ro**ssendorf **Co**olant **M**ixing Model) [1-3] test facility. ROCOM is a 1:5 scaled model of a German KONVOI type 1300 MW PWR with controllable pumps in all loops, so that a wide range of flow conditions between natural circulation and nominal flow can be simulated. Previous investigations have been done on coolant mixing with operating pumps and during the start-up of coolant circulation in the primary circuit without density differences in the fluid [1-3]. It is expected, that density differences can be neglected, if the flow rates are sufficiently high, that means, if mixing is momentum controlled. To find the conditions for transition to buoyancy controlled mixing, generic experiments with density differences were performed. To investigate the mixing of the ECC water, an exactly modelled ECC injection nozzle has been connected to one of the cold legs of ROCOM.

Investigations on density effects in coolant mixing have been performed earlier at different experimental facilities (i.e. HDR [4], UPTF [5], University of Maryland [6, 7]). However, in the experiments presented in this paper, a significantly higher spatial resolution of the tracer concentration measurements is achieved.

2. Boundary conditions of the experiments

Due to the fact, that the test facility cannot be heated up, the necessary density differences were simulated by adding sugar (glucose) to the water that is injected into the cold leg. To observe the mixing of the ECC water, this water was tracered by small amounts of sodium chloride, enhancing the conductivity. Generating density differences by high salt concentrations is not possible, because the measurement system is very sensitive and would be saturated at high salt concentrations.

The test facility is equipped with wire mesh sensors for high resolution measurement of the transient concentration of the tracer in space and time. They are based on the measurement of the electrical conductivity. One sensor is located in the cold leg inlet nozzle of the loop with the ECC injection nozzle, two in the downcomer just below the inlet nozzles and before the entrance into the lower plenum, respectively. Each of the downcomer sensors has a measurement grid consisting of 64 angular and 4 radial points. The fourth sensor is integrated into the lower core support plate and has one measurement position at each fuel element inlet [2]. Dimensionless mixing scalars were derived from the data provided by the sensors with a time resolution of 0.05 s. These scalars are defined as follows:

$$\theta_i = \frac{\sigma_i - \sigma_0}{\sigma_P - \sigma_0} \tag{1}$$

where i is the current measurement position; σ_i the conductivity at that position, σ_0 the conductivity of the water before the experiment and σ_P the conductivity of the injected ECC water.

The goal of the experiments presented in the current work was the generic investigation of the influence of density differences between the primary loop inventory and the ECC water on the mixing in the downcomer. To separate the density effects from the influence of other parameters, a constant flow in the loop with the ECC injection nozzle was assumed in this study. The mass flow rate was varied in the different experiments between 0 and 15 % of the nominal flow rate, i.e. it was kept in the magnitude of natural circulation. The other pumps were switched off. The density difference between ECC and loop water has been varied between 0 and 10 %. Fig. 1 summarises the boundary conditions of the experiments. Altogether 20 experiments have been carried out (dots in Fig. 1). In all experiments, the volume flow rate of the ECC injection system was kept constant at 1.0 l/s. The normalised density is defined as the ratio between ECC water density and density of fluid in the primary circuit. All other boundary conditions are identical. Due to the fluctuations of the flow field in the RPV [2] observed earlier, each experiment was repeated five times to average over these fluctuations.

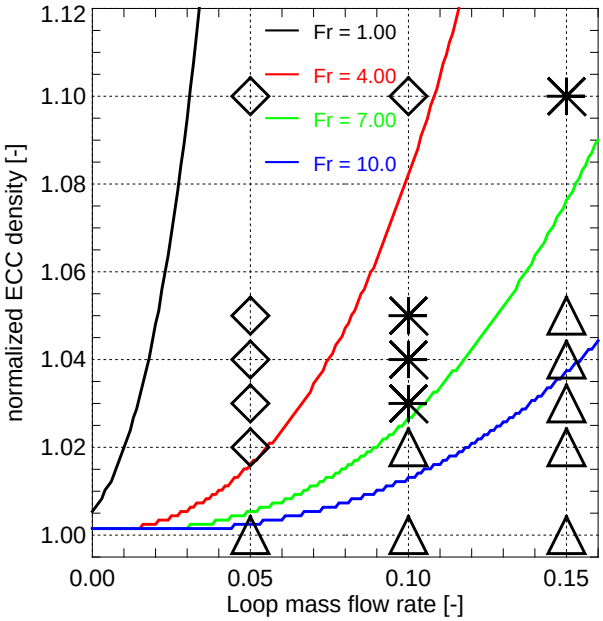

Fig. 1: Matrix of the experiments carried out and Froude-number isolines acc. to eq. (2)

3. Experimental results and interpretation

3.1. Reference experiment

The experiments without density effects serve as reference experiments for the comparison. Fig. 2 visualises the time evolution of the tracer concentration in an unwrapped view measured at the two downcomer sensors. The downwards directed red arrow indicates the position of the loop with the running pump, in that case delivering 10 % of the nominal flow rate. At the upper downcomer sensor, the ECC water (injected in each experiment from t = 5 to t = 15 s) appears directly below the inlet nozzle. Due to the momentum created by the pump, the flow entering the downcomer is divided into two streams flowing right and left in a downwards directed helix around the core barrel. At the opposite side of the downcomer, the two streaks of the flow fuse together and move down through the measuring plane of the lower downcomer sensor into the lower plenum. Almost the whole quantity of ECC water

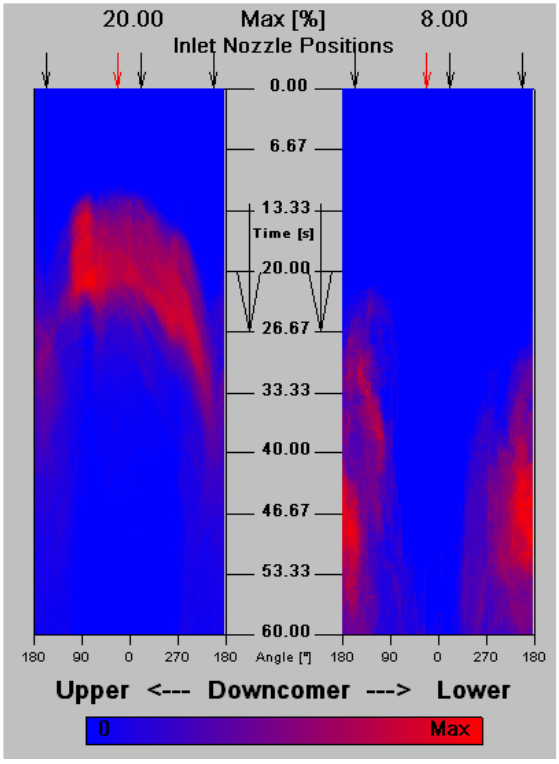

Fig. 2: Time evolution of the mixing scalar at the two downcomer sensors in the experiment with 10 % loop flow rate and no density difference

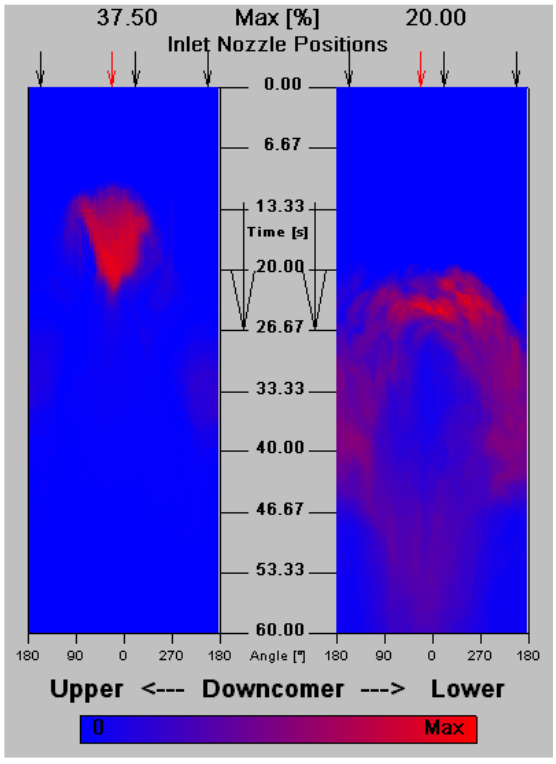

Fig. 3: Time evolution of the mixing scalar at the two downcomer sensors in the experiment with 10 % loop flow rate and 10 % density difference

passes the measuring plane of the lower downcomer sensor at the side opposite to the azimuthal position of the affected loop.

The maximum tracer concentration of the ECC water in the downcomer is 20 % of the injected water concentration at the upper sensor and 8 % at the lower sensor. This concentration profile results from the velocity field typical for single-loop operation. It has its maximum at the opposite side of the downcomer and a minimum at the azimuthal position of the running loop, which has been found in velocity measurements by means of a Laser-Doppler anemometer [8].

3.2 Experiment with 10 % density difference

Fig. 3 shows the experiment, carried out at the same flow conditions, but the density difference between the injected ECC water and the primary loop coolant is now 10 %. In that case a streak formation of the water with higher density is observed. At the upper sensor, the ECC water covers a much smaller azimuthal sector. The density difference impedes the horizontal propagation of the ECC water. The ECC water falls down in an almost straight streamline and reaches the lower downcomer sensor directly below the affected inlet nozzle. Later only, coolant containing ECC water appears at the opposite side of the downcomer. The maximum concentration values observed at the two downcomer sensors are significantly higher than in the case without density differences, i.e. 37.5 % and 20.0 % from the initial concentration in the ECC water tank. The visualisations of the behaviour of the ECC water in the downcomer reveals that in case of momentum driven flow, the ECC water covers nearly

the whole perimeter of the upper sensor and passes the measuring plane of the lower sensor mainly at the opposite side of the downcomer. When the density effects are dominating, the sector at the upper measuring device covered by the ECC water is very small. The ECC water falls down straightly and passes the sensor in the lower part of the downcomer below the inlet nozzle of the working loop. Furthermore, variations of the density were carried out to identify the transition region between momentum driven and density driven flow.

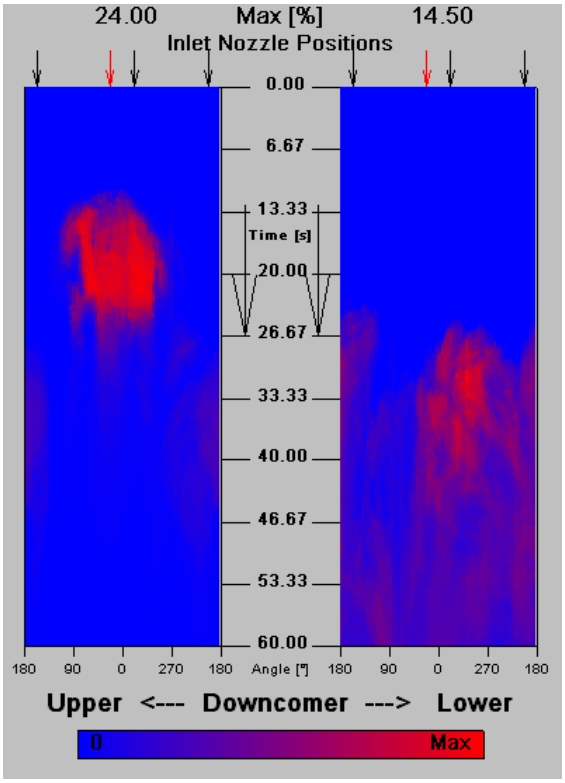

Fig. 4: Time evolution of the mixing scalar at the two downcomer sensors in the experiment with 10 % loop flow rate and 4 % density difference

3.3 Experiment with 4 % density difference

Fig. 4 shows an experiment with a density difference of 4 %, while the flow rate was again 10 % of the nominal. At the upper sensor, the width of the azimuthal sector covered by the ECC water is in-between the two cases with 0 % respectively 10 % density difference. Near the lower sensor, the ECC water reaches the opposite side of the downcomer and the region below the inlet nozzle position almost at the same time. That means, that one part of the ECC water follows the stream lines of the external momentum driven flow field and another part directly falls down due to the internal momentum created by density differences. We consider this as an intermediate state between momentum and density driven flow. The experiment in Fig. 4 was therefore assigned to the transition region between the two flow regimes.

Based on these observations, the set of experiments conducted according to the matrix in Fig. 1, was divided into three groups: density dominated flow (◊), momentum dominated flow (Δ) and the transition region (*). The conditions at the inlet into the downcomer were used to calculate Froude-numbers of the experiments according to the following formula [3]:

$$Fr = \frac{v_{in}}{\sqrt{g \cdot s \cdot \frac{\rho_{in} - \rho_a}{\rho_{in}}}} \qquad (2)$$

where v_{in} is the velocity at the reactor inlet (combined loop and ECC flow), g is the gravitational acceleration, s is the width of the downcomer, ρ_{in} the density of the incoming flow, calculated with the assumption of homogeneous mixing between ECC and loop flow, and ρ_a the density of the ambient water in the downcomer. Lines of constant Froude-numbers calculated by means of this formula are shown in Fig. 1. All experiments identified as density dominated are located in the region left of the isoline *Fr = 4.0* and all momentum dominated points are found right of the isoline *Fr = 7.0*. These two numbers are critical

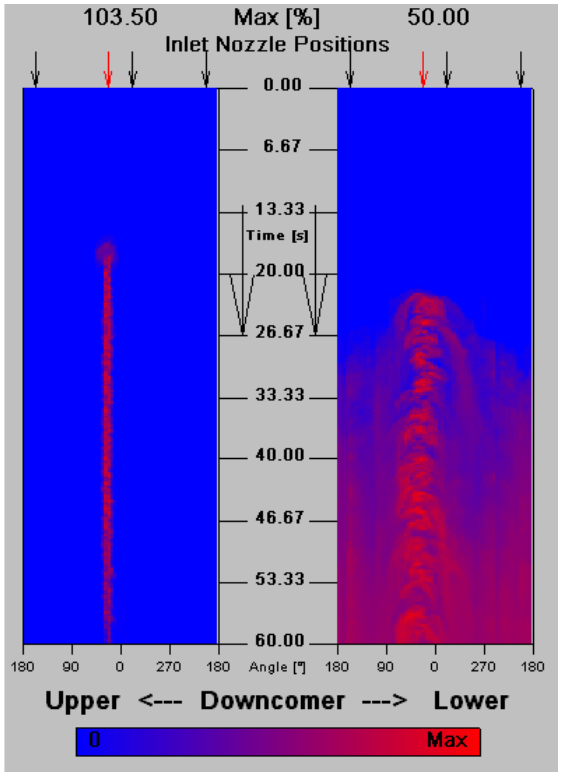

Fig. 5: Time evolution of the mixing scalar at the two downcomer sensors in the experiment with 0 % loop flow rate and 10 % density difference

Froude numbers separating the two flow regimes for the ROCOM test facility. A transition region is located between the two critical values.

Density effects are extremely developed in an experiment with no flow in the primary loop (Fig. 5), where the fluid circulation is initiated only by starting the ECC injection (injection time was 40 s). At the upper sensor, the ECC water appears unmixed and covers a sector of only about 15°. The data from the lower downcomer sensor show clearly buoyancy induced turbulent structures. As can be concluded from these data, the water with higher density accumulates in the lower plenum.

4. Core inlet distribution

The conclusions concerning the influence of the density on the mixing processes in the RPV are confirmed by the experimental data obtained from the measuring device at the inlet into the core. Fig. 6 shows the distribution of the tracer at the core inlet sensor at the time point of the first maximum in the three above described experiments. The different mixing mechanisms responsible for the distribution of the tracer in the downcomer determine the distribution at the core inlet, too. Thus, in the experiment without density differences, the ECC water goes preferred to the side opposite to the azimuthal position of the loop with the working pump. The experiment with 4 % density difference shows the transition character of the flow regime and in the experiment with 10 % density difference the first tracer appears directly below the position of the loop with the working pump.

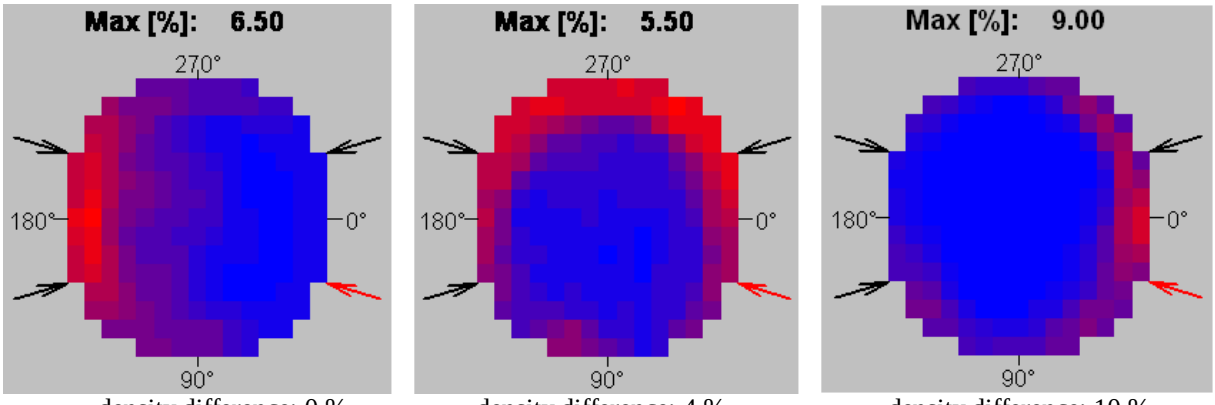

density difference: 0 % density difference: 4 % density difference: 10 %

Fig. 6: Core inlet distribution of the mixing scalar at the time point of maximum in the experiments with 10 % loop flow rate and varied density difference

5. Outlook

The goal of further investigations should be to clarify the possibility of generalisation of the transition criterion between density controlled and momentum controlled mixing and the dependence on geometry and other parameter constellations. This should include the analysis of experiments from other test facilities. The data of the experiments will be used for the validation of computational fluid dynamics codes to density driven flow regimes in reactor geometry.

References

[1] R. Hertlein, H.-M. Prasser, F.-P. Weiß, M. Scheuerer, R. Wohlstein (2001), Kühlmittelvermischung in DWR bei Borverdünnungs- und Kaltwassertransienten, Annual Meeting on Nuclear Technology '01, Topical Session: "Integral tests for the improved safety assessment of LWR"

[2] G. Grunwald, Th. Höhne, H.-M. Prasser, F.-P. Weiß (2000), Coolant mixing in PWR at constant coolant flow in the primary circuit, in Proc. Annual Meeting on Nuclear Technology '00 (pp. 109 – 114) INFORUM GmbH, Bonn

[3] S. Kliem, H.-M. Prasser (2001), A semi-analytical model for the description of coolant mixing inside the KONVOI reactor pressure vessel during pump start-up, Proc. Ann. Meeting on Nucl. Technology '01 (pp. 107–112) INFORUM GmbH, Bonn

[4] HDR safety program – thermal mixing in the cold leg and downcomer of the HDR test rig (1990), Report PHDR 91-89, FZ Karlsruhe

[5] K. Umminger, W. Kastner, J. Liebert, T. Mull (1999), Thermal hydraulics of PWR's with respect to boron dilution phenomena: Experimental results from the test facilities PKL and UPTF, Ninth Int. Topical Meeting on Nuclear Reactor Thermal Hydraulics (NURETH–9), San Francisco, California

[6] M. Gavrilas and K. Kiger (2001), ISP-43: Rapid boron dilution transient experiment, comparison report, NEA/CSNI/R(2000)22

[7] B. Woods (2001), UM 2x4 loop experimental findings on the effect of inertial and buoyancy forces on annular flow mixing for rapid boron dilution transients, Ph.D. Thesis, University of Maryland

[8] G. Grunwald, Th. Höhne and H.-M. Prasser (2001), Laser-Doppler-velocity measurements in the downcomer of the ROCOM test facility in comparison with numerical results, Report FZR-334, ISSN 1437-322X, Rossendorf (in German)

Acknowledgement

The project this paper is based on is funded by the BMWi (Bundesministerium für Wirtschaft) and is registered with No. 150 1216.

ANALYSIS OF A BORON DILUTION TRANSIENT USING THE CODE DYN3D COUPLED WITH THE SEMI-ANALYTICAL COOLANT MIXING MODEL SAPR

Sören Kliem, Siegfried Mittag, and Reinhard Koch

1. Introduction

The coupling of 3D neutron kinetics core models with advanced thermohydraulic system codes leads to the necessity of the implementation of a model, which links the thermohydraulics of the system code with the thermohydraulics of the core model, simulating the coolant mixing in the reactor pressure vessel (RPV) in a realistic way. Due to the long computation times, the direct integration of Computational Fluid Dynamics (CFD)-modules into reactor safety analytical tools is not practical at present. For that reason, a fast running model for the description of the coolant mixing inside the RPV has been developed. Development and validation of the Semi-Analytical Perturbation Reconstruction (SAPR) model is described in [1]. In this paper, the application of the model in combination with the 3D reactor dynamics code DYN3D [2] to the analysis of a boron dilution transient is presented.

2. Boundary conditions and stationary core calculations

The analysis presented here has been carried out for the begin of an equilibrium fuel cycle of a generic four-loop pressurized water reactor. The macroscopic cross section library needed for the core calculations has been generated by the 2D neutron transport code HELIOS. The library contains cross section sets dependent on burn-up and the thermo-hydraulic feedback parameters in a range of variation being relevant for the transient under consideration. The reactor is assumed at hot zero power in a subcritical state. The Xenon- and Samarium-distributions correspond to the full power state. All control rods are inserted, except one, which sticks at fully withdrawn position. This control rod is located in the core region, where the minimum boron concentration during the analysis of the transient has been predicted.

The considered boron dilution scenario is based on the analysis of the restart of the first main coolant (MCP) pump in a PWR after a steamgenerator tube rupture accident [3]. It was assumed in this analysis, that a slug of boron-free coolant has been created in the main circulation loop and is driven into the core by switching-on the first MCP. The coolant in the lower plenum has a temperature of 192 °C and a boron content of 2200 ppm. The temperature of the deborated slug is 210 °C. The initial subcriticality of this state (before the restart of the circulation) is determined with -7787 pcm.

The mixing of the slug with the highly-borated coolant in the downcomer and the lower plenum is calculated by means of the SAPR-model. The initial slug volume used as input to SAPR has been varied between 0 m^3 and the bounding volume of 36 m^3 [3] in steps of 4 m^3. The core inlet boron and coolant temperature distribution for the time point of the total minimum boron concentration reached during the analysis has been extracted for each slug volume from the SAPR-results.

For each case of boron and temperature distribution, a stationary core calculation for the hot

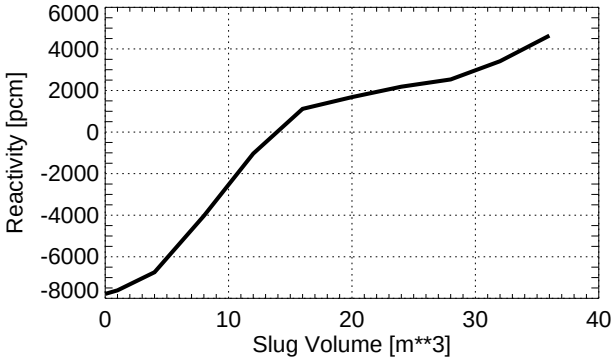

Fig. 1 Static reactivity dependent from the volume of the unborated slug

zero power state described above has been carried out by means of DYN3D. In these calculations, the inlet distribution is extended over the whole height of the core, that means, a uniform axial distribution is assumed. Fig. 1 summarises the results of the stationary calculations, showing the dependency of the static core reactivity from the initial slug volume. It follows from the stationary calculations, that an initial slug volume of less than 16 m^3 does not lead to a recriticality of the core. That means, that only cases with an initial slug volume of at least 16 m^3 are of interest for the transient analysis.

3. Transient core calculations

The first transient calculations have been carried out for the initial slug volumes of 16 and 20 m^3. The SAPR-Model provides the time-dependent boron concentration and coolant temperature at the inlet into each fuel assembly. In the DYN3D-code, the fuel assemblies are modelled as isolated parallel thermohydraulic channels.

The MCP reaches its full mass flow rate about 15 s after the switching-on. The boron front reaches the core bottom about 12 s after switching-on the MCP. This time is the starting point for the transient core calculations. The average coolant velocity is 0.45 m/s at that time and enhances up to 0.65 m/s during the next seconds. Earlier analyses of boron dilution events showed a significant influence of the description of the boron front through the core on the behaviour of reactivity and nuclear power in transients with low fluid velocity [4]. In

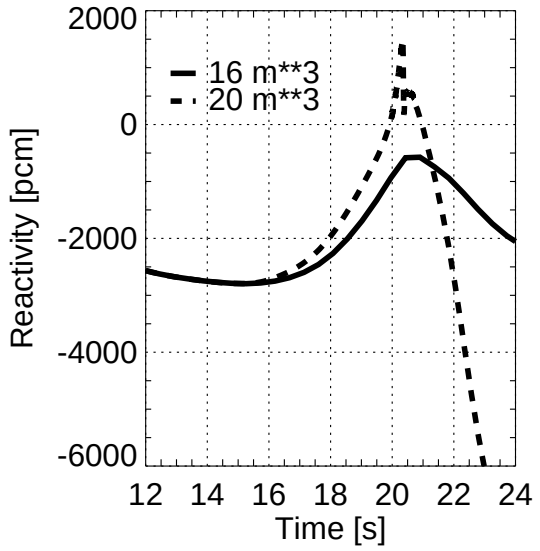

Fig. 2 Dynamic reactivity in the case of a 16 and 20 m^3 unborated slug

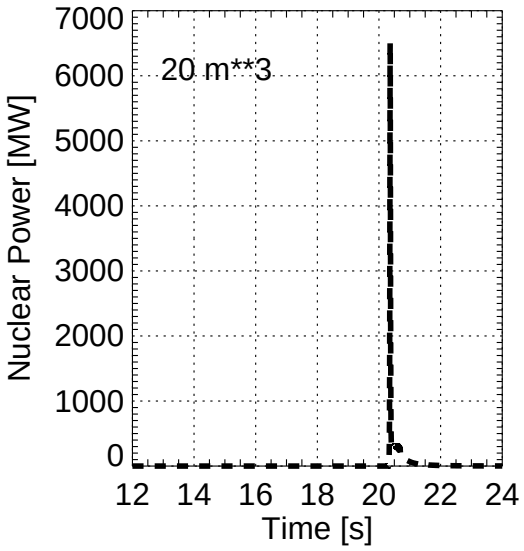

Fig. 3 Nuclear power in the case of a 20 m^3 unborated slug

connection with these analyses, a special model, based on a particle-in-cell (PIC) method for the description of the boron transport through the reactor core has been developed. Using the PIC-method for the boron transport in the core allows to select a time step width, which satisfies the requirements of the interaction between neutron kinetics and thermohydraulics. Numerical diffusion is fully suppressed.

Fig. 2 shows the dynamic reacticvity during the transient for the 16 m^3 and the 20 m^3 cases. As can be seen, the dynamic reactivity in the 16 m^3 case remains always below the zero-line. This is connected with the fact, that the slug has a finite length, what was not taken into account in the stationary calculations extending the minimum inlet distribution of the boron concentration in axial direction. The boron dilution in the reactor core due to the slug of 20 m^3 causes a super prompt critical reactivity insertion leading to a very short power pulse with a magnitude of more than 6500 MW (Fig. 3). It is limited due to the strong, practically promptly acting Doppler feedback of the fuel temperature. The small half width of the power peak did not lead to a significant enhancement of the coolant temperature, boiling did not occur.

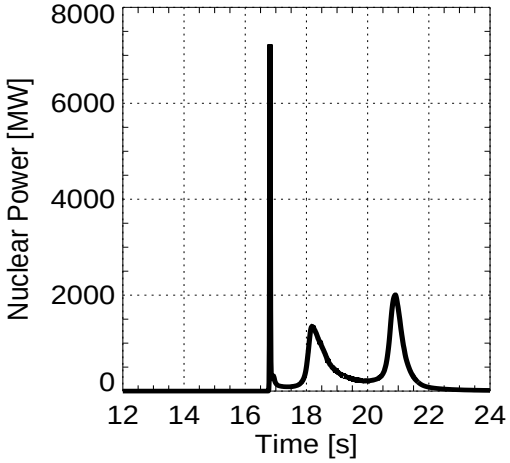

Fig. 4 Nuclear power in the case of a 36 m^3 unborated slug

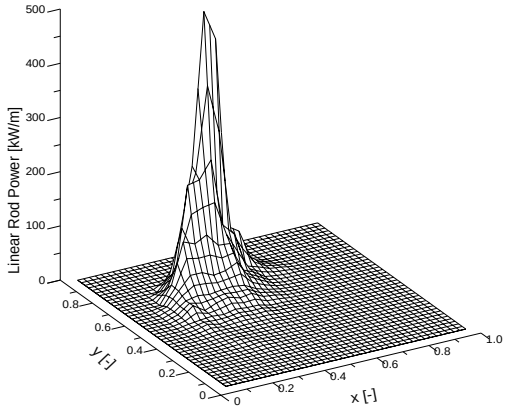

Fig. 5 Radial distribution of the linear rod power density in the moment of maximum power (36 m^3 case)

With more than 7000 MW, the magnitude of the power peak is only slightly higher in the calculation with the bounding slug volume of 36 m^3 (see fig. 4) than in the previous calculation. The Doppler feedback stops the further power increase, too. Contrary to the 20 m^3 case, the power peak occurs even before the boron concentration has reached its minimum. Because the positive reactivity insertion is continued after the power peak, typical secondary power peaks are observed. As can be seen from fig. 5, the radial power distribution over the reactor core is very heterogeneous. At the location of the power maximum, coolant boiling with a maximum void fraction of up to 70 % occurs for a short time. However, no heat transfer crisis was obtained, so that the cladding temperatures keep below 260 °C and no safety relevant limitations are violated.

4. Conclusions

The coolant mixing model SAPR, which provides realistic boron concentration fields at the core inlet, has been used in combination with the reactor dynamics code DYN3D for a

parameter study of a hypothetical boron dilution event. By varying the initial slug volume it was found, that for the given core configuration slugs of less than 16 m^3 did not lead to supercriticality in static calculations. Transient calculations revealed a further conservatism of the static analysis. Only an initial slug volume of 20 m^3 leads to a power increase of the shut-off reactor in the calculation. According to these calculations, even a reactivity insertion up to 2 $ connected with the 36 m^3 slug did not lead to safety relevant consequences. The power excursion is controlled by the Doppler feedback.

The consideration of realistic assumptions concerning the coolant mixing in the RPV preserves a great amount of inherent safety of the reactor. Earlier analyses with conservative coolant mixing assumptions provide supercriticality even for smaller slug volumes.

A proper description of the boron transport through the core in case of transients with low coolant velocity is absolutely necessary to calculate the neutron kinetic behaviour of the core in a right manner. Otherwise the numerical diffusion distorts the boron front and the reactivity insertion is smoothed artificially.

This parameter study performed for a generic PWR is a demonstration of the capabilities of the mixing model SAPR in combination with the neutron kinetic core model DYN3D In case of the application of the mixing model to a certain reactor, the bounding initial slug volume for a specific scenario has to be determined and then used as input to the mixing model.

In the near future, the model is to be implemented into the coupled code DYN3D/ATHLET. That would allow to carry out analyses of the whole plant behaviour. This is especially important during steam line break analyses, where the core behaviour is influenced by the whole primary circuit and even the steamgenerator secondary side must be considered over several hundred seconds.

References

[1] S. Kliem, H.-M. Prasser (2001), A semi-analytical model for the description of coolant mixing inside the KONVOI reactor pressure vessel during pump start-up, Proc. Ann. Meeting on Nucl. Technology ‘01 (pp. 107–112) INFORUM GmbH, Bonn

[2] U. Grundmann, U. Rohde (1996), DYN3D – A 3-dimensional core model for steady-state and transient analysis in thermal reactors , Proc. Int. Conf. on the Physics of Reactors PHYSOR’96 (pp. J70 – J79)

[3] R. Reinders (1998), Dreidimensionale Berechnung der Borkonzentration im RDB nach einem DE-Heizrohrleck, in Proc. Annual Meeting on Nuclear Technology ’98 (pp. 107 – 110) INFORUM GmbH, Bonn

[4] U. Rohde, D. Lucas (1998), Solution of the 4th AER Dynamic Benchmark by use of the code DYN3D with a Particle-in-Cell method for the description of boron transport, Proc. 7th Symposium of AER (p. 387) KFKI Atomic Energy Research Institute, Budapest

Acknowledgement

The project this paper is based on is funded by the BMWi (Bundesministerium für Wirtschaft) and is registered with No. 150 1225.
The authors thank Dr. D. Lucas (FZR) for implementing the PIC-Method into the core model DYN3D.

EXPERIMENTAL VALIDATION OF CROSSFLOW IN THE REACTOR CORE GEOMETRY

Margarita Kliem

1. Introduction

At present, there are two possible approaches, which practically are used for the thermal-hydraulic analyse of the reactor core in simulations, where crossflow effects are relevant. The first of them is the representation of the core by a system of separated parallel flow subchannels with provision of a forced crossflow mixing by implementation of additional formulations (sometimes without the net mass exchange between the subchannels). The flow fields, calculated with this approach, are characterised by straight stream lines, what is not always a correct representation of the real state. The second approach, is a porous body approximation, in which the core geometry is replaced by a structure of homogenized zones of porous media with different properties. In some cases [1], when crossflow is comparable with flow along the bundels, the porous body approach is the only suitable method to perform steady-state and transient flow calculations for safety analyses.

The CFD – code CFX-4 offers a porous region model for the modelling of the core geometry as a homogenized medium. The volume porosity is the first in a set of properties, which were determined for the characterisation of the porous region in CFX-4. The volume porosity is the volume fraction, which is free for flow and can be set by the user. The area porosity tensor is assumed to be isotropic. Its coefficients, corresponding to the volume porosity can also be set by the user. The coefficients of the resistance tensor, which is not limited to be isotropic, can be either preset (what is only valid for simple flow cases and geometries) or calculated by special correlations. These correlations can be implemented by means of user subroutines. The turbulence model in the porous region is the same as the turbulence model specified for the rest of the flow. The modifications to this turbulence model due to the presence of the porous media, as well as the heat sources can also be implemented or set by the user subroutines.

R. D. Lonsdale proposed a simple model for turbulent flow in anisotropic porous media [2]. The correlations for drag due to flow through the porous medium and for the effective diffusivities of momentum and heat are included in this model. In this model, it is assumed, that the turbulence is fully developed everywhere and the turbulence quantities are only dependent upon local flow conditions. The basis for the equations were the theoretical assumptions for the turbulent flow in rod bundles, concerning the relationships between the mean turbulent characteristics, and empirical correlations. In the frame of this work, these formulations were implemented in CFX-4 as a part of the porous region model. Due to this implementation it is now possible to take into account the anisotropy of the flow in porous media. However, an extended validation of the model against experimental data is necessary.

2. Description of the experimental facility

The Core Crossflow Experimental Facility (CCEF) was built with the objective to obtain experimental data for the validation of the implemented model and for the investigation of forced crossflow mixing in reactor core geometry.

The turbulent single-phase flows with relative small velocities, which range under loss-of-flow accident conditions [1] between 8-25 cm/s in the core, and recirculation zones (what means the different flow angles to the rods of the bundle) are the subject of these experimental investigations. Such low mass flow rates can be caused during an accident i.e. and after the switch-off of the main coolant pumps [3]. The Reynolds number corresponding to these small coolant velocities, which achieve only a few cm/s, remains below 10^4. The test section of the experimental loop was designed for turbulent flow inside this Reynolds number range.

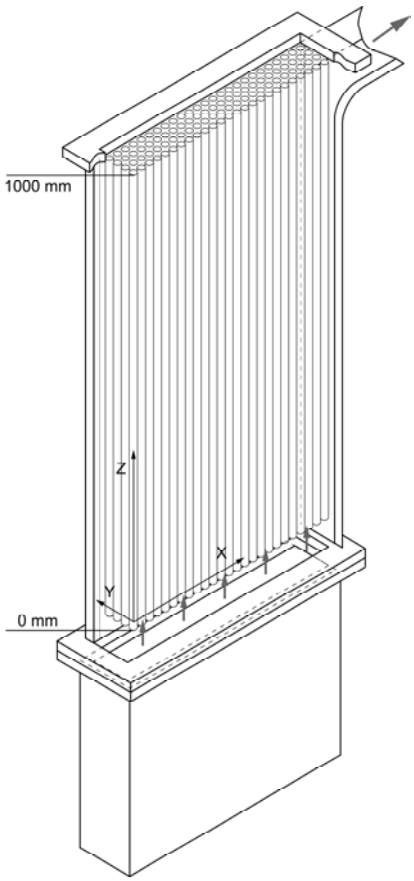

Fig. 1: Sketch of the CCEF test section.

Fig. 1 shows a view of the test section used for the experiments. Fluid enters the bottom of the flow housing, flows vertically along the rods and leaves the test section thought outlet at the right side. The block of the test geometry consists of 100 acryl rods with 15 mm diameter, arranged in 4 rows. The 1000 mm long rods are locked in the upper plate of the test section housing and are fixed with a spacer grid 20 mm above their lower end. The test geometry block can be replaced by another one with modified geometry if necessary.

The experiments were done in an isothermal recirculating flow loop at room temperature. Turbulent velocity measurements were made using a one-component laser-Doppler anemometer manufactured by Dantec. The measurements of the horizontal (x-direction) and vertical (z-direction) velocity components were accomplished at four different elevations (according to 22, 700, 800, 900 mm in z-direction) for five different mass flow rates. It is assumed, that the value of the third velocity component is about zero, because of the small extension of the test section in y-direction.

Fig. 2 shows the measurement points for each elevation. The computer controlled traversing system moves automatically the laser optics to the next point according the measurement lattice.

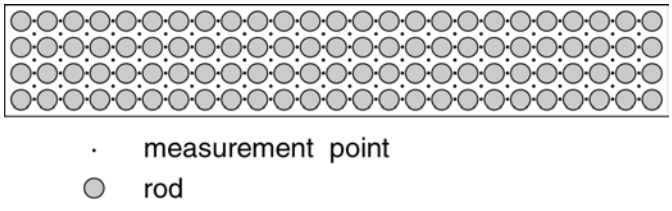

Fig. 2: Arrangement of the measurement points.

3. Comparison with the flow calculations

Calculations for comparison with experimental data were performed in two different approaches. The detailed geometry was created for the calculation of flow fields with the k-ε turbulence model and includes about 140.000 nodes. A relative simple geometry of the CCEF test section was created for the flow simulation in the porous

region approach with about 40.000 nodes. It was assumed in both cases that the fluid is incompressible. The velocity profile measured at the lowest elevation was set at the inlet (corresponding to the mass flow rate of the experiment). A pressure boundary condition was set at the outlet for both types of flow simulations with the value of 10^5 Pa.

Fig. 3 shows the flow field for the simulation with the k-ε turbulence model. This figure gives an impression of the flow structure in the test section of CCEF. The flow field in the calculation with porous region approach looks similar to that in Fig. 3. The differences will be clear by comparison of the corresponding values of velocity components in the experiment and the calculations at the same geometrical position.

Fig. 4 and 5 show the profiles of the vertical velocity component *w*, over the geometrical position of the measurement points between the second and third rows of rods, for the highest elevation (900 mm) and for second mass flow rate 5.0 l/s and for the highest mass flow rate (9.4 l/s) at the 700 mm elevation, respectively.

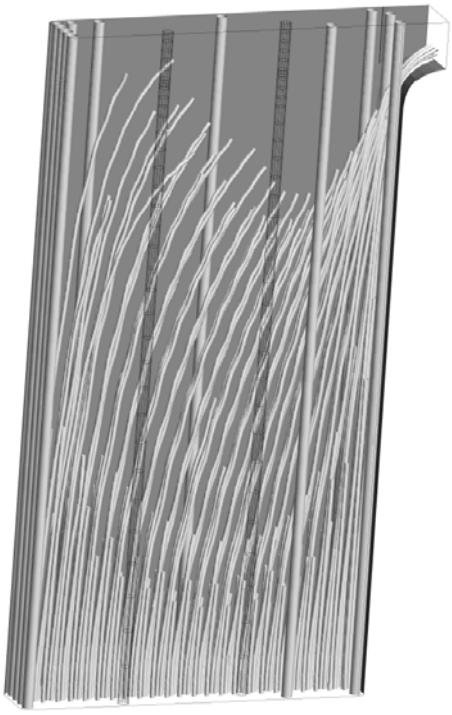

Fig. 3: Stream lines for the calculation in the detailed geometry.

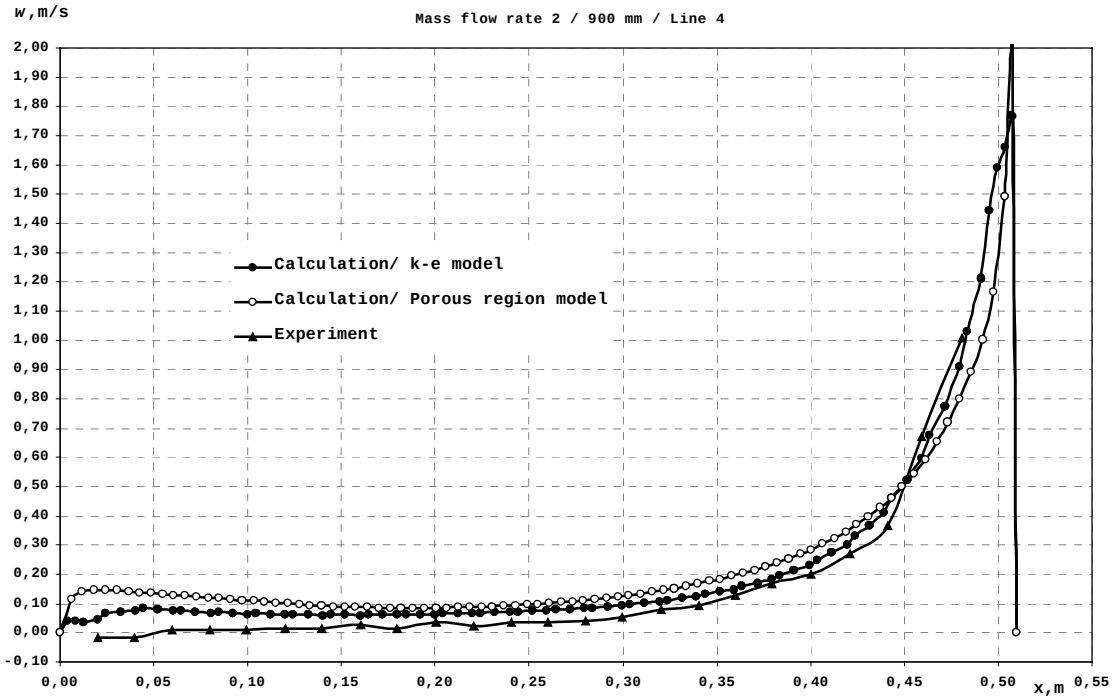

Fig. 4: Comparison of the calculation results with experimental data for the mass flow rate 2.

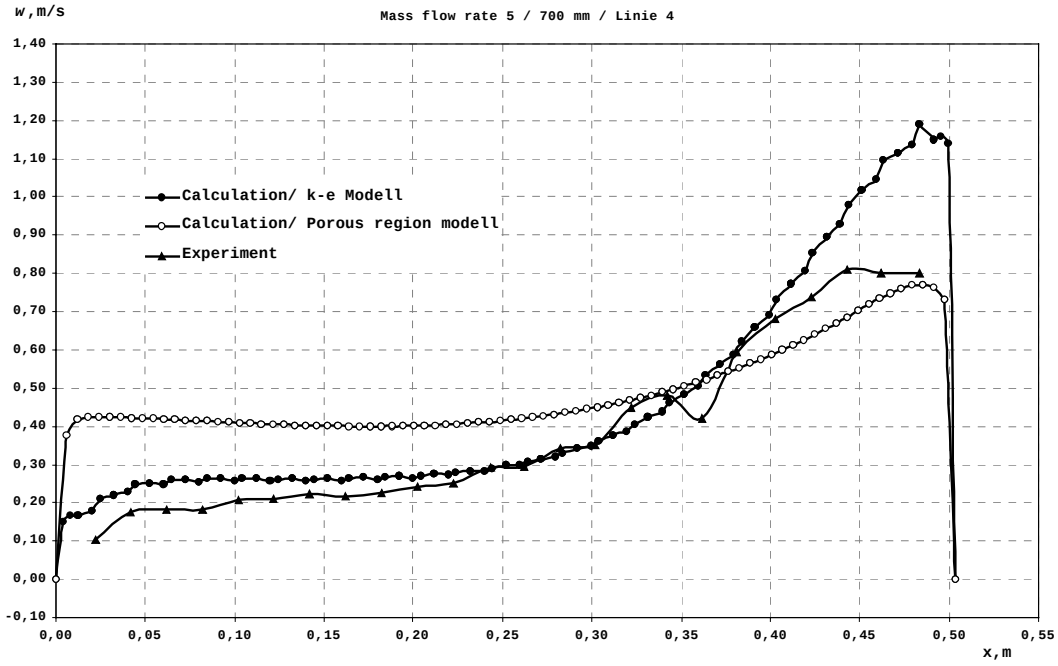

Fig. 5: Comparison of the calculation results with experimental data for the mass flow rate 5.

4. Discussion

The velocity profiles calculated with the porous region approach and the standard turbulence model show similar behaviour as in the experiment in most of the cases. As the fig. 4 shows the agreement between the calculation results and the experimental data for the second massflow rate at the highest measurement elevation is quite good. However, the comparison for the other elevations and massflow rates shows (see i.e. fig. 5) some deviations especially for the horizontal velocity component by a good agreement in general. Therefore some additional investigations have to be performed before drawing general conclusions.

The good agreement indicates a proper modelling of the flow field in the bundle by the implemented anisotropic porous body model. Noteworthy, that this anisotropic porous body model takes into account the anisotropy of the turbulent flow in the rod bundle due to the coefficients of the resistance tensor, the spatial anisotropy of the rod bundle is neglected.

The influence of the boundary condition at the outlet, in particular pressure boundary condition, on the flow field has to be examined. Also, it has to be tested, whether the results of the calculations with the porous media approach are of the same quality, when the mesh will be much coarser, what is more convenient for practical applications.

References

[1] M. Kliem, (2000), 3D flow simulations for a reactor core modelled as porous body using CFX-4.2, Proc. Ann. Meeting on Nucl. Technology 2000, (pp. 69-73), INFORUM GmbH, Bonn

[2] R. D. Lonsdale (1984), A simple turbulence model for flow in anisotropic porous media, Internal report, AEA Technology, ND-M-2947(D)

[3] S. Kliem, U. Grundmann, U. Rohde, (1998), Main Steam Line Break analysis of a NPP with VVER by means of the coupled code DYN3D/ATHLET, Proc. Ann. Meeting on Nucl. Technology 1998, (pp. 15-19), INFORUM GmbH, Bonn

NUMERICAL INVESTIGATION AND MEASUREMENT OF TRANSIENT TWO-PHASE BOILING IN A HEATED POOL

Eckhard Krepper

1. Introduction

The present paper was originated by safety assessments of dangerous liquids storage tanks against an external fire. As a consequence of an external heat source, the heat-up of the inventory may lead to the evaporation of the liquid and to release of significant quantities of dangerous gases into the environment. The liquid inventory behaves very differently depending on the mode of heating. Heating from the bottom of the tank leads to an irregular thermoconvective motion of the liquid, which causes good mixing, so that saturation is reached at all locations inside the tank approximately at the same time. If the tank is heated from the side however, a stable temperature stratification is observed leading to large temperature gradients. Evaporation at the surface can start much earlier than the average temperature reaches saturation. The scenario is very realistic for cylindrical barrels, which in vertical position stand on the bottom and are exposed to an external fire.

In the Forschungszentrum Rossendorf a lot of experiments of a bottom and of a side wall heated water tank, having a diameter of 0.25 m and a height of 0.21 m were performed. At different locations in the tank the temperature and the void fraction were measured (see [1], [2]). In order to clarify the physical nature of the heating up process in simple geometrical boundary conditions, first a two dimensional mathematical model was developed, which also includes evaporation and two phase flow (see [3]). The present paper deals with calculations using the CFD code CFX-4 which were performed recently (see [4]). The simulation comprises two phase flow, subcooled boiling at the heated side wall and steam release at the water surface.

2. CFX-boiling model

The subcooled boiling model, implemented into CFX-4 (see [5]) assumes incompressible flow at a fixed absolute pressure. The saturation temperature T_{sat} and the latent heat of evaporation H_{lg} are specified at this pressure. Constant properties at the saturation temperature are assumed for the steam and the liquid. Related to the liquid temperature T_l, the liquid subcooling $T_{sub} = T_{sat} - T_l$ and the liquid superheating $T_{sup} = T_l - T_{sat}$ are defined.

The heat source is assumed to be a heated wall. The boiling model calculates the partition of the given total heat flux Q into three parts:

$$Q = Q_f + Q_Q + Q_e \tag{1}$$

where $Q_f = h_f(T_w - T_l)$ = heat transfer rate due to convection, $Q_Q = h_Q(T_w - T_l)$ = heat transfer due to quenching, when a bubble detaches the wall and is replaced by subcooled water and Q_e = heat transfer due to evaporation; with T_w being the wall temperature, T_l the liquid temperature in the cell next to the wall and h_f and h_Q as the corresponding heat transfer

coefficients. For a given set of Q, T_{sub} and U_l (tangential velocity in the cell next to the wall) the bubble diameter at departure, the bubble departure frequency, the nucleation site density, the wall area fraction covered by liquid, the wall area fraction covered by vapour, the evaporation rate and the quenching heat transfer coefficient are calculated using corresponding correlations. During the heat flux partition algorithm, the composites of the given overall heat flux Q and the wall temperature T_w are calculated by iteration.

The rate of vapour generated at the wall is calculated by

$$\dot{m} = Q_e / H_{lg} . \tag{2}$$

The vapour is then assumed to be always at the saturation temperature. In the subcooled liquid ($T_l < T_{sat}$), heat flows from vapour to liquid and the bulk condensation is calculated by:

$$\dot{m} = max\left(\frac{h_{lg}(T_{sat} - T_l)A_{lg}}{H_{lg}}, 0\right) \tag{3}$$

In the superheated liquid ($T_l > T_{sat}$), all the heat flows from the liquid into the bubbles contributing to bulk evaporation:

$$\dot{m} = max\left(\frac{h_{lg}(T_l - T_{sat})A_{lg}}{H_{lg}}, 0\right) \tag{4}$$

A_{lg} is the interfacial area and h_{lg} the interphase heat transfer coefficient, which is calculated according the Ranz-Marshall correlation.

The model describes the heating up of a subcooled fluid until boiling occurs. It is assumed, that the liquid phase is continuous and the gas phase is in the form of disperse bubbles at saturation temperature. Kurul (1990, [5]) and Anglart and Nylund (1996, [6]) proposed to assume the bubble mean diameter d_p to be linearly dependent on the subcooling temperature T_{sub}:

$$d_p = \frac{d_1(T_{sub} - T_0) + d_0(T_1 - T_{sub})}{T_1 - T_0} \tag{5}$$

The recommended reference bubble diameters and subcooling are d_0=1.0e-4 m at a subcooling temperature of 13.5 K i.e. T_0=13.5 K and d_1=2.0e-3 m at a superheating temperature of 5 K i.e. T_1=-5 K (see [6]). The bubble diameter determines the drag force and the interfacial area.

3. CFX-calculations

The tank was modelled in two-dimensional cylindrical coordinates with 52 axial and 41 radial nodes. The radial nodes are unequally distributed with the minimum radial cell thickness near the wall of $5.0 \cdot 10^{-4}$ m.

The Euler/Euler approach was applied for the description of the establishing steam/water mixture the two fluid model. The Rayleigh Number was estimated in the order of $7.5 \cdot 10^{10}$. No turbulence was modelled. The drag of the bubbles according to the Ishii-Zuber viscous regime correlation was considered in the momentum equations. A non-slip boundary condition was set at the wall for the fluid phase while a free slip condition was set for the gas. Buoyancy was

considered using the Boussinesq approximation. The conservation equations were solved adopting a higher order discretisation scheme according to van Leer. For the time discretisation, a fully implicit backward time stepping procedure was used. Except for the pressure equation, the discretised equations were solved using a strongly implicit procedure according to Stone. The pressure equation was solved applying an Algebraic Multigrid Solver.

The vapour release into the environment at the upper surface was modelled introducing a degassing boundary. It acts as a vapour sink depending on the rising velocity of vapour and on the vapour volume fraction. The heat flux from the side wall into the water was reconstructed from temperature measurements and was given as a boundary condition.

During the first period of the transient, the problem was regarded as a single phase problem until the subcooling temperature T_{sub} falls below 15 K in the first cell of the volume. This occurs at the upper outer cell after about 810 s. Then a restart of the calculation was initiated applying the two phase models including the boiling model. The calculation was continued until convergence could not be reached at an increased vapour content at about 1220 s.

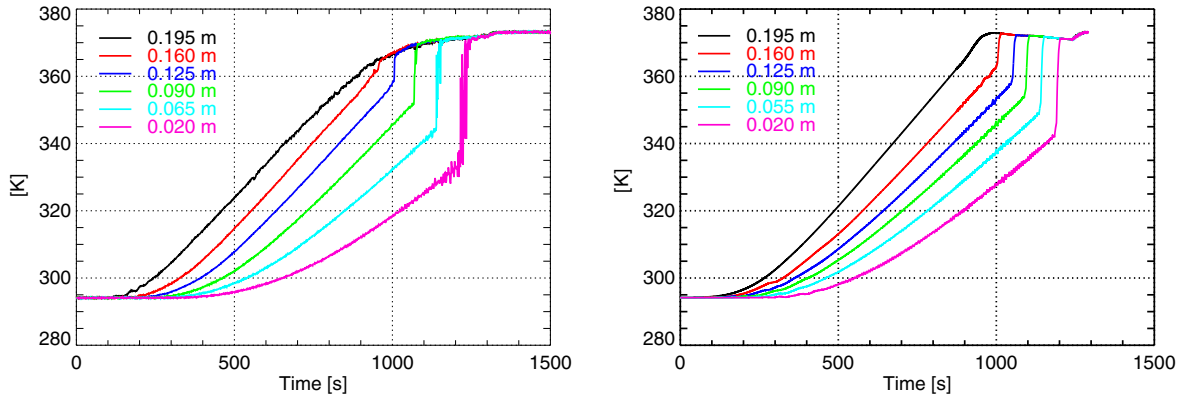

a) measured b) calculated

Fig. 1: Temperatures at different height levels in the centre of the tank

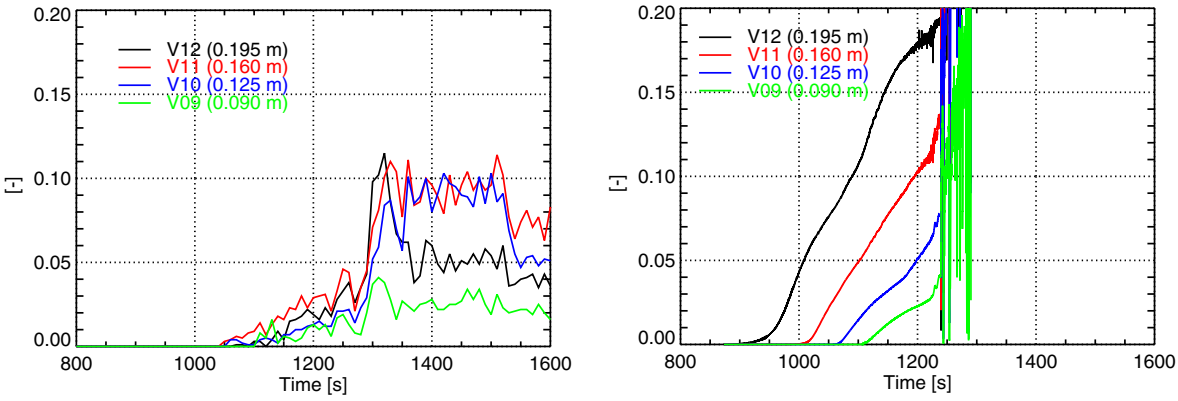

a) measured b) calculated

Fig. 2: Void fractions at different height levels at a wall distance of 1 mm

4. Results and discussion

Fig. 1 shows the measured and calculated temperatures in the centre of the tank at different levels. The strong temperature stratification observed in the experiment was confirmed by the calculations too. The measured temperature courses show subsequent temperature jumps, which are modelled in qualitatively good accordance to the experiment. An explanation of the jumps will be given below.

Fig. 2 shows the measured and calculated void fraction signals near the wall. Boiling is found first at the probe V12 (highest level, 1 mm wall distance) in the measurements at 1050 sec and in the calculations at 920 sec. The deviation could be explained by the measurement probe size. The probes had a diameter of 1 millimetre. Therefore they are not capable of detecting bubbles with a diameter smaller than about 1.5 millimetres. During the tests, small bubbles were seen at the wall already after about 950 seconds. Also the typical noise at subcooled boiling was detected. The large gradient of the void fraction near the wall and the sensitive influence of the probe location might be a further explanation for the discrepancy.

The experimental data and

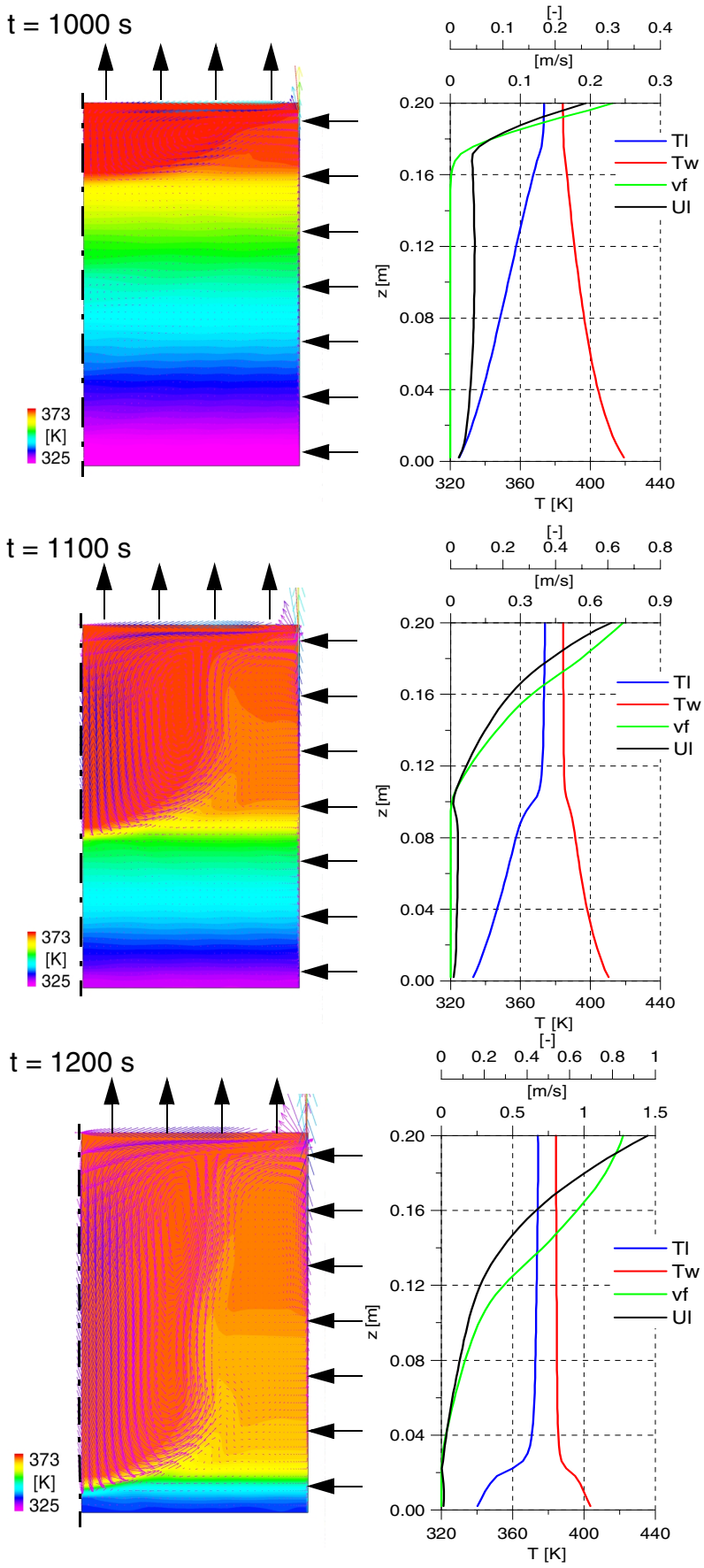

Fig. 3: Calculated temperature and velocity field and parameter at the heated wall

the calculated results give a deeper insight into the physical processes during the heating-up. Fig. 3 represents on the left side the temperature and velocity distribution in the tank after 1000 s, 1100 s and 1200 s. Heating from the side walls and steam degassing at the top are marked by arrows. The right side of Fig. 3 shows the parameter of the heated wall. The liquid temperature T_l, the void fraction *vf* and the fluid velocity U_l are the parameters of the first cell near the wall. The wall temperature T_w is calculated by the boiling model.

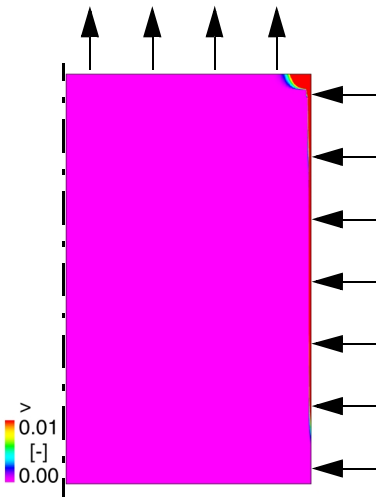

Fig. 4: Calculated volume fraction distribution after 1200 s

During the first few hundreds seconds of the test, remarkable upward movement of the fluid is observed only in a thin layer near the wall. Correspondingly there is only a slow downward movement in the bulk of the tank. Heated fluid is transported to the upper surface and a quite stable temperature stratification is established. After the first occurrence of boiling at the upper part of the side wall the rising steam accelerates the fluid. This is clearly reflected by the wall parameters on the right side of Fig. 3. The temperature stratification is mixed up by the generated steam. Fig. 3 shows the well mixed upper region at saturation temperature, a horizontal boundary and a lower region showing the remaining temperature stratification. Above the boundary a strong upward movement at the wall and a strong downward movement in the centre is established. Further heating up, the boundary moves gradually downward. In Fig. 3, the boundary is found at 0.17 m after 1000 s, at 0.10 m after 1100 s and after at 0.04 m 1200 s. When the boundary crosses a thermocouple, the measurement shows a temperature jump. This explains the temperature jumps. Remarkably amounts of vapour are found only in a thin layer near the heated wall during long periods of the transient (see Fig. 4 after 1200 s). When finally the boundary reaches the bottom of the tank and the downward velocity in the centre exceeds the bubble rising velocity, the whole tank is well mixed and pool boiling occurs. Then a second temperature jump is observed in the measured temperature course after 1300 s (see Fig. 1a). The calculations however yielded reasonable results only up to about 1220 sec. The last phenomenon could not be simulated since convergence could not be achieved. The slight decreasing of the maximum fluid temperature after the corresponding jump seen in Fig. 1b could not be explained.

5. Conclusions

The code CFX-4 and the implemented boiling model are capable of simulating a transient two phase phenomenon including subcooled boiling. Numerical problems were solved for low volume fractions by large iteration number per time step and by underrelaxation. The numerical effort compared to a single phase situation is enhanced by a factor of about 10. Situations with higher void fraction in the last period of the transient could not be simulated.

There is criticism found in the literature against the simplified linear dependence of the bubble diameter on the subcooling temperature according eq. (5) (see [7]). The correlations to describe creation, growth and detachment of bubbles should be reviewed and validated by additional experiments.

References

[1] A. Aszódi, E. Krepper and H.-M. Prasser (2000), Experimental and numerical investigations of one and two phase natural circulation in storage tanks, Heat and Mass Transfer 36, 497-504

[2] A. Aszódi, E. Krepper, H.-M. Prasser (1999), Investigation of heating up and evaporation processes in storage tanks by experiments and by numerical investigations, Proceedings of the Second International Symposium on Two-Phase Flow Modeling and Experimentation Pisa, Vol. III, pp. 1667

[3] A. Aszódi (1997), Modelling of transient natural convection – Thermal-hydraulic analysis for an accident of dangerous fluid storage tanks, PhD. Thesis, Technical University Budapest

[4] E. Krepper, A. Aszódi, H.-M. Prasser (2001), Experimental and numerical investigations of one and two phase natural circulation in storage tanks, 4th International Conference on Multiphase Flow, New Orleans, May 2001, paper 515

[5] Kurul, N., M. Z. Podowski (1990), Multidimensional effects in sub-cooled boiling, Proc. of 9'th Heat Transfer Conference

[6] H. Anglart, O. Nylund (1996), CFD Application to prediction of void distribution in two-phase bubbly flows in rod bundles, Nuclear Science and Engineering 163, 81-98

[7] J. Y. Tu (1999), Improvement of a two-fluid model for predicting subcooled flow boiling at low pressure, NURETH-9, San Francisco, October 1999

TESTING OF NEUTRON DATA LIBRARIES IN APPLICATION TO REACTOR PRESSURE VESSEL DOSIMETRY

Bertram Böhmer, Gennady Borodkin[1], Jörg Konheiser und Gennadi Manturov[2]

1. Introduction

The fast neutron induced embrittlement of the reactor pressure vessel (RPV) is the main cause limiting the lifetime of many types of nuclear reactors, especially of the VVER type, producing most of the nuclear energy in Russia and seven other countries. As the reactor lifetime is directly proportional to the fast neutron fluence at the RPV, the uncertainty of that fluence has important economic and safety consequences. Uncertainty estimations show that the largest contribution to the uncertainty of calculated fluences is the uncertainty of the neutron cross section data. In the present work, different aspects of uncertainties of up-to-date neutron fluence determination connected with the neutron data for transport calculations, data preparation methods and activation dosimetry cross sections have been investigated by comparison of calculations with data from different libraries and by comparison of calculated and measured activation reaction rates.

2. Calculational Methods

Most of the calculations were performed by the discrete ordinate code DORT using a 3D synthesis of (R-Θ)-, (R-Z)- and R-calculations. For the 3D synthesis of the flux in group g the relation

$$\Phi_{\mathrm{g}}(\mathrm{R},\Theta,\mathrm{Z}) = \Phi_{\mathrm{g}}(\mathrm{R},\Theta)\cdot\frac{\Phi_{\mathrm{g}}(\mathrm{R},\mathrm{Z})}{\Phi_{g}^{1D}(\mathrm{R},\Theta)}$$

was applied, where $\Phi_g(R,\Theta)$, $\Phi_g(R,Z)$ and $\Phi_g^{1D}(R,\Theta)$ are 2D flux density distributions obtained by DORT. $\Phi_g^{1D}(R,\Theta)$ was calculated using the same (R,Θ) space grid, as for the calculation of $\Phi_g(R,\Theta)$, but for a 1D cylindrical R-model. The advantage of this procedure is a reduction in non-physical Θ oscillations. Results produced by the Monte Carlo code TRAMO [1] with a 123 fast neutron group library based on ENDF/B-VI data (TRAMO/B-VI) were applied to validate the DORT results for reactor calculations. The Monte Carlo code MCNP [2] allowed to investigate the influence of the group approximations used with DORT and TRAMO on the fluence results.

3. Neutron fluence calculations for Balakovo-3

3.1. The reactor

The main object of these investigations was the VVER-1000 type reactor of the Balakovo NPP, unit 3 (Balakovo-3). For the 5th cycle of that reactor detailed operation and source data as well as geometry and material data were available. During the same cycle activation

[1] SEC for Nuclear and Radiation Safety of GOSATOMNADZOR, Moscow, Russia
[2] SSC RF Institute of Physics and Power Engineering, Obninsk, Russia

detectors of 8 participants of an international intercomparison experiment [3] had been irradiated in the cavity between reactor pressure vessel and thermal insulation.
The positions of the detectors are shown on the horizontal cross section of the 60° symmetry sector of the reactor in Fig. 1.

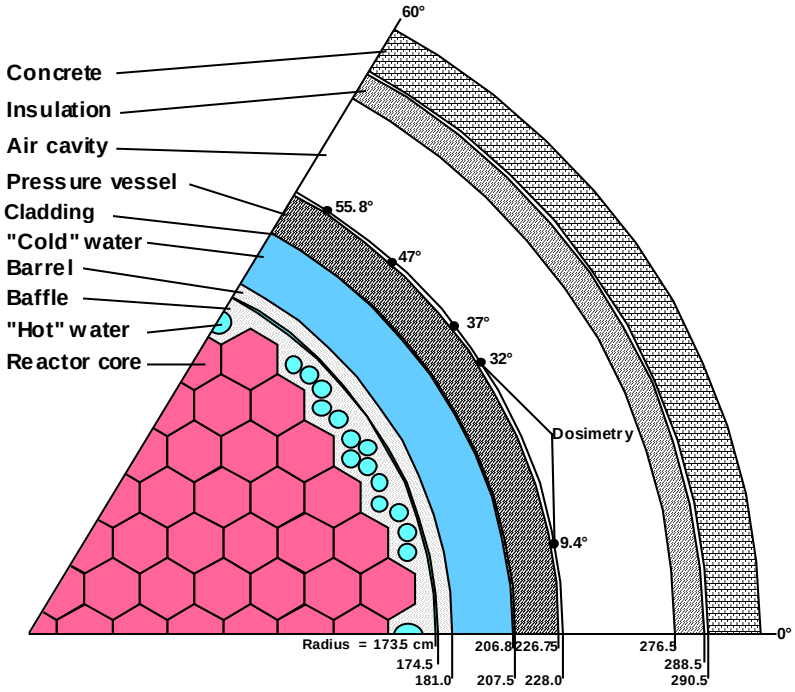

Fig. 1: Horizontal cross section through the 60° symmetry sector of Balakovo-3 with dosimetry positions

3.2. Comparison of fluence calculations

The following libraries were tested: the ENDF/B-VI based 47n/20g-group library BUGLE-96 [4], the Russian 299n/15g-group library ABBN-93 [5], version 99.01, named ABBN/Original, and two modifications of the ABBN library: ABBN/B-VI and ABBN/JEF2.2. In these modifications the cross section data of Fe, Cr and Ni were replaced by data based on the evaluated nuclear data libraries ENDF/B-VI and JEF-2.2, respectively. This allows to investigate the influence of the data for the elements most critical for the RPV fluence. The test was based on the comparison of several fluence integrals and reaction rates important for pressure vessel embrittlement as well as of fluence spectra at the inner and outer walls of the RPV. Although thermal neutrons contribute only negligibly to the embrittlement they are a major source of gamma irradiation, probably having a non-negligible effect on PV embrittlement, as newer results indicate. Therefore, the influence of different treatment of neutron data in the thermal energy region was investigated by calculations with and without upscattering in the region below 5 eV, as well as with and without consideration of core heterogenity effects. Neutron spectrum calculations with DORT/BUGLE-96 for the inner RPV wall considering upscattering resulted in an flux integral below 0.414 eV increased by

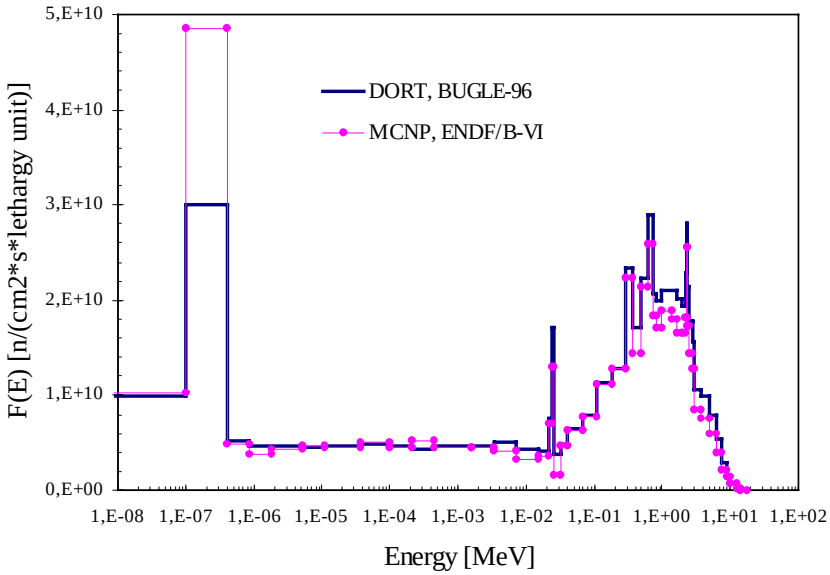

Fig. 2: DORT Synthesis/BUGLE-96 and MCNP/ENDF/B-VI neutron spectra at the inner RPV wall of Balakovo-3

about 40%. Thereby, the flux integral below 0.1eV decreased slightly and the flux integral from 0.1 to 0.414eV increased by an order of magnitude. The upscattering was taken into account in all further calculations involving thermal neutrons. The effect of a rigorous pointwise treatment of neutron cross sections for all neutron energies including the thermal region was studied by comparison of MCNP/ ENDF/B-VI and DORT/BUGLE-96 results for the inner wall of the Balakovo-3 RPV (Fig.2). The obtained fluxes are comparable as in both calculations the same 3D model was used and for the calculated midplane position the DORT synthesis supplies accurate results. The MCNP results are somewhat smaller in the fast energy region but considerably higher in the thermal region. The influence of different data variants on the midplane flux above 0.5 MeV calculated with the help of a cylindrical reactor model in dependence on the radial position is shown in Fig.3.

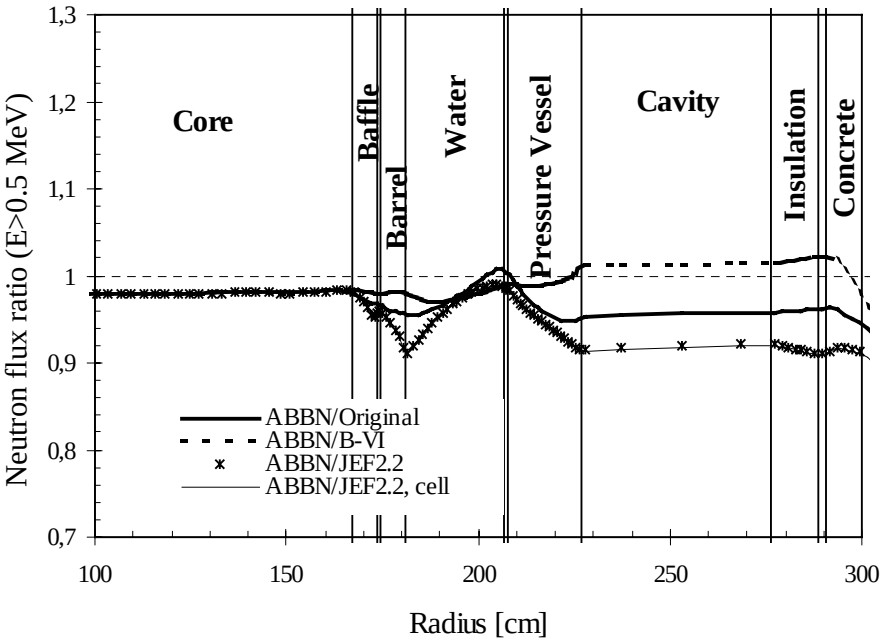

Fig. 3: Ratio of neutron fluxes (E>0.5 MeV) calculated with different libraries to the flux obtained with BUGLE-96 at different radial positions

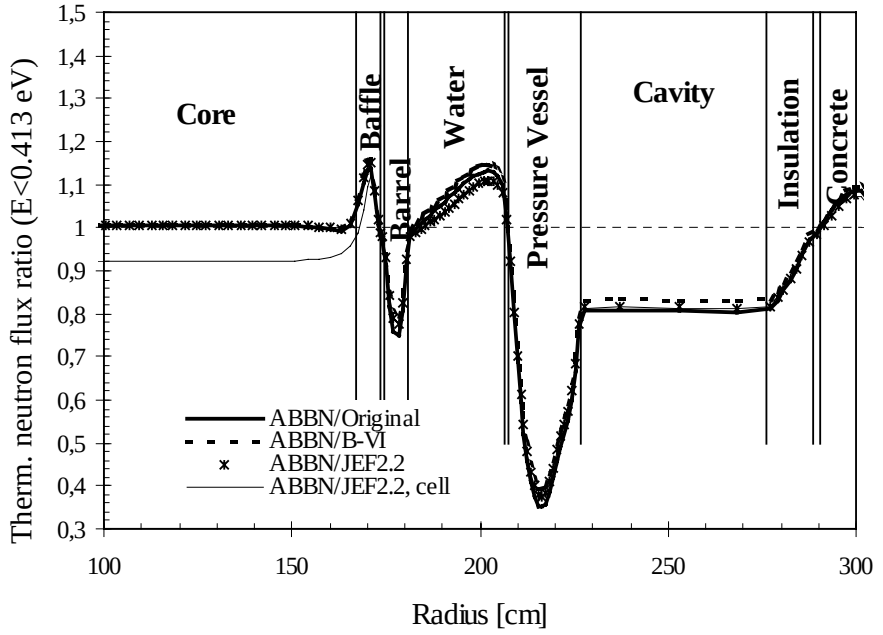

Fig. 4: DORT calculated thermal neutron flux (E<0.413 eV) ratio per BUGLE-96 calculation in radial direction of the VVER-1000 Balakovo-3

The differences between the results with different libraries are in the order of 10% or less. The ABBN/B-VI based results are closest to the BUGLE-96 ones. As expected, the effect of the core heterogenity considered in the ABBN/JEF2.2, cell library is negligible for fast neutrons. The corresponding ratios for thermal neutrons, shown in Fig. 4**,** display large discrepancies

between BUGLE-96 and all ABBN based libraries especially inside the pressure vessel, where the BUGLE-96 result is up to 2.6 times higher than the ABBN results. The core heterogenity changes the thermal flux only in the core region due to the short range of the thermal neutrons. Noteworthy is the good agreement of flux results for all libraries at the inner surface of the RPV demonstrating that agreement in one point is no proof of agreement everywhere.

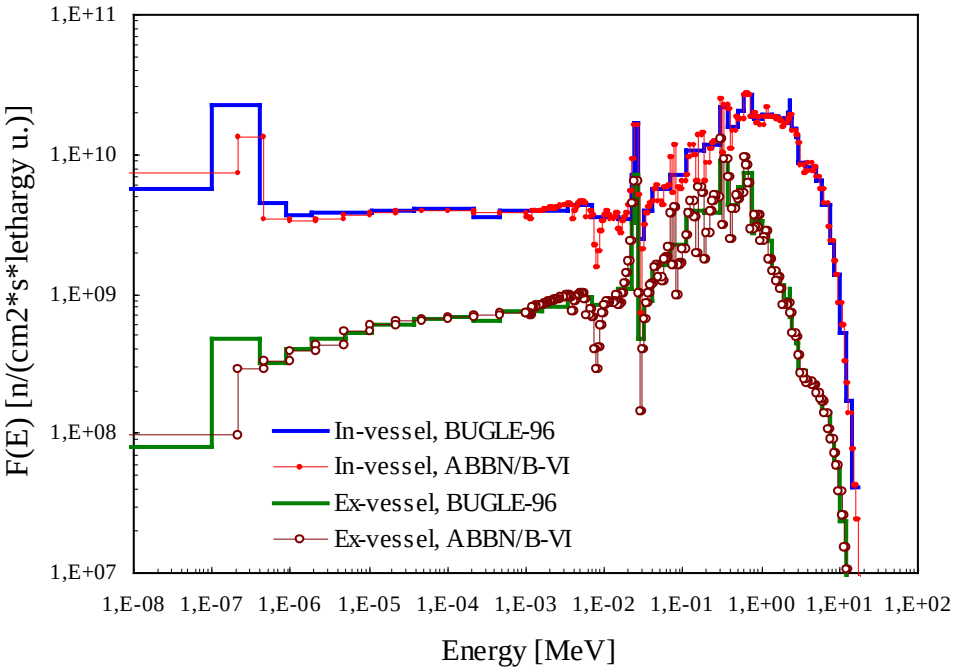

Fig. 5: DORT (R,Θ) neutron spectra at two Balakovo-3 positions calculated with ABBN/B-VI and BUGLE-96

For two important Balakovo-3 RPV positions - the inner and outer wall midplane azimuthal maxima - a reasonable agreement of the absolute neutron flux spectra calculated by DORT with ABBN/B-VI and BUGLE-96 can be observed in Fig. 5.

3.3. Comparison of calculations with experiments

The results of calculations of activation reaction rates at ex-vessel positions were compared with reference data of the Interlaboratory Activation Experiment at Balakovo-3. IRDF-90v2 [6] was used as dosimetry library. It can be seen from Fig. 6 that for the threshold reactions: ^{237}Np(n,f), ^{93}Nb(n,n'), ^{238}U(n,f), ^{58}Ni(n,p), ^{54}Fe(n,p), ^{46}Ti(n,p) and ^{63}Cu(n,α) a similarly good agreement between results of calculations (C) and experiments (E) was obtained for DORT/BUGLE-96, DORT/ABBN/B-VI, and TRAMO/B-VI results.

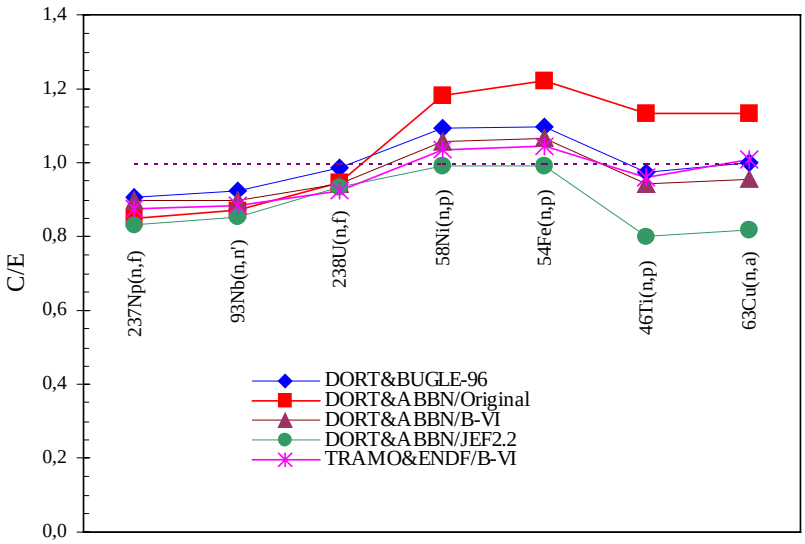

Fig. 6: Position-averaged C/E data for Balakovo-3 ex-vessel experiment for different calculation variants using IRDF-90v2 dosimetry cross sections

4. Impact of dosimetry cross sections on RPV fluence results

Dosimetry cross sections are important for C/E comparisons and for the calculation of fluences from activation rates using the method of effective cross sections or adjustment methods. The effect of different dosimetry cross section libraries (IRDF-90v2, JENDL/D-99 [7], RRDF-98 [8] and a new Russian evaluation for ^{237}Np(n,f) [9] on C/E data for activation rates of the Balakovo-3 ex-vessel experiment was investigated using different neutron transport calculations. Tables 1 and 2 show the C/E comparison results.

Table 1: Position-averaged C/E for reaction rates of Balakovo-3 experiment and 3D synthesis DORT/BUGLE-96 calculations for different dosimetry cross section libraries

Reaction	IRDF-90v2	JENDL-D99	RRDF-98	BUGLE-96
^{237}Np(n,f)	0.907	0.943	0.951	0.857
^{93}Nb(n,n')	0.923	0.982	0.932	
^{238}U(n,f)	0.986	0.997		0.995
^{58}Ni(n,p)	1.092	1.069		1.094
^{54}Fe(n,p)	1.097	1.111		1.100
^{46}Ti(n,p)	0.974	1.069	1.069	1.034
^{63}Cu(n,α)	0.998	1.018	1.005	0.993

Table 2: Position-averaged C/E for reaction rates of Balakovo-3 experiment for 3D synthesis DORT/ABBN/B-VI and TRAMO/ENDF/B-VI calculations using different dosimetry cross section libraries

Reaction	DORT/TRAMO IRDF-90v2	DORT/TRAMO JENDL-D99	DORT/TRAMO RRDF-98
^{237}Np(n,f)	0.895 / 0.876	0,938 / 0.910	0.945 / 0.918
^{93}Nb(n,n')	0.900 / 0.883	0.955 / 0.937	0.898 / 0.889
^{238}U(n,f)	0.941 / 0.926	0.951 / 0.936	
^{58}Ni(n,p)	1.057 / 1.036	1.034 / 1.014	
^{54}Fe(n,p)	1.066 / 1.043	1.079 / 1.057	
^{46}Ti(n,p)	0.943 / 0.961	1.036 / 1.053	1.035 / 1.054
^{63}Cu(n,α)	0.954 / 1.010	0.974 / 1.023	0.960 / 1.017

The systematic calculational underestimation for ^{237}Np(n,f) in case of IRDF-90v2, observed also by other investigators, can be largely reduced using JENDL/D-99 or the new Russian evaluation. The improvement is caused by higher cross sections in the region below 0.1 MeV in these two data sets. A similar underestimation of experimental results by calculations for ^{93}Nb(n,n') disappears mostly if JENDL/D-99 data are used.

5. Calculations for one-dimensional 2-zone models

To evaluate the influence of cross sections of individual elements and water on the neutron fluence calculation, simple two-zone cylindrical models were defined. Their inner zone simulates the reactor core, the outer consists of Fe, Cr, Ni or H_2O. In addition to DORT calculations with different libraries MCNP/ENDF/B-VI calculations were performed, to test the influence of a pointwise data representation.

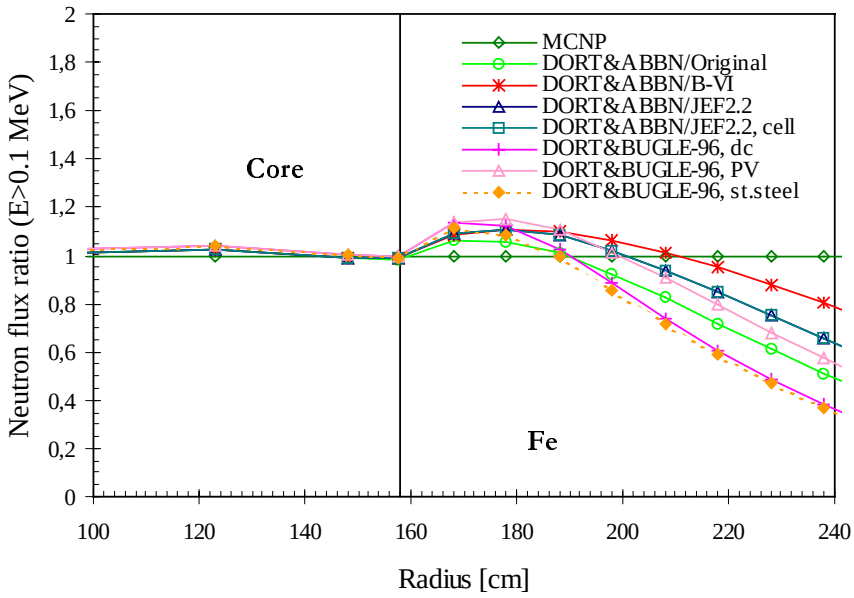

Fig. 7: Fe zone model: Ratio of DORT to MCNP results for neutron flux (E>0.1 MeV)

Ratios of the flux integrals (E>0.1 MeV) calculated with DORT and different cross section sets to the flux integrals obtained with MCNP are shown in Fig. 7 for the Fe zone model. The three different BUGLE-96 cross section variants are related to 3 different environments of the Fe atoms: downcomer (dc), RPV and stainless steel. There is a reasonable agreement within limits of ±20% for depths up to 20 cm (real RPV thickness). A similar agreement was found for fast neutrons in H_2O, Cr and Ni zones.

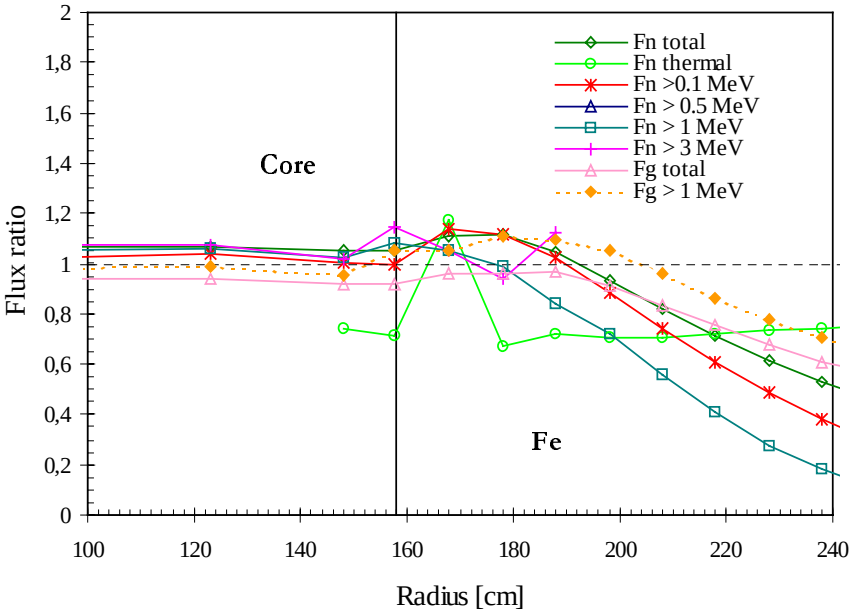

Fig. 8: Ratio of DORT/BUGLE-96(dc) to MCNP/B-VI neutron and gamma flux integrals

Fig. 8 demonstrates the impact of the group approximation on neutron and gamma flux integrals by comparing results of DORT/BUGLE-96 and MCNP/ENDF/B-VI calculations for the Fe zone model. For thermal neutrons there are unsystematic discrepancies for all outer zone materials. The reasons of the large discrepancies for all functionals at outer zone depths above 20 cm, especially for the Cr and Ni zones should be further investigated. Partly they will be caused by the group approximation.

6. Conclusions

Comparing results obtained with different basic nuclear data, data preparation methods, dosimetry cross sections and experiments, maximum discrepancies in the order of 20% were obtained for fast neutron fluences in the reactor pressure vessel region. The ABBN/B-VI library delivered similar results as BUGLE-96 and was found to be suitable for RPV dosimetry applications. For low energy neutrons and deeper penetrations considerable discrepancies were found requiring further investigations. There is an urgent necessity for new experimental benchmark data to check low energy neutron and gamma spectrum calculations in the ex-core reactor region.

References

[1] H.-U. Barz, B. Böhmer, J. Konheiser, I. Stephan, High-Precision Monte Carlo Calculations, Experimental Verification and Adjustment of Fluences in the Pressure Vessel Cavity of a VVER-1000, Proc. 1998 ANS Radiation Protection and Shielding Division Topical Conference Technologies for the New Century, April 19-23, 1998, Nashville, Tennessee, USA, Vol. 1, p. 447-454

[2] J.F. Briesmeyer, MCNP - A general Monte Carlo n-particle transport code (Version 4A), Manual, LA-12625-M (1993)

[3] Borodkin, G. I., Kovalevich, O. M., Barz, H.-U., Böhmer, B., Stephan, I., Ait Abderrahim, H., Voorbraak, W., Hogel, J., Polke, E., Schweighofer, W., Seren, T., Borodin, A. V., Vikhrov, V. I., Lichadeev, V. V., Markina, N. V., Grigoriev, E. I., Troshin, V. S., Penev I., and Kinova, L., Balakovo-3 Ex-vessel Exercise: Intercomparison of Results, *Reactor Dosimetry: Radiation Metrology and Assessment, ASTM STP 1398*, American Society for Testing and Materials, West Conshohoken, PA, 2001, pp. 320-327.

[4] J.E. White et al., BUGLE-96: A Revised Multigroup Cross Section Library for LWR Applications Based on ENDF/B-VI Release 3, ANS Rad. Prot. & Shielding Topical Meeting, Falmouth (April 1996).

[5] G.N. Manturov, M.N. Nikolaev, A.M. Tsiboulya, BNAB-93 Group Data Library. Part I: Nuclear Data for the Calculation of Neutron and Photon Radiation Fields, INDC(CCP)-409/L, August 1997, p.65-110.

[6] N.P. Kocherov and P.K. McLaughlin, The International Reactor Dosimetry File (IRDF-90), *Report IAEA-NDS-141*, Rev.2, IAEA, Vienna, October 1993.

[7] JENDL Dosimetry File 99 (JENDL/D-99), *JAERI*, 1999, IAEA distributed nuclear data, (1999).

[8] S.A. Badikov, et al., Status of Russian Dosimetry File, *Proc. of the 9th International Symposium on Reactor Dosimetry*, Sept. 2-6, 1996, Prague, Czech Republic. Hamid Ait Abderrahim et al. Eds., World Scientific Publishing Co. Pte. Ltd., 1998, pp. 480-488.

[9] S.A. Badikov, K.I. Zolotarev et al., Analysis of Discrepancies in Evaluated Data for Np-237 and Development of the Improved Evaluation, *Voprosy Atomnoi Nauki i Tekhniki*, Seria: Yadernye Constanty, 1997, V. 3-4, p.59.

RESULTS OF COLUMN AND BATCH INVESTIGATIONS OF GYPSUM WEATHERING

Roland Kuechler, Klaus Noack and Torsten Zorn

1. Introduction

Often, chemically aggressive seepage water is the cause of the mobilisation of pollutants and radionuclides in the unsaturated zone. This results from the weathering of minerals which form stronger acids or lyes. For the forecast of the groundwater pollution and contamination of radionuclides it is therefore important to know the solution kinetic for decisive minerals in the unsaturated zone. In the literature the dissolution of minerals is described with rate laws, usually determined with the rotating disk method under water saturated conditions. The verification of this rate laws for the unsaturated transport by column experiments is an important task to come to a realistic modelling. This contribution reports on a gypsum weathering experiment, presents and discusses the most important experimental results and compares them with results of computations.

2. Batch and column experiments with gypsum

The principles of the batch and column experiments are described in [1]. The gypsum used in the experiments is a natural gypsum (Marienglas) from Rocastrada, Italy. To check the purity of the mineral the powder was investigated with Scanning Electron Microscopy/Energy Dispersive Spectrometry (SEM/EDS) and X-ray Powder Diffraction (XRD). The gypsum solution was analysed with Inductive Coupled Plasma-Mass Spectrometry (ICP/MS). The ICP/MS analyses showed small iron impurities in the gypsum, but no other noticeable impurities. The gypsum was prepared in the following way. After crushing and dry sieving the grain size was in the range between 200-300 µm. Then the powder was washed with MilliQ-water and dried at a temperature of 50 °C to remove small particles. This gypsum powder was used in the batch and the column experiment.

To observe the dissolution of gypsum in batch experiments a defined mass of a few grams of this powder was mixed with 400 mL MilliQ-water and the electrolytic conductivity κ was monitored. The conductivity is a combination of the several ion concentrations which the dissolution process caused. Fig. 2 illustrates the influence of different masses of gypsum on the time curve of the conductivity. The equilibrium values are close to each other: 2.11 mS/cm and 2.12 mS/cm for washed gypsum. They well agree with the calculated value of κ = 2.15 mS/cm. The results of the chemical analyses of the solutions related to the pH-values, calcium and sulphate concentrations are summarized in Table 1. The solutions were filtered through a filter with 0.2 µm pore size. These results show the nearly neutral reaction of gypsum with MilliQ-water. The measured calcium and sulphate concentrations in the equilibrium well agree with the measured calcium concentrations of Marienglas as published in [2]. The 1:1 ratio of calcium and sulphate in the solution of gypsum was also found.

In the column experiments sea sand was used as matrix. To achieve inertness of the sand against the gypsum-water solution it was washed with MilliQ-water because the reaction of the gypsum solution will be neutral. The gypsum powder and the sand were mixed in the ratio of 2 g per 1 kg. Fig. 1 shows the results of electrolytic conductivity and pH measurements of

the solution leaking from the 1 m-column over a time period of 70 days after of the water breakthrough. Table 2 gives the results of the chemical analysis of the solutions for steady state water flow at various heights in the column.

Table 1: Chemical analyses of the solutions at the pH, calcium and sulphate concentrations of the batch experiments at equilibrium

Batch experiments	pH-value	Sulphate / mmol/L	Calcium / mmol/L
1 g gypsum	6.2	14.8	15.1
3 g gypsum	6.0	15.4	15.7

Table 2: Analytical measurements of the solutions at steady-state water flow in dependence on the height of the 1 m-column

Height	pH-value	κ / mS/cm	Calcium / mmol/L	Sulphate/ mmol/L
30 cm	5.32	0.17	0.44	to small volume for Ion Chromatography
50 cm	4.58	1.81	10.73	
70 cm	4.45	2.21	15.34	
90 cm	4.22	2.24	14.67	14.96
Outflow (100 cm)	3.90	2.22	15.44	16.45

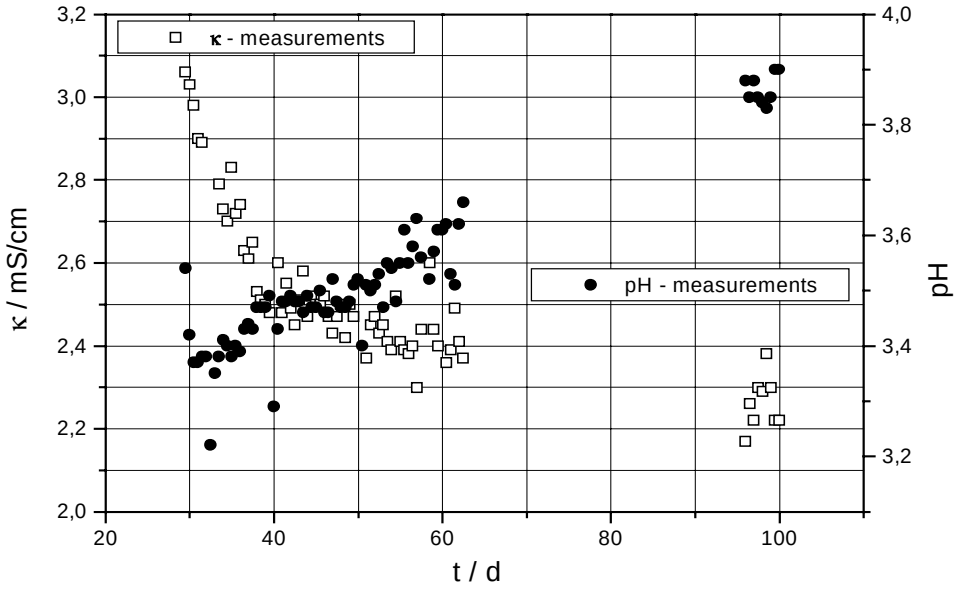

Fig. 1: pH-value and electrolytic conductivity of the solution leaking from the 1 m-column in dependence on time after start of water injection

The values in Table 2 were determined at the end of the column experiment. At the measuring points samples were taken through lockable windows. Solution and solid portions of these

samples were separated by centrifugation. The κ-values measured for these solutions were also used for the calibration of the conductivity in Fig. 4.

Fig. 1 also shows the influence of the sand matrix on the leaking solution over a time period of 62 days. In this time interval the κ-values are higher than the κ-value of the saturated gypsum solution. As result, it must be concluded that the sea sand is not perfectly inert against mineral dissolution. The analyses by ICP/MS for the cations and by Ion Chromatography (IC) for the anions confirmed this fact, but this influence becomes weaker with time. There is a good agreement at the outlet of the column with the measured κ-values at the batch experiments in equilibrium (Fig. 2). The measured pH-values (Fig. 1 and Tab. 2) show a weak acid reaction of the used sea sand matrix increasing with the transport path length of the water. Thus, the pH-values are not in the neutral pH-range. Furthermore, the κ-values and the calcium concentrations (Tab. 2) show the gypsum extraction in the water unsaturated part of the column after the long time period of 100 days. In the considered time period the electrolytic conductivity and the measured concentrations of calcium and sulphate in the water saturated part accept the values of the gypsum equilibrium.

3. Modelling of batch and column experiments

In batch tests storage and dissolution processes proceeding in water and soil samples are analysed. The following system of coupled ordinary differential equations (ODEs) describes the dynamics of the chemical system in these tests[3]:

$$\frac{dC_i}{dt} = \eta \frac{F_p}{V_s} r_{ip}(solution) + \sum_{j=1}^{m} W_{i,j}(C_1,\ldots,C_m) \qquad i = 1,\ldots,m \tag{1}$$

where C_i is the concentration of the ion species i, F_p the total surface area of the mineral particles p, V_s the volume of the solution and r_{ip} is the dissolution rate of the chemical component i from the surface of mineral p. m denotes the number of components and species which are involved in the reactions. In general, the dissolution rate depends on the chemical composition of the solution dissolving the mineral, for example on its pH-value. $\sum W_{i,j}$ can be viewed as the interaction rate to maintain the fast reactions in the water phase in equilibrium. This term determines the composition of the chemical solution on the basis of the mass action laws and acts also as source or sink. With the dissolution of the mineral grains their surface also decreases. This process is described by the function:

$$\eta(t) = \left(\frac{m(t)}{m_0} \right)^{\beta} = \left(\frac{\rho_M(t)}{\rho_{M0}} \right)^{\beta}, \tag{2}$$

where $m_0 = \rho_{M0} V$ is the initial mass of mineral, V is the considered volume element, $m(t)$ is the mass of mineral at a given time, and β is a geometry factor which indicates the dependence of the surface on the volume or mass. For ball, cube and all regular polyhedrons $\beta = 2/3$ applies. The ratio of real area to geometric area is referred to as the surface roughness. It changes with time as a mineral weathers because during the solution process edges and sharp peaks are more strongly attacked than smooth surfaces. Therefore a larger value for β is to be expected.

In the column tests transport, storage, exchange, and dissolution/precipitation processes are investigated. The evaluation of experimental data is based on the complete one-dimensional

migration model. Assuming a constant flow rate v of the solution through the column the system of transport equations (PDEs) for the species is [4]:

$$n \cdot s(x) \frac{\partial C_i}{\partial t} = -v \frac{\partial C_i}{\partial x} + \alpha_L v \frac{\partial^2 C_i}{\partial x^2} + \eta \frac{F_p}{V} r_{ip}(solution) + \sum_{j=1}^{m} W_{i,j}(C_1, \ldots, C_m), \quad i = 1, \ldots, m. \quad (3)$$

Here $n \cdot s(x)$ means the soil water content, n is the porosity and s the water saturation of the pores, v the Darcy velocity per unit area , α_L the longitudinal dispersion length (dispersivity) of the medium, and V the matrix volume. In this case

$$\eta = \left(\frac{\rho_M(x,t)}{\rho_{M0}} \right)^{\beta} = \left(1 - \frac{1}{\rho_{M0}} \int_0^t \frac{\partial j}{\partial x} dt \right)^{\beta} \quad (4)$$

also considers the reduction of the surface with decreasing mineral mass. ρ_{M0} is the initial molar density, $\rho_M(x,t)$ is the molar density at given time and space, and β is the geometry factor explained above. For the current j the appropriate components are to be used which register the moles of mineral flowed away.

For the surface controlled dissolution and precipitation reactions of gypsum the rate equations of Inskeep and Bloom [5] is used:

$$q_{Ca^{2+},gypsum} = q_{SO_4^{2-},gypsum} = q_{gypsum}(1 - \frac{\gamma_2^2 C_{Ca^{2+}} C_{SO_4^{2-}}}{K_{SP}}), \quad (5)$$

where q_{gypsum} designates the forward reaction rate which has no dependence on any species in solution and the term in the parentheses takes into account the effects of back reaction as equilibrium is approached, and assures that $q_{i,gypsum} = 0$ at equilibrium. This yields the mixed kinetic-equilibrium system (1) for the gypsum dissolution:

$$\begin{aligned}
&\frac{dC_i}{dt} = \sum W_{i,j}\ , \quad \text{i} = \text{H}^+,\ \text{OH}^-,\ \text{HSO}_4^-,\ \text{H}_2\text{SO}_4,\ \text{CaSO}_4,\ \text{j} = \text{all species} \\
&\frac{dC_{Ca^{2+}}}{dt} = \eta \frac{F_{gypsum}}{V_s} q_{gypsum}(1 - \frac{\gamma_2^2 \cdot C_{Ca^{2+}} \cdot C_{SO_4^{2-}}}{K_{sp}}) + \sum W_{Ca^{2+},j} \\
&\frac{dC_{SO_4^{2-}}}{dt} = \eta \frac{F_{gypsum}}{V_s} q_{gypsum}(1 - \frac{\gamma_2^2 \cdot C_{Ca^{2+}} \cdot C_{SO_4^{2-}}}{K_{sp}}) + \sum W_{SO_4^{2-},j},
\end{aligned} \quad (6)$$

$$\left[\begin{array}{lll}
W_{1,2} = W_{2,1} & \approx & \gamma_1^2 C_{H^+} \cdot C_{OH^-} - K_W \\
W_{1,3} = W_{3,1} = -W_{4,4} & \approx & \gamma_2 C_{H^+} \cdot C_{SO_4^{2-}} - K_1 \cdot C_{HSO_4^-} \\
W_{1,4} = W_{4,1} = -W_{5,5} & \approx & \gamma_1^2 C_{H^+} \cdot C_{HSO_4^-} - K_2 \cdot C_{H_2SO_4} \\
W_{3,6} = W_{6,3} = -W_{7,7} & \approx & \gamma_2^2 C_{Ca^{2+}} \cdot C_{SO_4^{2-}} - K_3 \cdot C_{CaSO_4}
\end{array} \right],$$

where γ_1, γ_2 are the activity coefficients for single and double charged ions, respectively. K_1 and K_2 are the first and second dissociation constants of sulphuric acid in water, K_{sp} is the solubility product for gypsum, and K_W is the dissociation constant of water. The activity coefficients γ_1, γ_2 were calculated using the Davies-Equation.

With the solutions of the differential equations one gets the electrolytic conductivity in good approximation with the aid of the Debye-Onsager equation also known as Kohlrausch's law:

$$\kappa = (C_{Ca^{2+}} + C_{SO_4^{2-}}) \cdot \left[\Lambda_0 - 0.041 \sqrt{C_{Ca^{2+}} + C_{SO_4^{2-}}} \right], \qquad (7)$$

where Λ_0 is the equivalent conductivity at infinitive dilution. The contributions of the other ions to conductivity are negligibly small. As well known, this law (7) considers the mobility reduction of the ions by relaxation and electrophoresis. The electrolytic conductivity is an integral parameter for dissolved, dissociated substances.

To solve the set of equations (3) and (6), computer programs have been written in FORTRAN. These codes were used to analyse the experiments.

4. Results and Discussion

Fig. 2 shows the time courses of the electrolytic conductivity calculated and measured in batch tests for one and three gram gypsum in 400 mL ultra pure water (κ~0.5 µS/cm). The experimental points were fitted by variation of the parameters $a_{gypsum} = F_{gypsum} / V_s \cdot q_{gypsum}$ and r in the solution of equation. The fits resulted in the following model parameters:
1 g gypsum, a_{gypsum} = 106 mmol/L/h, β = 0.67; 3 g gypsum, a_{gypsum} = 325 mmol/L/h, β = 0.67

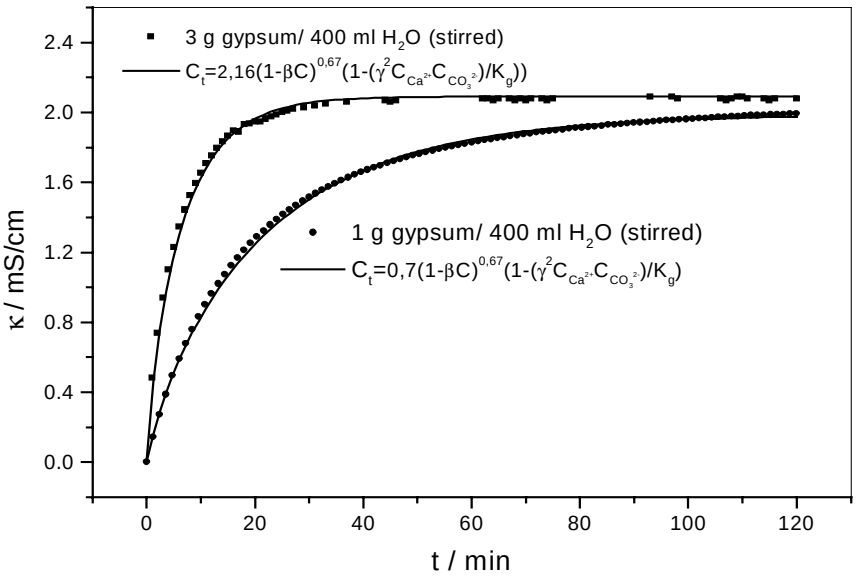

Fig. 2: Electrolytic conductivity κ of gypsum-water solution in dependence on time in batch experiments

There was no need to vary β for these fits. The calculation shows that a trebling of the mass also trebles the reactive surface. With the value $q_{gypsum} = 1.1 \cdot 10^{-4}$ mmol / cm^2 / s [2] which was determined by means of the rotating disk method one obtains the values 265 cm^2 / g for the reactive surface area per gram from the batch tests. These values are on the one hand, much smaller than 2000 cm^2 / g the value determined by BET measurement [6], however, on the other hand larger than the value of 101 cm^2 / g which follows from the sphere model. The BET method based on the adsorption of a monolayer of Kr-gas by the surface area .

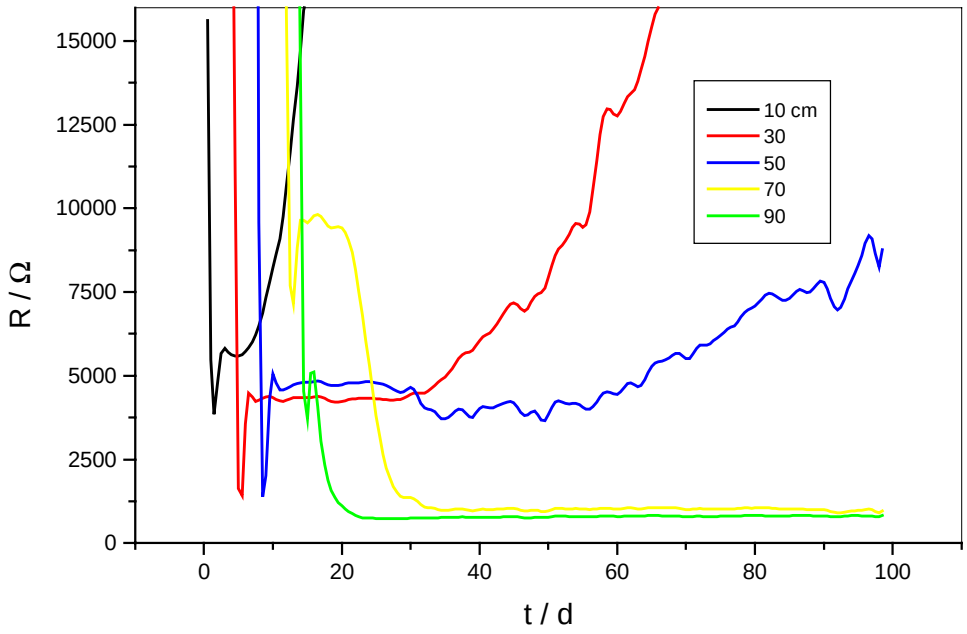

Fig. 3: The measured resistance distribution at the five measuring points of the 1m-column

Fig. 3 shows the results of the resistance measurements at the gypsum column. The steeply dropping curves, measured in the first 2-3 weeks, show the water movement from the beginning of the irrigation up to the steady state water profile. After approximately 22 days the

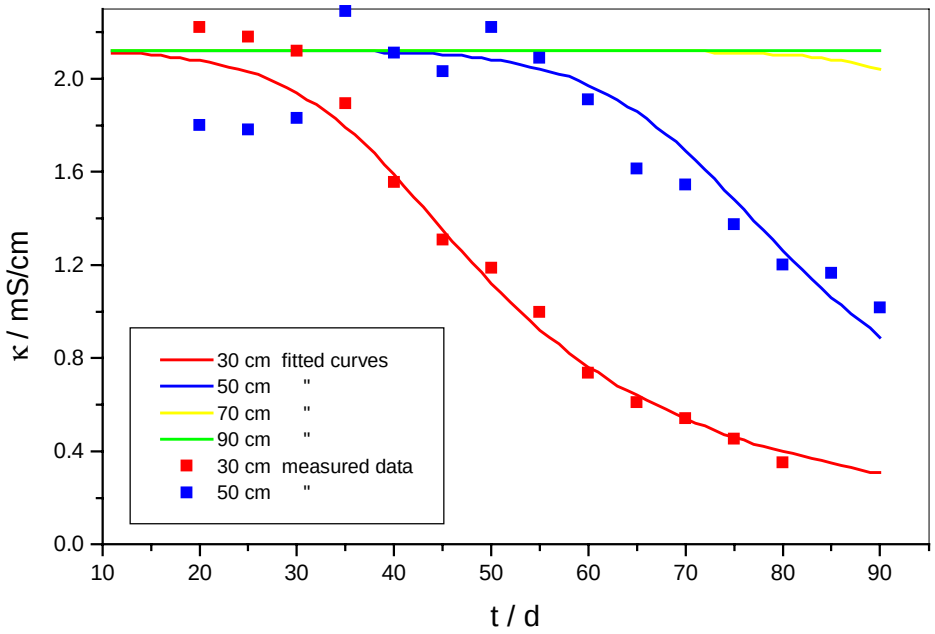

Fig. 4: Fits of the model solution of Equ. 3 to the experimental data

column is in stationary state. At this time the modelling by means of the transport equation system begins. The curves parallel to the t-axis mean that the transport process is in a local equilibrium, that is, the solution is saturated. The different resistance values in this area are determined by the water saturation. The first measured value at the 10 cm mark could not be

analysed since the gypsum was already exhausted during the adjustment of the equilibrium. The steep upward curve illustrates this fact.

By means of modelling the ionic conductivity of the solvent was calculated. The term "ionic conductivity" will be used for the specific ionic conductivity κ of the water extracted from the soil matrix. Therefore, the measured resistivity profiles must be converted into the ionic conductivity for comparison. For that the dependence of the resistance in relation to the saturation and the cell constant of the parallel steel electrodes is needed [7]. From the experimental data, the relationship follows between κ and water saturation s for the used sea sand: $\kappa = \kappa_{solution} \cdot s^{1.22}$. The conductivity sensor consists of two stainless-steel electrodes which are specifically sized and spaced to provide a known "cell constant" [8]. A calibration procedure supplied the cell constant K_c = 0.121 cm^{-1} ($\kappa = K_c / R$) for the given range of operation R = 0.5-15 kΩ.

The rectangular points in Fig. 4 show the result of the conversion. The solid lines represent the solution of the PDEs (3) with the fitted model parameters to the measured values. In order to reach these best possible fits the additional variation of β was necessary. The parameters in the PDEs given by the column test are: v = $3.0 \cdot 10^{-4}$ m/h, α_L= 1 cm, n = 0.38 and $s(x) = 1.0 - 0.75 / (1 + \exp(22.7(x - 0.64))$ for the fit of the saturation distribution. The result of the variation is: a_{gypsum} = 0.3 mmol/L/h and β = 1.9. That is, only the very small part of the reactive surface area of 8 cm^2 / g in comparison to the batch value of 266 cm^2 /g becomes effective in the unsaturated zone.

The large β value proves the assumption that the surface decreases more strongly with the mass than the geometrical relation between surface and volume or mass resulting in β = 2/3. Thus, one gram gypsum in one litre water dissolves 33 times faster than one gram gypsum in the seepage water from one litre, which flows with the Darcy-velocity of v = $3.0 \cdot 10^{-4}$ m/h at a saturation of $s \approx 0.25$.

5. Conclusions

Batch and column experiments were carried out to study the dissolution of gypsum by water under saturated and unsaturated conditions. The experimental results were analysed with the help of corresponding calculations.

The electrolytic conductivities and pH-values measured at equilibrium of the batch tests were in good agreement with the numeric results. The comparison of observed and modelled kinetics allowed to determine the reactive surface of the gypsum grains which were used in column tests too. The solution leaking from the 1 m-column turned out to be saturated with gypsum. Its conductivity and the calcium and sulphate concentrations well agree with the values measured in batch tests.

The analysis of the column experiments by means of calculations showed that only a small portion of the grain surface is chemically acting in the unsaturated zone. This reacting part of the surface turned out to depend on the saturation and on the Darcy-velocity. The calculation also showed that the dissolution of gypsum is mainly determined by the Darcy-velocity. The reason of this fact is the high dissolution rate of gypsum in water which leads to a fast saturation of the solution.

References

[1] R. Kuechler, K. Noack and T. Zorn (2001), Investigation of calcite dissolution under saturated and unsaturated water conditions, Rossendorf, Report FZR-316

[2] A. A. Jeschke, K. Vosbeck and W. Dreybrodt (2001), Surface controlled dissolution rates of gypsum in aqueous solutions exhibit nonlinear dissolution kinetics, Geochimica et Cosmochimica Acta, 65, 27

[3] L. Luckner and W. M. Schestakow (1991), Migration Processes in the Soil and Groundwater Zone, Leipzig, Verlag für Grundstoffindustrie

[4] P. C. Lichtner (1996), Continuum Formulation of Multicomponent – Multiphase Reactive Transport, in P. C. Lichtner, C. I. Steefel and E. H. Oelkers (Eds.), Reactive Transport in porous Media, Reviews in Mineralogy, Vol. 34

[5] W. P. Inskeep and P. R. Bloom (1985), An evaluation of rate equation for calcite precipitation kinetics at pCO2 less then 0.01 atm and pH greater than 8, Geochim Cosmochim Acta 49, pp. 2165-2180

[6] A. W. Adamson (1982), Physical chemistry of Surfaces, New York , Wiley & Sons

[7] M. A. Hilhorst (1998), Dielectric characterisation of soil, Wageningen Agriculture University

[8] C. H. Haman and W. Vielstich (1984), Elektrochemie I, Weinheim, VCH Verlagsgesellschaft

Acknowledgement

This work was made with the kind support of the Institute of Radiochemistry of Forschungszentrum Rossendorf.

DESIGN STUDIES OF A LIQUID LEAD NEUTRON RADIATOR FOR TOF EXPERIMENTS AT ELBE

Eberhard Altstadt, Sven Eckert, Hartwig Freiesleben[1], Vladimir Galindo, Eckart Grosse[2], Baerbel Naumann[2], Klaus Seidel[1], Frank-Peter Weiss

1. Radiator Design

Time of flight experiments with a pulsed neutron beam are planned at ELBE. The development of a technologically feasible radiator is an essential part of the preparation of such neutron experiments. Simulations were carried out for rotational symmetric radiators (length 4.1 mm; radii 2.5 mm and 5 mm) which consist of a solid material (Ta) [1]. For a beam energy range from 20 MeV up to 50 MeV and a current of about 1 mA the energy deposition in the radiator would result in melting. Based on this fact, a new radiator concept was developed using liquid lead as a radiator. The material depth seen by the electron beam was chosen in the order of the radiation length X_0 (Pb; X_0 = 6.3688 g/cm^2). Various materials for the lead confinement were considered.

2. Simulation of the power dissipation

The power dissipation in the wall and the lead were obtained for an electron beam of E = 30 MeV, I = 1 mA and r = 1.5 mm. The Monte Carlo simulations were carried out using the FLUKA code [2]. The results are given in Tab.1 for liquid lead (ϱ = 10.5 g/cm^3) and structural parts of the wall consisting of stainless steel or beryllium.

Table 1: Power dissipation in the lead and the wall given in kW (irradiation of the radiator with an electron beam of E = 30 MeV and I = 1 mA).

	material and thickness		
	steel	beryllium	
	500 µm	500 µm	300 µm
Pb	10.371 kW	10.271 kW	10.245 kW
wall (beam in)	0.571 kW	0.136 kW	0.081 kW
wall (beam out)	0.388 kW	0.092 kW	0.056 kW
lateral walls	0.256 kW	0.054 kW	0.031 kW
sum	11.586 kW	10.553 kW	10.413 kW

[1] Institute of Nuclear and Particle Physics, TU Dresden
[2] Institute of Nuclear and Hadron Physics

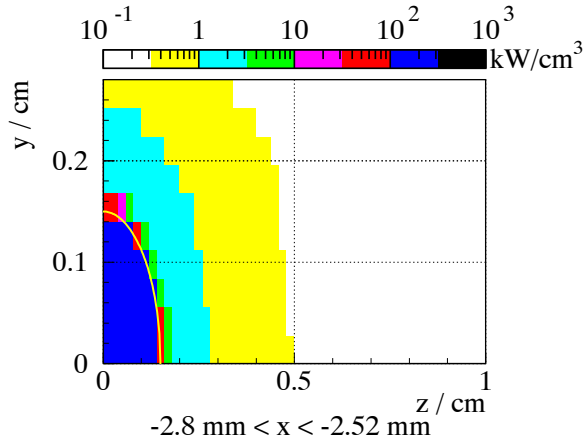

Fig. 1: Power density distribution in the liquid lead volume in the yz-plane normal to the beam in the first lead layer; the line describes the beam shape.

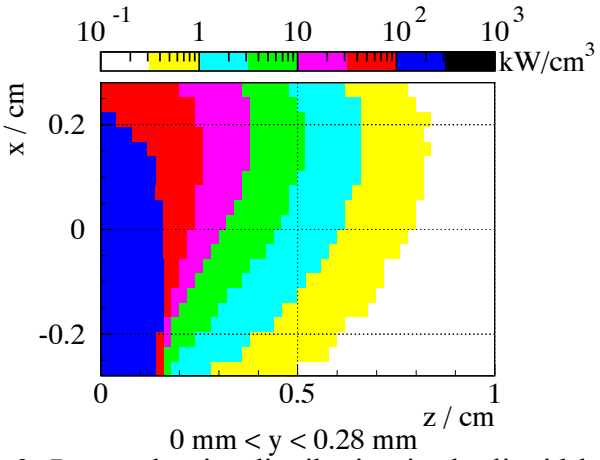

Fig. 2: Power density distribution in the liquid lead volume at the central xz-plane. Coordinate system see Fig. 5.

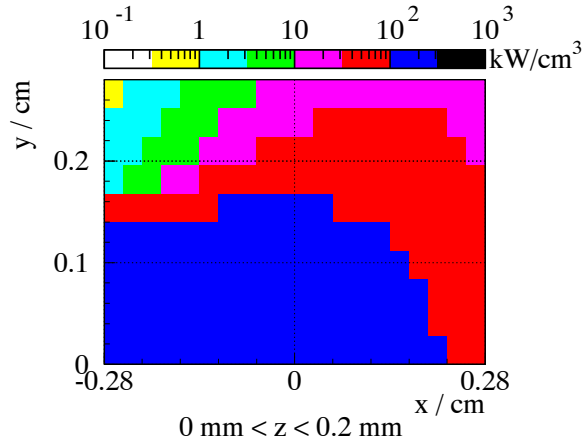

Fig. 3: Power density distribution in the liquid lead volume at the central xy-plane.

The power density in the steel wall heated by the electron beam amounts to 162 kW/cm^3, which is four times higher than in the 500 µm thick beryllium wall what leads to an overheating of the steel. Hence a beryllium confinement was considered. Moreover, the three-dimensional distribution of the power dissipation in the radiator was calculated.

In Fig.1 the power density distribution in the liquid lead volume is shown in the yz-plane. The beam hits the radiator at the Be wall at x = -0.33 cm. The power density distribution is also shown for the central regions in the xz-plane (Fig.2) and the xy-plane (Fig.3) respectively.

3. The liquid lead loop - Numerical flow and temperature simulation

The lead circulates inside a closed loop (Fig.4). The liquid metal is exposed to the electron beam when it passes the target section with a cross sectional area of 5.6 x 5.6 mm^2. The beryllium walls in the target section have a thickness of 500 µm.

A test loop will be set-up to validate the numerical calculations and to collect experience with respect to the behaviour of the materials as well as the handling and instrumentation of the loop. As shown in Fig.4 the main components of the loop are an induction pump, a heat exchanger, an expansion tank and a storage tank. The loop is designed to operate at a pressure up to 6 bars and a maximum flow rate of 0.2 l/s. The lead volume of the loop will be about 5 l.

Numerical calculations for the target section of 12 cm length predict maximum values of the temperature of 530 °C in the lead assuming a mean velocity of about 5 m/s and an inlet temperature of 400 °C. A mean temperature of 450 °C is obtained by averaging over the cross section at a distance of 6 cm downstream of the position where the electron beam hits the lead.

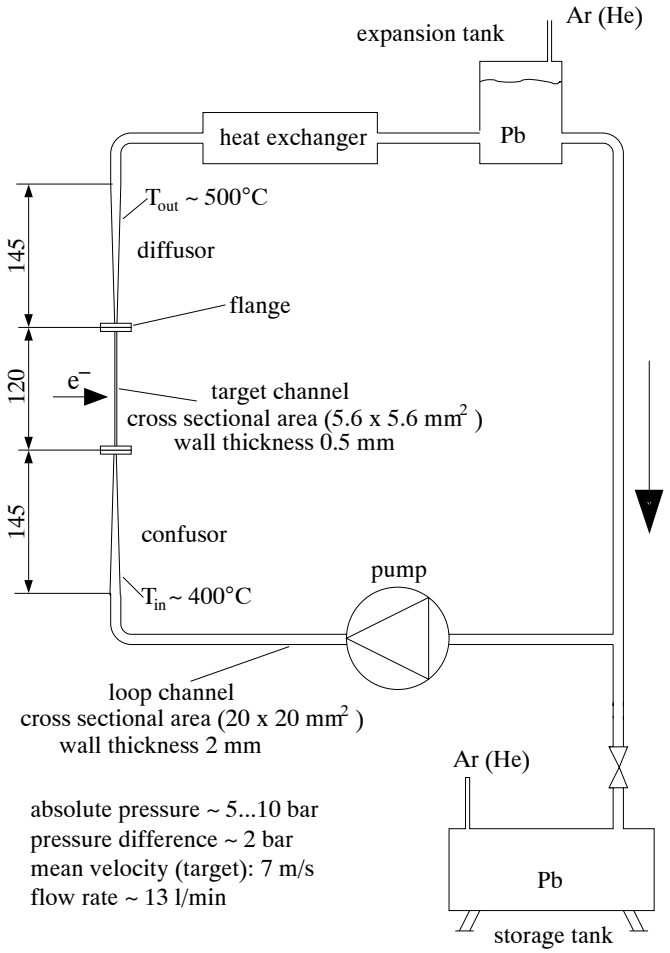

Fig. 4: Sketch of the Pb loop.

Fig. 5 shows the results of the numerical flow and heat transfer simulation using the commercial multi-purpose finite elements CFD code FIDAP [3]. It represents, from the left to the right, the discretisation mesh, the temperature distribution in the beryllium wall, the temperature distribution in both the wall and liquid lead, respectively. The flow is in z-direction.

The temperature field leads to mechanical loads in the wall of the square Be-channel. The stresses and strains are evaluated using a finite element model based on the code ANSYS [4]. The mesh of the Be-wall is identical to that of the CFD model. Thus the nodal temperatures can be taken from the FIDAP calculations.

Furthermore, for reason of conservatism a static internal pressure of 10 bars was assumed. The material was considered to behave elastic-plastically. Beryllium is rather brittle at room temperature (plastic fracture strain 2 %) whereas at higher temperatures (300-700 °C) it becomes more ductile (fracture strain up to 30 %). Fig. 6 shows the plastic strain for a Pb velocity of 5 m/s. The plastic deformation in the Be-wall is limited to the vicinity of the electron

beam. The maximum plastic equivalent strain is about 0.48 % occurring at the wall which is hit by the beam. This is far below the fracture strain even at room temperature. However, considering a large number of temperature cycles (heat-up, cool down), material fatigue could be a problem.

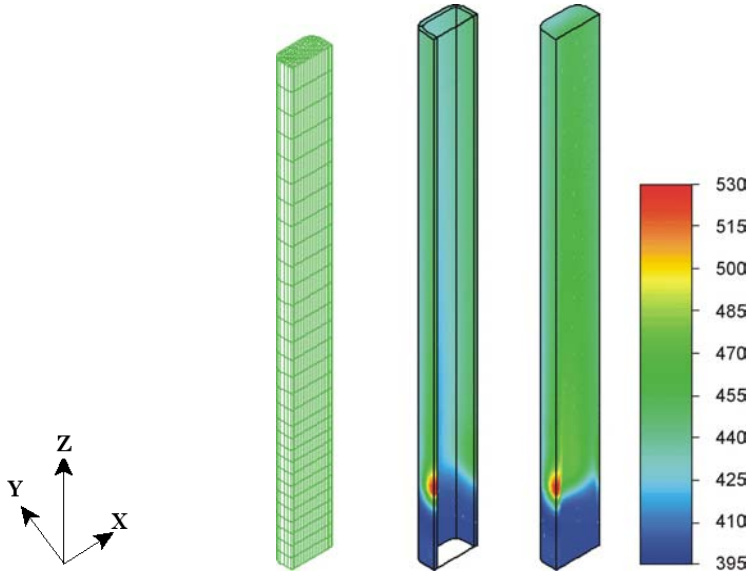

Fig. 5: Temperature distribution. Mean Pb velocity: 5 m/s . Maximum temperature: 530°C.

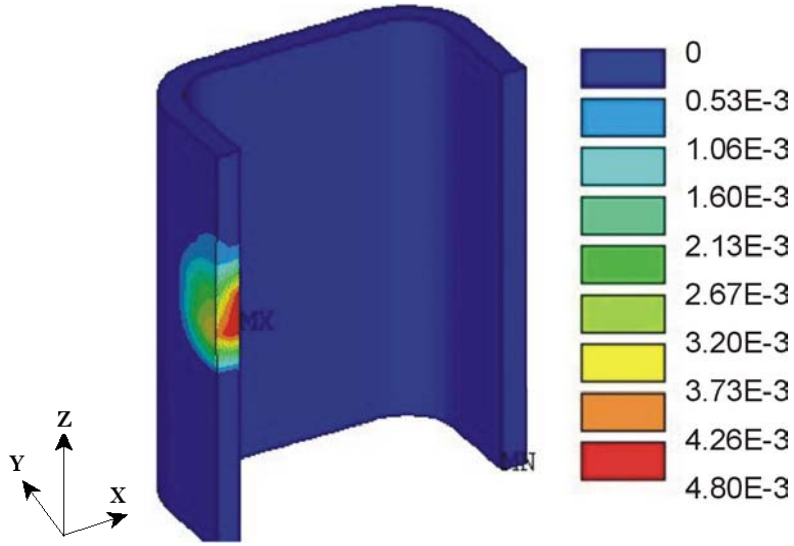

Fig. 6: Plastic equivalent strain in the beryllium wall.

References

[1] B. Naumann et al., FZ Rossendorf, Wiss.-Techn. Berichte FZR-271 (1999) 35
[2] A. Fasso, A. Ferrari and P.R. Sala, Proc. of the Monte Carlo 2000 Conference, Lisbon, 23-26 Oct., (2000)
[3] Fluent Inc.: FIDAP 8 theory manual, Lebanon, NH, USA (1998)
[4] ANSYS User's Manual for Rev. 5.6., Swansons Analysis Systems, Inc. (1999)

ON-LINE MONITORING SYSTEM FOR HETEROGENEOUS HYDROGENATION IN STIRRED TANK REACTORS

Günther Hessel, Jürgen Heidrich[1], Ralf Hilpert[1], Holger Kryk, Michael Roth[1], Wilfried Schmitt, Torsten Seiler and Frank-Peter Weiß

1. Introduction

The aim of this work was to develop an on-line monitoring system to support the operator of stirred tank reactors in the safe and ecologically compatible process control of transient semi-batch reactions. After having tested the monitoring system with a homogeneous esterification process [1], the catalytic hydrogenation of a substituted nitrobenzoate (SNBE) to a substituted aminobenzoate (SABE) in isopropanol using platinum on active carbon (Pt/C) as a catalyst was used as a further model reaction to test the performance of a prototype of the monitoring system. This hydrogenation chosen by the industrial partner is a heterogeneous (multi-phase), strongly exothermic process with consecutive reactions and with a concurrent reaction path. To model this complex chemical reaction, extensive studies were carried out using a reaction calorimeter (RC1) which was equipped with an immersion tube of a FTIR-spectrometer [2]. Depending on the SNBE quality, the process conditions and the effects of mass transfer, two pathways for the reduction of the nitro compound (SNBE) to the amine compound (SABE) are possible. If the concentrations of the intermediates nitroso and hydroxylamine increase, the much slower concurrent reaction path via the azo compound can occur. Due to the accumulation of the intermediates, the hazardous potential of the process is extremely increased because then strongly exothermic condensation reactions might take place without hydrogen uptake. Therefore, the most important task of the monitoring system should be to estimate the concentration profiles during the hydrogenation. To fulfil the requirements of the GMP (good manufacturing practice) in the pharmaceutical industry, the monitoring system (MoSys) was embedded in a batch information management system (BIMS) developed by Degussa AG. In this paper, the working principle of MoSys and BIMS is described. Furthermore, results from the verification of MoSys in the laboratory reactor and from on-line testing in a chemical plant of the Degussa AG are presented.

2. Description of MoSys and BIMS

In order to realise the real-time operation, the monitoring system was integrated into the new batch information management system to be connected with the process control system (PCS) of the chemical plant. Figure 1 shows the structure and the information flow between the involved systems. As can be seen in Fig. 1, the functionality of MoSys was distributed to three modules: MoSys-Config, MoSys-Adapt and MoSys-Online. MoSys-Config links the monitoring system to the BIMS database and allocates it to the production plant to be monitored.

In MoSys-Adapt, the coupled mass and heat balances with adaptive model components are used for the adaptation of the monitoring system to the target chemical plant [1]. The application of adaptive components requires that Mosys has first to be trained with at least one set of data from a complete batch process under normal conditions.

[1] Degussa AG

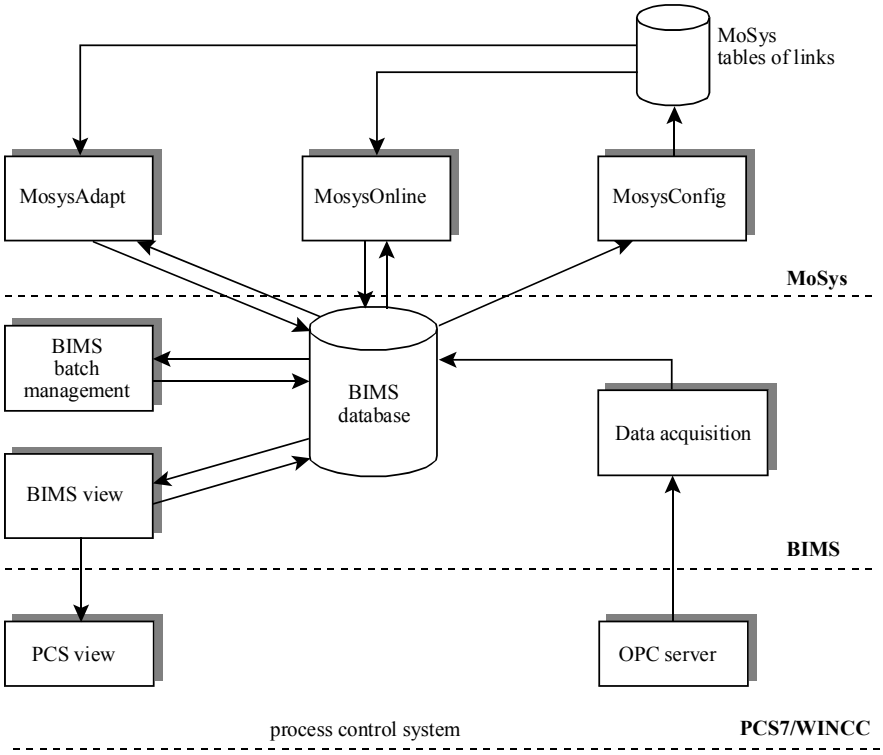

Fig. 1: Block diagram of the integration of MoSys into BIMS

In case of the heterogeneous exothermic hydrogenation process, the time dependent differences between the thermal conversion and the chemical conversion are used to characterise the current process state defined by the concentration distribution of the educt, the intermediates and the product. Results of these adaptations are stored to the BIMS database from where they are available as parameters for the balance models in the third program module MoSys-Online. At the beginning of a hydrogenation, the program module MoSys is initialised. The results from MoSys-Online are promptly stored in the BIMS database so that they are then available for visualisation in the framework of BIMS.

The objectives of BIMS are to use all information on the current process state obtained by MoSys (e. g. estimated profiles of concentrations) and to give a recommendation to the operator by visual displays if a deviation from the normal process course was recognised by MoSys. In Fig. 2, the scheme of the data & information flow in the batch information management system is depicted. BIMS consists of the components: monitoring system MoSys, data management system (SQL database) and visualisation & operation. These user programs are implemented on a separate PC coupled to the terminal bus. The graphical user interface (GUI) for the operators is additionally installed on several operator stations so that the information is available both in the measuring station and on the different control panels in the chemical plant. These operator stations are used, for example:

- to enter the MoSys coefficients and plant parameters by the system tutor,
- to input the batch data (recipe) and laboratory findings (chemical analysis of educts and products) by the process officer,
- to enter data of events and of countermeasures during a deviation from the normal process course by the operator and
- to visualise process signals and MoSys output signals.

An automatic intervention of the BIMS in the process control is not scheduled at present. Corrective measures and interventions in the process course are exclusively initiated by the operator. For this purpose, the operator gets corresponding hints for countermeasures from the knowledge base of known process situations. This knowledge base is generated from historic events and corresponding actions of the operator.

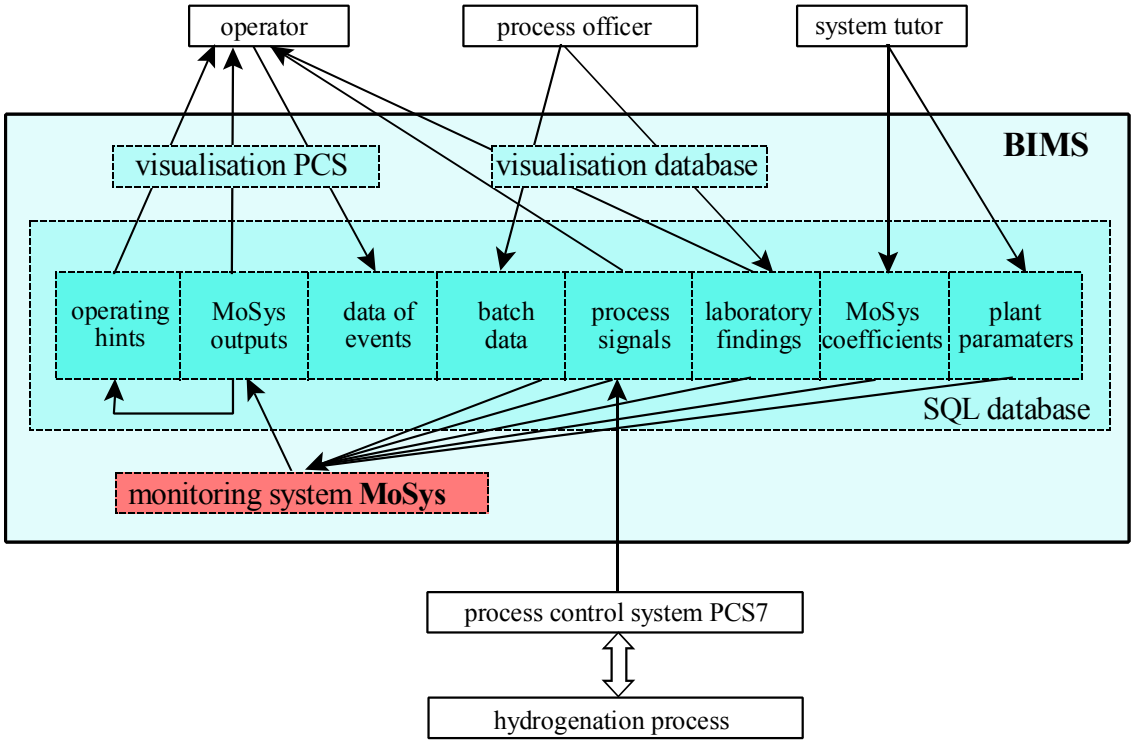

Fig. 2: Scheme of the data & information flow

3. Results of tests

To test and optimise the monitoring system, numerous experiments were carried out in the automatic laboratory reactor (ALR), equipped with a 1 or 10 litre reactor vessel. For the validation of the estimated MoSys-concentration profiles, a set of samples was taken from the reaction mixture during the hydrogenation processes and analysed using high performance liquid chromatography (HPLC). After this validation, the monitoring system was embedded into the BIMS and tested on-line using hydrogenation batches performed in the chemical plant.

3.1 Verification at laboratory scale

To optimise the monitoring system for heterogeneous hydrogenation processes, the following investigations were carried out in the ALR:

- hydrogenation reactions of different educt charges under production conditions for
  - validation of the estimated MoSys-concentration profiles
  - comparison of the estimated concentration profiles obtained at laboratory and industrial scale

- hydrogenation reactions under isothermal and isobaric conditions with different catalyst concentrations, stirrer speeds and reactor pressures for
  - testing the stability of the monitoring system under alternating process conditions (e.g. faulty states)
  - examination of the concentration profiles during different process conditions (e.g. catalyst concentration) and comparison with results obtained by calorimetric investigations including in situ FTIR-measurements

As examples of these studies, the MoSys-concentration profiles during the hydrogenation processes of two different educt charges of the nitroaromatic compound (A and B) are shown in Fig. 3.

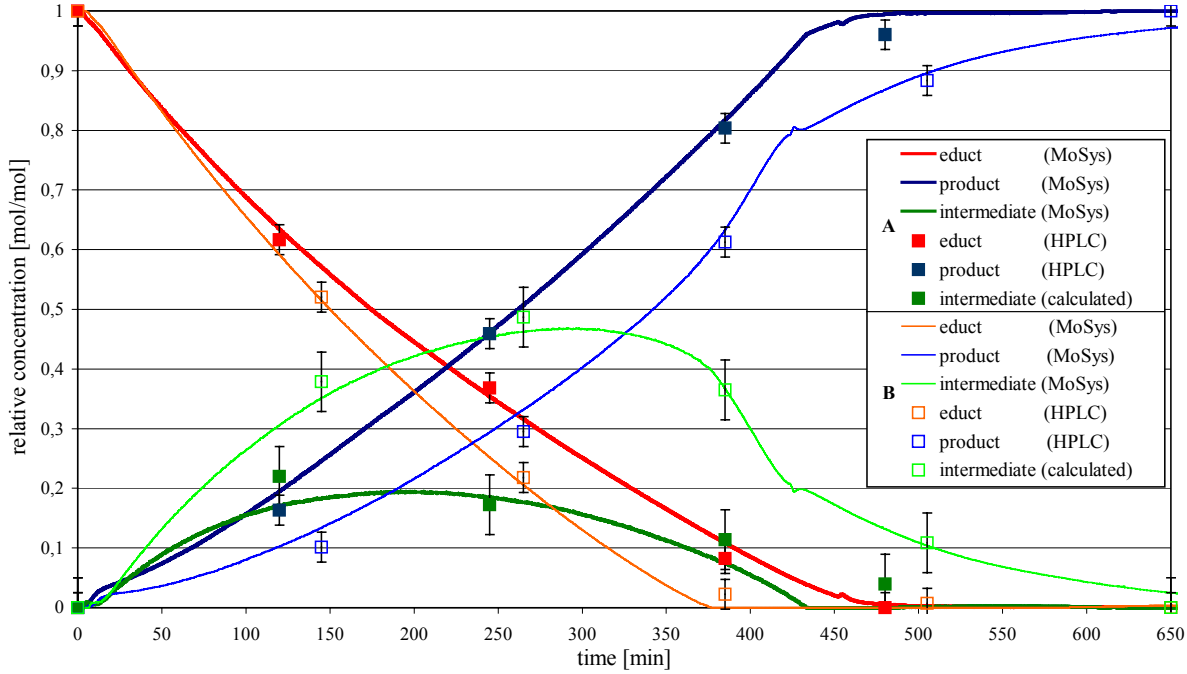

Fig. 3: Concentration profiles of MoSys output signals and HPLC results during the hydrogenations of the educt charges A and B in the ALR

There is a good agreement of the MoSys output signals with the concentration data obtained by HPLC analyses for the educt and the product. Due to the instability of the intermediates, it was not possible to quantify the HPLC signals for these substances. Therefore, the concentration data of the intermediate were calculated from a mass balance based on the HPLC data of the educt and the product. The higher amount of accumulated intermediate during the hydrogenation process in case of charge B was confirmed by additional calorimetric investigations.

3.2 Tests in the production plant

The performance of MoSys and BIMS was tested in a multipurpose tank reactor during a production campaign of 15 hydrogenation batches. By using these PC-based systems, all quality-relevant process data were recorded and archived during the whole hydrogenation run. Additionally, the operator chronologically listed important events like operator interventions. Thus, MoSys was able to estimate the most important parameters of chemical reactions, the concentrations of the substances, as shown in Fig. 4. This figure provides the MoSys-

concentration profiles during the hydrogenation batches for the educt charges A and B in the production plant. The MoSys results during the hydrogenation process at the industrial scale correlate with the estimated concentration profiles at the laboratory scale according to Fig. 3. The higher amount of accumulated intermediate during the hydrogenation process in case of charge B is recognised correctly.

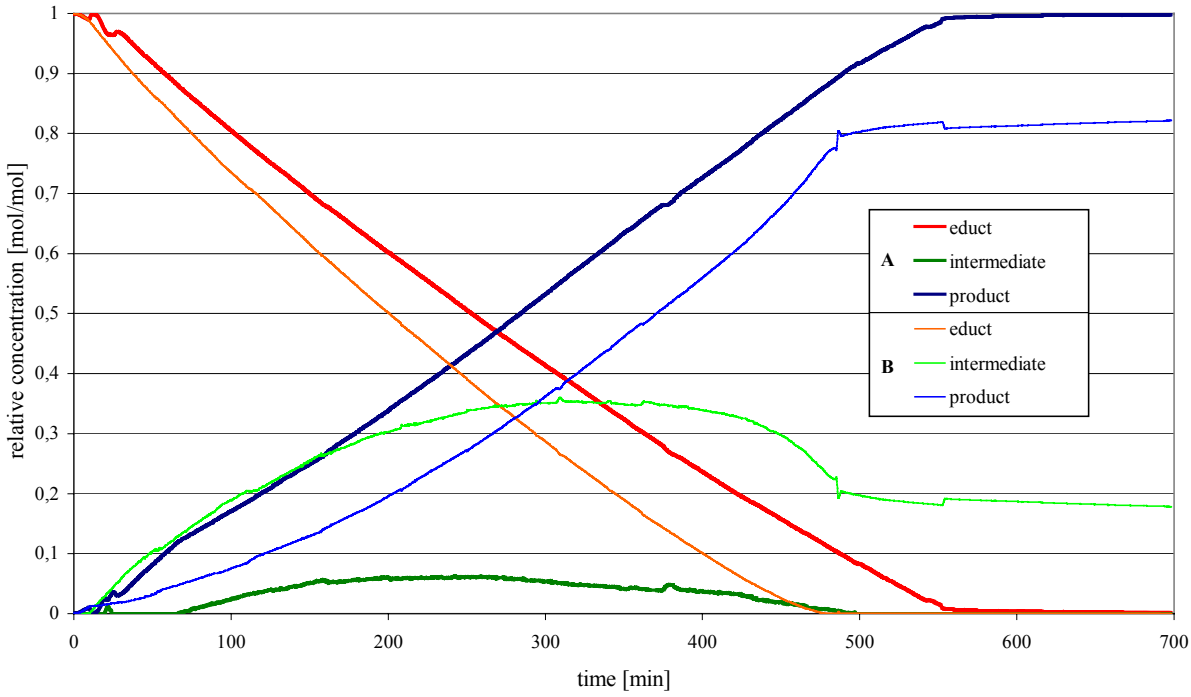

Fig. 4: MoSys-concentration profiles during the hydrogenations of the charges A and B in the production plant

Furthermore, information on the chemical conversion rate and the remaining hydrogenation period up to the complete hydrogenation were indicated in graphical form at the operator stations (Fig. 5).

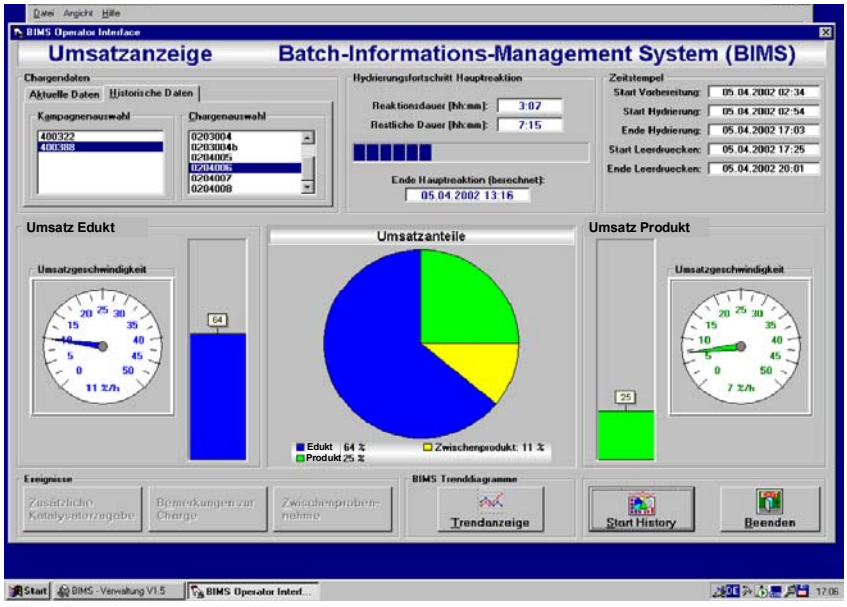

Fig. 5: On-line display of the conversion rates and the remaining hydrogenation period at the operator stations

4. Conclusions

The on-line monitoring system MoSys for complex hydrogenation processes has been developed to support the operator in decision making. To test the prototype in a chemical plant, MoSys was embedded in a newly developed batch information management system . Both software program systems were implemented on a separate PC coupled to the process control system. The balance models used in MoSys were adapted to the industrial chemical plant using data sets from normal productions batches. After the adaptation , the concentration profiles which were indicated by MoSys showed a qualitatively good agreement with the expected concentration profiles. Besides the on-line concentration profiles of the educt, intermediate and product, MoSys provided information on the conversion rate and the remaining period up to the complete hydrogenation. Moreover, qualitative varieties between the different hydrogenation batches regarding to the intermediate accumulation and the hydrogenation time would be visualised by MoSys on-line.

By using MoSys and BIMS, the demand for traceability of the complex batch processes could be fulfilled. The recorded data enables to optimise the production process so that the required product quality is attained. Furthermore, the archived data allow to repeat hydrogenation batches of a high quality at any time. Consequently, MoSys and BIMS contribute to fulfil the requirements of the good manufacturing practice in the pharmaceutical industry.

Further work is planned to validate the quantitative concentration of the intermediate by sampling of in-process material during the running production process and by analysing these samples by means of HPLC. For this purpose, a special sampling device has to be installed for the next production campaign so that samples can be taken under hydrogen atmosphere.

References

[1] G. Hessel, H. Kryk, W. Schmitt, T. Seiler and F. P. Weiss (2001), Monitoring system for batch reactors using adaptive heat balances, in F. P. Weiss, U. Rindelhardt (Eds.): Annual Report 2000 Institute of Safety Research, Rossendorf, Report FZR-316, April 2001, pp.77-82

[2] K. Biskup, B. Bothe, G. Hessel, G. Hulzer, H. Kryk, W. Schmitt and N. Tefera (1999), Characterizing the kinetics of heterogeneous exothermic reactions, in F. P. Weiss, U. Rindelhardt (Eds.): Annual Report 1998 Institute of Safety Research, Rossendorf, Report FZR-268, July 1998, pp. 71-80

Acknowledgements

The project this paper is based on is funded by the BMBF (Bundesministerium für Bildung und Forschung) and is registered with No. 01RV9802/4.

MAGNETIC FIELD INFLUENCE ON ELECTROCHEMICAL PROCESSES

Tom Weier, Jürgen Hüller and Gunter Gerbeth

1. Introduction

Electrochemical reactions play an important role in various types of industrial processes including electrolysis (conversion of substances), metal processing and finishing, batteries and fuel cells, and waste water treatment. From an industrial viewpoint, primary considerations are obviously of economic nature. The product yield in space and time and the specific energy consumption are of utmost importance for the return of investments.
Magnetic fields might be a tool to increase the space time yield as well as to decrease the energy consumption of specific electrochemical processes. The effect of magnetic fields on electrochemical reactions were so far mainly attributed to an enhanced mass transfer due to electromagnetically induced convection [1]. A possible effect of the magnetic field on reaction kinetics has been argued by several researchers, too. Recently, the latter point of view started to gain acceptance due to a number of newly published results, but remains still controversial. In the present paper, the convective effect of the Lorentz force is the sole object of consideration.

2. Increase of space time yield

The space time yield ρ_P [kg m^{-3} s^{-1}] of product P in the absence of competing reactions may be defined as

$$\rho_P = a_e j \frac{M_P}{\nu_e F}. \tag{1}$$

Here, a_e denotes the electrode area per volume, j the current density, M_P the molar mass of the product, ν_e the number of electrons involved in one reaction and F the Faraday constant, respectively. The variables of equ. (1) accessible to the chemical engineer are a_e and j. Both should be maximised in order to increase ρ_P.
Electrochemical reactions belong to heterogeneous chemical processes. Therefore various transport phenomena have to be taken into account. If the mass transport to or from the electrodes determines the reaction rate, the maximum current density is as well limited by mass transfer. Typical industrial processes under mass transfer control are for instance copper refining and many electroorganic synthesis, like the Monsanto process.
The maximum current density attainable under mass transport control is the limiting current density j_l. It may be related to the diffusion coefficient D of the reacting specie, its concentration c in the bulk of the cell and the thickness of the Nernst diffusion layer δ_N around the electrode by [2]

$$j_l = \nu_e F D \frac{c}{\delta_N}. \tag{2}$$

The thickness of the diffusion layer again is determined by the flow conditions near the electrode. This is where Magnetohydrodynamics (MHD) comes into play.

The Lorentz force

$$\mathbf{F} = \mathbf{j} \times \mathbf{B} \tag{3}$$

is the vector product of a current density **j** and a magnetic field **B**. This Lorentz force represents a body force inside the electrolyte able to influence its flow. Since the current density is an inherent feature of electrochemical processes, only a suitable magnetic field has to be added to generate a Lorentz force. In economic terms, no running costs are added to the process, provided the magnetic field originates from permanent magnets.

Fig. 1 shows the anodic limiting current density in a small cell with vertical electrodes for the classical $K_4[Fe(CN)_6]$/ $K_3[Fe(CN)_6]$-redox system under different conditions in terms of the magnetic field influence. A permanent magnet has been placed behind the anode of the cell in such a way, that the main field component was parallel to the electrode surface. By changing the orientation of the permanent magnet Lorentz forces either in upward or downward direction could be imposed on the electrolyte. At the anode $[Fe(CN)_6]^{4-}$ is oxidised to $[Fe(CN)_6]^{3-}$, which has a smaller density than the former complex. Therefore in the unforced case, a natural convection develops, which is directed upwards at the anode and downwards at the cathode. If a steady state is reached, a limiting current given by this natural convection is established. The limiting current increases with the concentration as it would be expected from equ. (2), although this simplified relation hides the nonlinearities caused by the flow in

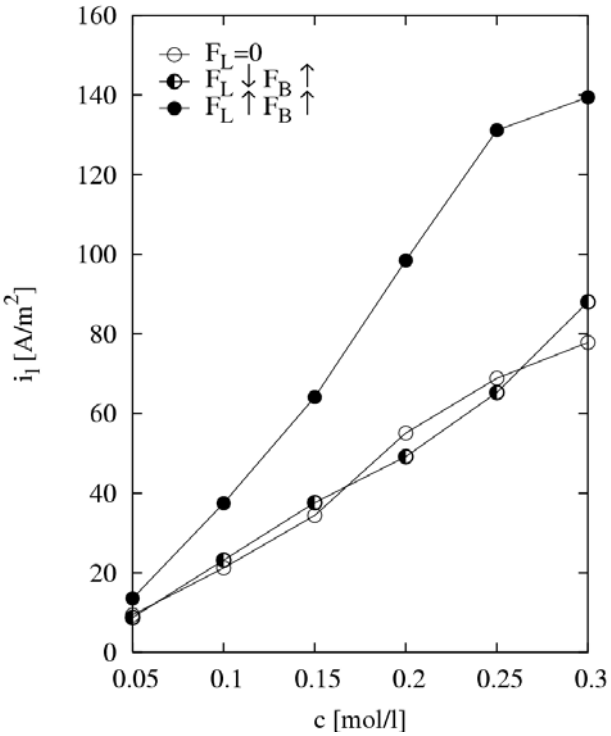

Fig. 1: Limiting current density versus concentration for a permanent magnet behind the working electrode.

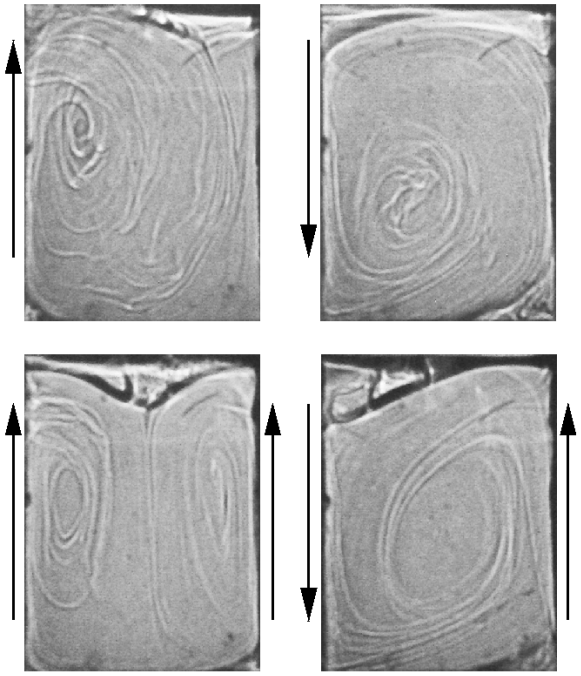

Fig 2: Shadowgraph pictures of the electrolyte flow under several magnetic field configurations. The arrows denote the direction of the Lorentz force near the electrodes.

δ_N. In Fig. 2 four shadowgraphs of the electrolytic solution in the cell are given. The arrows denote the direction of the Lorentz forces near the electrode. Both images in the upper part of Fig. 2 show configurations, where only the anode is equipped with a permanent magnet. It is

clearly to be seen that the Lorentz force despite their concentration in a small volume along the anode determines the flow in the whole cell completely. If one applies additional magnets behind the cathode, depending on the orientation of the force fields a twin vortex structure may be generated, or the single large vortex typical for the one side forcing might be intensified. Dictated by the cell geometry, in all configurations edge vortices are present.
If the Lorentz force F_L has the same direction as the buoyancy force F_B, the limiting current density in Fig. 1 is increased by a factor of almost two over the whole range of concentrations. In the contrary, the configuration where the Lorentz force counteracts buoyancy shows only a slight increase and sometimes even a decrease of the limiting current density. Reduced convection alone could hardly explain this since, as can be deduced from the upper left subfigure of Fig. 2 and has been measured by Particle Image Velocimetry, the velocity magnitudes are similar in both cases. A possible explanation might be the formation of dead zones, when both forces are antiparallel. As mentioned afore, the anodic product is lighter than the bulk solution, therefore it will tend to accumulate in the upper left edge vortex thus preventing the covered electrode area from taking part in the reaction. Therefore the measured absolute current and the mean current density calculated with the geometric electrode area would be decreased.

3. Decrease of the specific energy consumption

Many industrial electrochemical processes such as chloralkali or water electrolysis take place under activation control, i.e. the rate determining step is not connected to mass transport in the electrolyte but to the processes of adsorption/desorption, surface diffusion and electron transfer. The cell voltage U_C which has to be applied at the electrodes in order to maintain an electrochemical reaction can be divided into several components

$$U_C = U_0 + \eta_a + \eta_c + I \sum R. \tag{4}$$

Here U_0 denotes the purely thermodynamicaly determined reversible cell voltage, η_a is the anodic and η_c the cathodic overvoltage, respectively. $I\Sigma R$ describes the voltage drop due to the several resistances in the cell (electrolyte resistance, membrane resistance). Whereas neither the reversible cell voltage nor the overvoltages could be influenced by fluid dynamic means, the resistance of the electrolyte might be accessible in the case of processes developing gaseous products. The gas holdup in the cell increases the averaged electrolyte resistance and can lead to other unfavorable side effects like foaming and membrane degradation [3].
As has been shown in [4] the fluid velocity near the electrodes has a strong influence on the electrode area covered with gas bubbles which is, therefore, blocked for the current. Depending on the fluid velocity almost all bubbles can be removed from the electrode, reducing the Ohmic resistance accordingly.
As has been already demonstrated, the magnetic fields of suitable placed permanent magnets are capable of producing a Lorentz force density accelerating the electrolyte near the electrode. Fig. 3 shows Laser Doppler Anemometry measurements near the gill of a model louver. In this case louver and counter electrode have been immersed in a

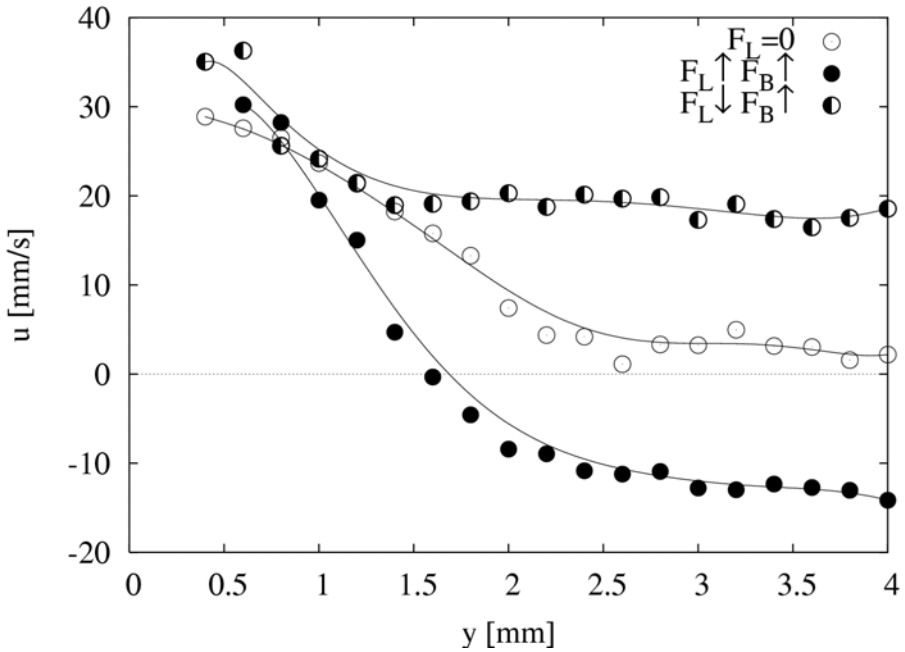

Fig. 3: Mean velocity profiles near the louver gill under different Lorentz force configurations.

larger vessel containing a 0.2 molar NaOH. The reaction has therefore been a water electrolysis. Only one gill of the anode was equipped with permanent magnets, the velocity measurements took place in the plane in front of this gill. *y* denotes the wall distance and *u* the mean velocity. In the case without Lorentz force a wall jet can be seen that is driven by the rising oxygen bubbles evolving at the anode. The velocity is positive in the y range covered in the diagram. In the direct vicinity of the anode, velocity measurements have been prevented by the high void fraction, which caused an intensive light scattering. If the Lorentz force points upwards, the mean velocity gradient becomes steeper near the electrode. For $y \geq 1.5$mm a back flow occurs. In the case that Lorentz force and buoyancy are opposed, the velocity farther away from the wall increases compared to the unforced case. At first sight, this seems paradoxical. A possible explanation could be the redistribution of oxygen bubbles due to the downward force: the bubbles migrate from the region near the electrode into the outer fluid and accelerate it due to buoyancy.
So far complementary measurements of the cell voltage are still to be performed. Therefore the presumed effect on the energy consumption has not been verified, but could be concluded from the pertinent literature.

4. Conclusions

Magnetic fields in conjunction with present electric fields may be used to influence significantly the momentum transfer in electrochemical cells and reactors. The effects shown here demonstrate the large influence of magnetic fields of moderate strength and extension on mass transfer and flow conditions in the cells.

References

[1] Fahidy, T. Z. (1999), The effect of magnetic fields on electrochemical processes, in: B.E . Conway (Ed.): Modern Aspects of Electrochemistry, Nr. 32 (pp.333-354), New York, Kluwer/Plenum

[2] E. Heitz, G. Kreysa (1986), Principles of Electrochemical Engineering, Weinheim, VCH

[3] C. Schneider (1997), Fluid Mechanics of Electrolytic Cells, in F.P. Weiß, U. Rindelhardt (Eds.): Annual Report 1997 Institute of Safety Research, Rossendorf, Report FZR-238

[4] C. W. M. P. Sillen (1983), The effect of gas bubble evolution on the energy efficiency in water-electrolysis, PhD thesis, Tech. Hogeschool Eindhoven

Acknowledgements

We are very grateful to Alexander Grahn for the possibility to use his shadograph and video equipment.

INFLUENCE OF A ROTATING MAGNETIC FIELD ON THE CRYSTAL GROWTH OF GaAs

Olaf Pätzold[1], Ilmars Grants, Ulrike Wunderwald[1], and Gunter Gerbeth

1. Introduction

The GaAs wafer market is characterised by an increasing demand on high-quality substrates ready for epitax[1]ial post-processing. Nowadays, advanced Vertical Bridgman (VB) growth variants such as the Vertical Gradient Freeze (VGF) technique, are preferentially employed to meet the strong requirements according to a low dislocation density and high homogeneity of the substrates. By combining the VGF method with a rotating magnetic field (RMF) for a defined influence on the melt flow, a further improvement of the crystal quality seems to be possible. The benefit of the RMF may result from the stationary azimuthal and meridional flow imposed to the melt under certain conditions. Hence, it can be regarded as an additional tool to control the heat and dopant transport during the growth in a predefined way.

The RMF induced melt flow in a VB/VGF set-up has been studied by numerous authors, but up to now these results have only been confirmed experimentally by the directional solidification of model substances like gallium doped germanium or various tin alloys. Here we report on first results on the VGF-RMF growth of GaAs. The main purpose is to demonstrate the feasibility of a predictable and reproducible control of the heat flow in the melt by the rotating field resulting in a well-defined influence on the geometry of the solid-liquid phase boundary. For more details of these investigations we refer to [1].

2. The growth process

The scheme of the VGF-RMF set-up used for the growth of GaAs crystals at TU Bergakademie Freiberg is shown in Fig. 1. The growth furnace was especially designed for the vapour-pressure controlled VGF technique in a closed ampoule under optimised thermal conditions. The furnace is characterised by a modular, axis-symmetric set-up of seven heating zones. The maximum temperature is at about 1300°C and crystals with a diameter up to 2 inch can be grown. A separate seed heater guarantees a definite adjustment of the seeding point and by the top heating zone the temperature in the upper part of the furnace can be stabilised. The temperature control consists of a central computer system with implemented software controllers, DC power actuators for each heating zone and a set of type B thermocouples which are arranged at the inner surface of the ceramic heater supports. To suppress electronic disturbances induced by the rotating field the thermocouples are equipped with second order low-pass filters of Bessel type. The remaining fluctuations of the outer temperatures during RMF action are below 0.5K. The applied RMF (pole order = 1) is generated by a three-phase current controlled, 120° set-up of three coil pairs. Induction and frequency of the field can be varied in the ranges of 0 – 10mT and 30 – 400Hz, respectively. The direction of rotation can be switched. In order to get an estimate about the screening of the rotating magnetic field due to the metallic parts of the growth chamber, pre-experiments with and without the chamber have been performed with a stainless steel cylinder hanging on a torsion wire. They resulted in a screening factor $B_{eff}/B_0 = 0.7 \pm 0.01$.

[1] TU Bergakademie Freiberg, Institut für NE-Metallurgie und Reinststoffe

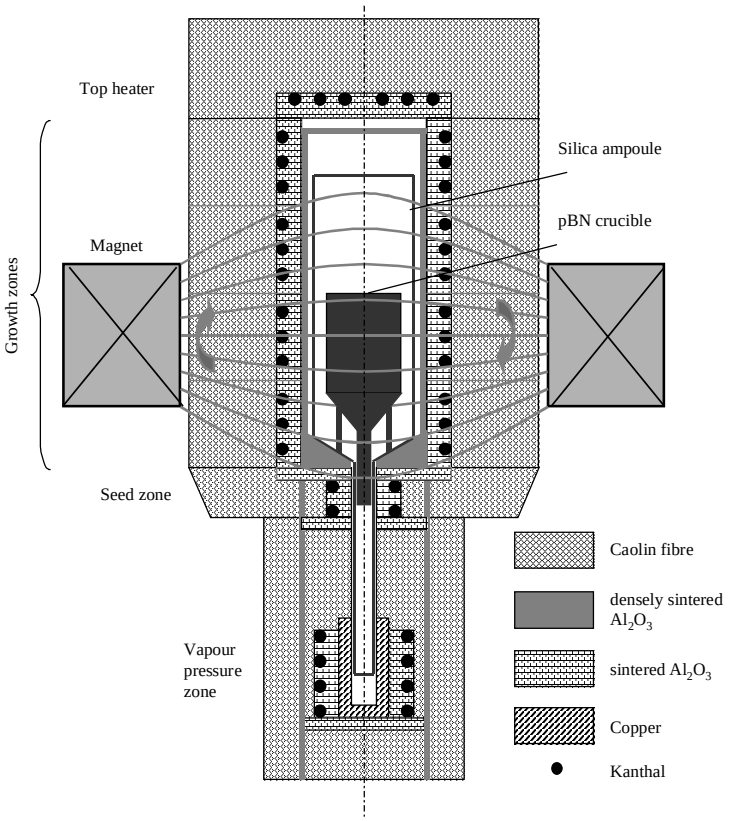

Fig. 1: Scheme of the VGF-RMF facility

The experiments were aimed at the detection of the RMF influence on the solid-liquid phase boundary. Si doped GaAs crystals with a diameter of two inch were grown in ⟨100⟩ direction under identical thermal conditions. The Si concentrations in the melt were about $1 \cdot 10^{19} cm^{-3}$. For the detection of the interface {110}-oriented samples have been prepared by sectioning the crystals lengthwisely. Striations were revealed by means of photoetching in a H_2O:HF:CrO_3 solution.
In doped material the interface is marked by so-called dopant striations due to microsegregation, i.e. fluctuations of the growth velocity. The striations at different stages of the growth were artificially induced by abrupt changes of the RMF itself. A shortly applied (~ 5min) RMF is used just to mark the natural striations, whereas RMF affected interfaces required an application of the filed over periods of more than one hour. With a typical growth velocity of 2 mm/h the overall growth process takes about 1-2 days.

3. Theoretical considerations

Before studying the melt convection and its influence on the solid-liquid phase boundary, the temperature boundary conditions for the melt have to be extracted out of a global model of the whole growth facility. The commercial program CRYSVUN has been used for that, operating on an unstructured finite element computational mesh. This model included the diffusive and radiative heat transfer, the released latent heat but not the convection in the melt. The silica ampoule and the encapsulant layer were treated as transparent. The main difficulty with the global model was the treatment of the control thermocouples. They were placed closely in front of the heaters. This, however, does not mean that they have had the same temperature. Indeed, because of high temperature and small size, they are strongly radiationally coupled to

all visible surfaces around and experience a somehow averaged temperature. Direct numerical treatment of such fine details is numerically unfeasible. To deal with this situation we assumed the thermocouples to be infinitesimal and placed at a certain distance from the heater. This distance was tuned via radial positioning of the control thermocouples so that the calculated solidification interface, its depth and the growth velocity matched the results of preliminary growth experiments.

A general aim of the computations is to find out a strength of RMF forcing that provides possibly a flat solidification interface. The problem can be turned `upside down' assuming that such a forcing exists if the target condition is satisfied in a good approximation. With the 'almost flat' phase boundary target condition the top of the crystal domain can then be approximately substituted with a plane isothermal surface and the heat flux in the crystal can be found along the solidification interface. Together with the desired growth velocity this flux introduces a Neumann type boundary condition at the assumed flat bottom of the melt domain. Certainly, if we constrain both the front shape and the heat flux through it, there will be a residual temperature difference along the bottom. Varying the forcing parameter, however, we can find such a value where the difference to the melting temperature becomes minimal. The absolute value of this temperature residual is proportional to the deflection from the flat solidification interface. Thus, the specific inverse task turns out to be simpler than the general direct problem due to the fixed geometry of the target conditions.

The flow problem was solved numerically by a spectral code including the natural convection due to buoyancy. The heat flux boundary conditions were evaluated from the solution of the global model. The main parameters of this system are the magnetic Taylor number $\mathrm{Ta} = \mathrm{B}_{\mathrm{eff}}^2 (\mathrm{H}/2)^4 \omega\sigma\rho / 2\eta^2$ and the aspect ratio H/R of the molten zone, where ω is the magnetic field frequency, and σ, ρ, η are the electrical conductivity, density, and dynamic viscosity of the melt, respectively. H is the height and R the radius of the melt. In each growth the field strength was increased during the course of the growth in order to compensate the influence of the decreasing melt height on the flow.

4. Results and discussion

The RMF causes primarily an azimuthal rotation of the melt. This primary motion is accompanied by a secondary, radial-meridional melt flow due to the no-slip condition on the solid boundaries of the liquid. This motion is directed radially inwards at the solid-liquid phase boundary. Figure 2 shows this RMF driven flow and its influence on the resulting temperature distribution.
An optimal forcing of the melt flow with respect to the flattening of the phase boundary was found for a Taylor number of $\mathrm{Ta} \approx 10^5$. Fig. 3 shows that the RMF driven flow reduces the residual temperature, *i.e.*, the front deflection considerably. It is interesting to observe that the resulting geometry of the phase boundary is no more the same curvature along the radius but obeys a w-type geometry.

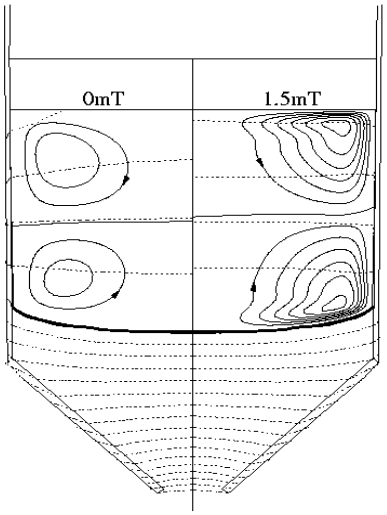

Fig. 2. Effect of the RMF on the melt flow and the temperature field. The phase boundary is shown with a thick line. Streamlines of buoyancy and RMF driven flow are shown with solid lines. The dotted lines show the temperature isolines with a step of 1 K.

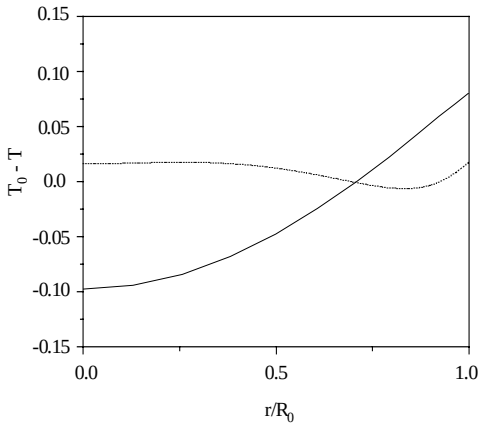

Fig. 3. Residual dimensionless temperature along the target (planar) phase interface at an aspect ratio of 1.5 with zero forcing (solid line) and at the magnetic Taylor number $Ta = 110^5$ (dotted line).

The experimentally obtained phase boundaries during the growth process are shown in Fig. 4. At the intermediate aspect ratio of H/R = 1.5 (S4 in Fig.4) a w-shaped interface is found confirming qualitatively the computed result shown in Fig. 3.

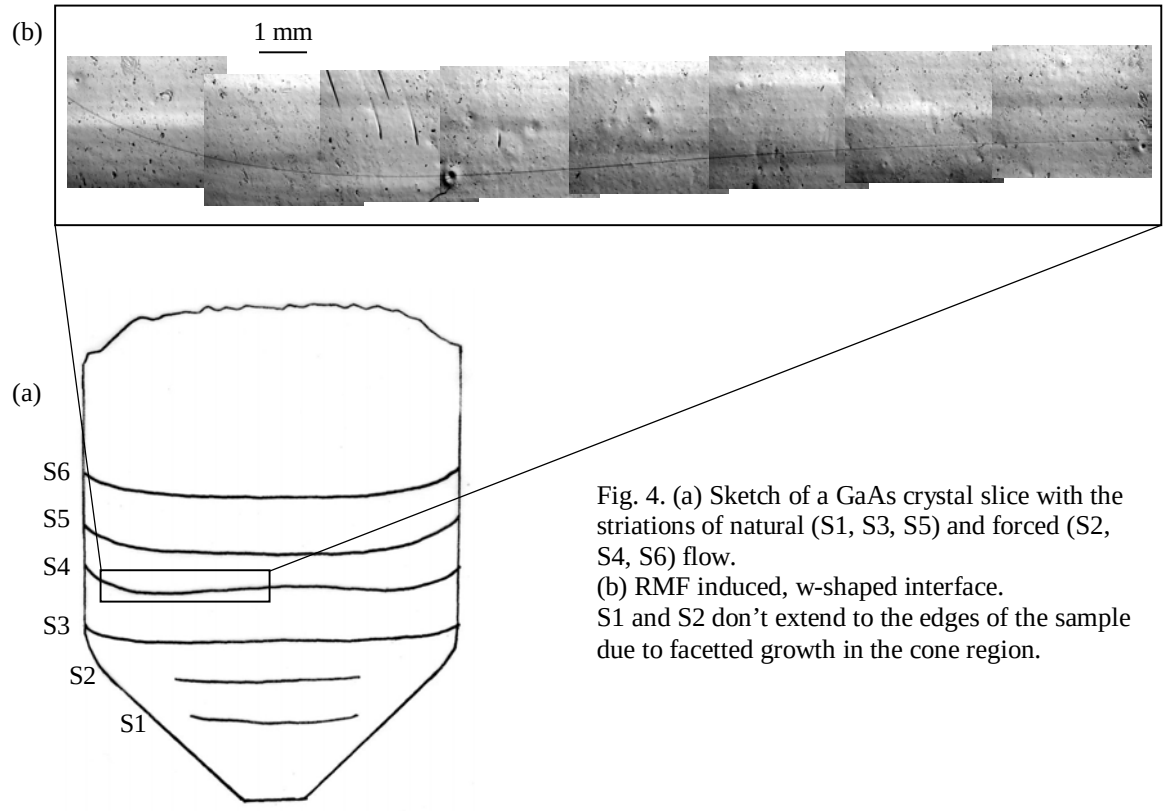

Fig. 4. (a) Sketch of a GaAs crystal slice with the striations of natural (S1, S3, S5) and forced (S2, S4, S6) flow.
(b) RMF induced, w-shaped interface.
S1 and S2 don't extend to the edges of the sample due to facetted growth in the cone region.

The RMF causes a decrease of the radial temperature gradients as it is evident from the interface deflections under forced flow which are detected to be considerably lower than the deflection of the natural interfaces at similar aspect ratios. As an example, the maximal deflection of the striation S6 is 3.89mm or 7.65% with respect to the crystal diameter compared to 4.92 mm or 9.68% of a natural striation.

In response to the melt convection the shape of the phase interface is quite inert. In a good approximation it can be assumed that the variation of the melt flow induced by a short RMF pulse is solely compensated by changing the growth velocity. Hence, knowing the average growth velocity and its variation due to the RMF it is possible to deduce the variation of the thermal gradient in the melt. This enables the short-pulse RMF as a measurement tool of heat flux in the melt. As predicted by numerical flow modelling the growth velocity becomes lower in the outer region of the melt and higher in the central part due to the forced convection. By comparing the measured variation of the gradient with the variation of the heat flux computed numerically the absolute value of the axial temperature gradient can be roughly estimated to be around 0.75K/cm.

5. Summary

First results on the VGF-RMF growth of two inch, Si doped GaAs crystals are presented. The RMF is shown to be a convenient tool to explore and control the heat transfer at the solid-liquid interface. The local temperature field is evaluated by RMF-induced dopant striations which mark the current phase interface. Under forced flow a significant reduction of the bowing of a nominally concave interface is obtained. In agreement with computed results even a wavy interface is observed at an aspect ratio of about 1.5. Hence, a significant influence on the solid-liquid interface is possible by application of an RMF of suitable strength. In addition, interface marking by RMF-pulses allows the direct measurement of the variation of the growth velocity and the local thermal gradients in the melt.

References

[1] O. Pätzold, I. Grants, U. Wunderwald, K. Jenkner, A. Cröll, G. Gerbeth (2002): Effect of rotating magnetic field on the heat flow in vertical gradient freeze growth of GaAs, submitted to J. Crystal Growth

UPGRADE OF THE GAS DYNAMIC TRAP: PHYSICAL CONCEPT AND NUMERICAL MODELS

Andrey V. Anikeev[1], Petr A. Bagryansky[1], Alexander A. Ivanov[1], Alexander N. Karpushov[1], Klaus Noack and Svetlana L. Strogalova[1]

1. Introduction

The Budker Institute of Nuclear Physics Novosibirsk develops a project of an intense 14 MeV neutron source (NS) based on a gas dynamic trap (GDT) which is mainly intended for fusion material irradiation. Its actual disadvantage is the lack of data for the parameter range of the projected GDT-NS which does not yet allow a reliable interpolation from the parameters of the existing GDT experimental facility to the neutron source. At present, experimental and computational researches are carried out to complete the required data base.

So far, rather promising results have been achieved concerning the main plasma-physical issues like MHD stability, longitudinal confinement, cross-field transport and the fast ion behaviour [1,2]. For the investigations in the latter field the Integrated Transport Code System (ITCS) has been used [3,4]. These investigations must be extended to a higher level of plasma parameters. To this end a substantial upgrade of the GDT facility is planned. The main subsystems which are to be upgraded are the neutral beam injection (NBI) system and the magnetic field power supply. The higher power and the longer duration of the injection will provide a substantially higher energy content of the fast ions and, consequently, will increase the electron temperature.

In recent years several transport codes have been developed and applied for computational studies in parallel to the experimental research. They have been coupled by appropriate data file transfers to the ITCS. The report is focused on the application of the code system to study possible operation regimes of the upgraded GDT. The results of numerical simulations enable us to conclude that an electron temperature of 250-300 eV can be achieved in the GDT-Upgrade with a NBI of 10 MW and a duration of 3-6 ms. The maximum fast ion density in the region of their turning points is estimated at ~5×10^{13} cm^{-3}.

2. Physical Concept of GDT-Upgrade

The two-component hydrogen plasma consists of a warm target plasma and a fast ion population which is produced by a high-energetic NBI. The target plasma is composed of electrons and low-energetic ions both with isotropic Maxwellian distributions because their behaviour is collision dominated. The electron temperature during a shot lies between 3-120 eV and the plasma density is in the range of $(1\text{-}20) \times 10^{13}$ cm^{-3}. The target plasma is produced by a plasma gun and/or by gas puffing. Different methods of cold-gas fuelling have been proposed and were experimentally tested at the GDT [5]. The NBI consists of six injectors with injection energies in the range of 12.5-17.5 keV. The duration of the NBI pulse is 1.0-1.2 ms, the total injected power exceeds 4 MW. The neutral beams are partly trapped by the target plasma as results of charge-exchange and ionisation processes by target plasma ions and electrons. The ionised part of the neutral beams represents the source of the fast ions. The energy relaxation of the fast

[1] Budker Institute of Nuclear Physics, Novosibirsk, Russia

ions is determined by electron and ion drag, their angular scattering by Coulomb collisions with the plasma ions and their loss by charge-exchange processes with the neutral gas. The target plasma dynamics is mainly controlled by gas dynamic longitudinal losses, cross-field transport, radiation losses and neutral gas ionisation [2]. The neutral gas inside the GDT chamber consists of slow hydrogen molecules and atoms, Frank-Condon neutrals and fast charge-exchange atoms. The neutral gas transport is determined by the interactions with target plasma, fast ions and with the chamber wall.

Table 1: Parameters of GDT and GDT-Upgrade

Parameter	**GDT**	**GDT-Upgrade**
Magnetic Field		
at midplane	0.21 T	0.35 T
mirror ratio	≈50	45
Pressure/Pa	$7*10^{-5}$	$7*10^{-5}$
NBI Parameters		
injection angle/°	45	45
beam energy/keV	12.5-17.5	25-30
power/MW	4.2, maximum	10, contin.
duration/ms	1.1	3-6
ion optics/∅ cm	13	21, focussing
angular spread/°	1 x 2	2
Plasma Gun		
temperature/eV	10-15	10
plasma flux/atom A	≈500	1076

The feasibility to achieve both high electron and ion temperatures of the dense target plasma as required by the GDT-NS project has not yet been demonstrated experimentally. Therefore, the development of approaches enabling the study of plasma physical issues related to plasma confinement in the GDT at source relevant conditions is mandatory. The new NBI system with a beam energy of 25-30 keV, a beam current up to 80 atom Amperes, and a pulse duration between 3-6 ms is proposed for the GDT-Upgrade. A ramp-type injection of totally about 10 MW will be possible. The construction of the coil system allows to strengthen the magnetic field by a factor of about 1.5 by increasing the capacity batteries. Possible parameters of GDT-Upgrade and those of the GDT are given in Table 1.

Besides the upgrading an extension of the GDT facility is also under way. A further mirror coil will be installed in a distance of about 0.5 m to the standard one producing in this way a new mirror section with a mirror ratio of about 1.2-1.4 and with a magnetic field strength of about 2.5-5 T in its centre [6]. Its target plasma is delivered from the central cell. Using two of the new injectors for perpendicular neutral beam injection in the centre of the small mirror fast ion densities up to 10^{14} cm^{-3} should be achieved during a shot of about 1 ms. The mean energy of the fast ions is expected in the range of 10-15 keV. So, a plasma-β is expected in the range of 30-50 per cent in a strong magnetic field. In this respect the conditions are nearly the same as expected in the source region of the GDT-NS. The experiments at the small mirror which is named as *Synthesised Hot Ion Plasmoid (SHIP)* represent the first stage of the research programme for GDT-Upgrade. A schematic view of SHIP is given in Fig. 1.

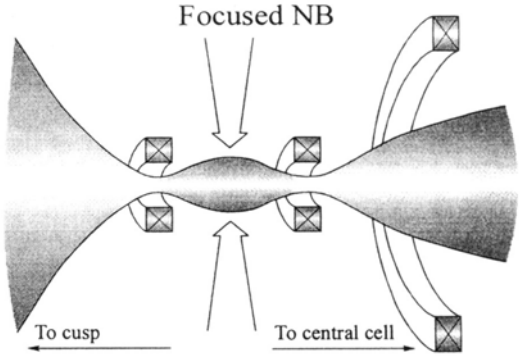

Fig.1: SHIP – Synthesised Hot Ion Plasmoid.

3. Integrated Transport Code System

In order to simulate the plasma behaviour in the existing GDT experiment as well as that in the GDT-based neutron source the Integrated Transport Code System has been developed. Existing stand-alone codes calculating the target plasma, the fast ions and the neutral gas in the GDT were coupled by an appropriate file transfer. The purpose of the ITCS is the calculation of physical effects connected with these particle fields. It considers the full dependence of the transport phenomena on space, time, energy and angle variables as well as the interactions between the fields. To check the capabilities of the physical models that have been incorporated in the ITCS the overall comparison between numerical and experimental results has been made. The ITCS includes the FITC [4], MCFIT [7], TUBE [5] and NEUSI [8] codes. The code FITC has been developed to calculate the dynamics of the GDT target plasma transport under neutral beam heating. It allows to compute the time dependent radial profiles of the target plasma density $n(r,t)$, its ion and electron temperatures $T_i(r,t)$, $T_e(r,t)$ and the heating powers $P_{Fi}(r,t)$, $P_{Fe}(r,t)$ delivered from the fast ions to the target plasma by ion and electron drag, respectively.

The Monte Carlo code MCFIT simulates the linear transport of neutral beam produced energetic ions in given magnetic field, target plasma and neutral gas. The code describes the relevant transport processes with a minimum of approximations. In the GDT-Upgrade the high fast ion energy content results in a high value of plasma-β which reaches almost sixty per cent. The high-β effect causes a deformation of the magnetic field and, consequently, of the fast ion distribution too. To consider this non-linear effect the time dependent azimuthal fast ion currents calculated by MCFIT were used to compute the correction of the magnetic field. Then, this β-corrected, time dependent magnetic field was used by MCFIT and FITC in an iteration procedure.

The neutral gas transport module consists of the codes TUBE and NEUSI. The Monte Carlo code TUBE simulates the time dependent coupled transport of H atoms and H_2 molecules inside the central chamber of the GDT. The code NEUSI bases on the Integral Transport Method. It calculates the radial, axial and time dependent densities of fast and slow H atoms and of H_2 molecules in the central cell of the GDT.

4. Application of the ITCS for GDT-Upgrade Calculations

The GDT components which are mainly to be upgraded are the neutral beam injection system and the magnetic field. A preliminary study of possible variants was made by means of the FITC module. From the variants considered one was selected to study the behaviour of the iteration procedure between the ITCS modules and, finally, to

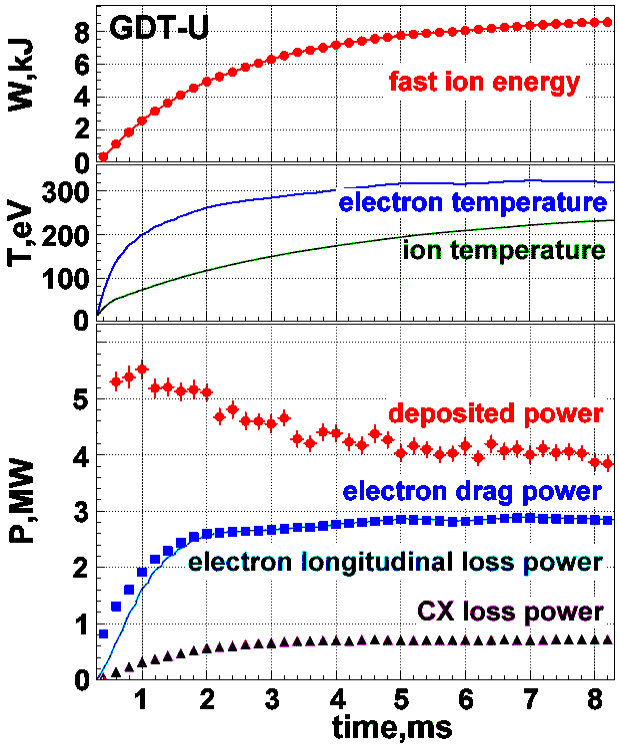

Fig. 2: Dynamics of plasma parameters for GDT-Upgrade.

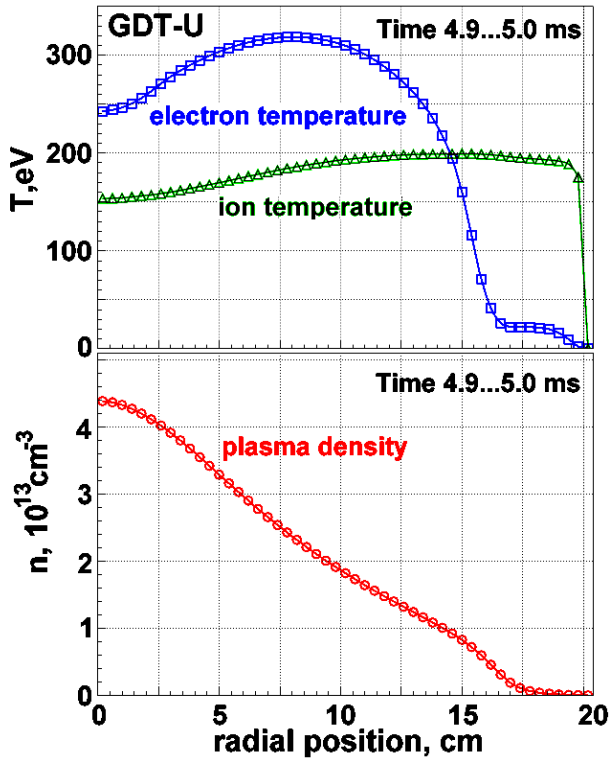

Fig. 3: Radial profiles of the plasma density and temperatures at 5 ms after start of the NBI.

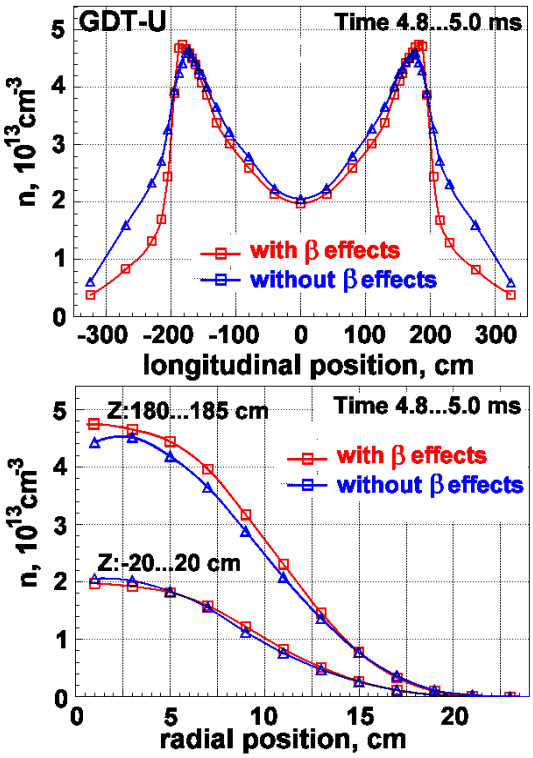

Fig. 4: Fast ion longitudinal on axis and radial density profiles with and without finite beta effects.

study the resulting fast ion distribution in detail. The main parameters of this variant are given in Table 1 and compared with those of the high-ß experiments at GDT.

To get initial approximations $n^0(r,t)$ and $T_e^0(r,t)$ for the target plasma density and electron temperature, respectively, a self-consistent calculation for target plasma and fast ions was performed by means of FITC. This calculation was made for the case «without neutral gas» and for a pulse duration of six milliseconds. The following MCFIT pre-calculation was made with the target plasma $(n,T_e)^0$. This calculation yielded the source distribution of «warm neutrals» which resulted from charge exchange ionisation of the neutral beam particles in the centre of the GDT and several partial integrals of the fast ion distribution function f^0. Then, the source of warm neutrals was used in the neutral gas calculations by means of TUBE and NEUSI. The information on the fast ion distribution served as input for the approximate fast ion model of NEUSI. TUBE calculated a discrete, time dependent distribution of hydrogen atoms and molecules reflected from the inner surface of the chamber wall into the device. Finally, using this surface source and the source of warm neutrals NEUSI calculated the gas as discrete distribution $g^0(r,z,t)$ in that volume which is occupied by fast ions.

After the pre-calculations several iteration steps were performed each consisting of a fast ion calculation by MCFIT and a target plasma calculation by FITC, respectively. In step i MCFIT computed the radial profiles of the electron drag power $P_{Fe}^i(r,t)$. This power distribution served as input for FITC which computed the new target plasma $(n,T_e)^i$. The MCFIT calculation was done using a target plasma which was mixed with the preceding steps according to the relationship

$$\overline{(n,T_e)}^{i-1} = 0.5\cdot(n,T_e)^{i-1} + 0.25\cdot(n,T_e)^{i-2} + 0.25\cdot(n,T_e)^{i-3}.$$

5. Results and Conclusions

After five iteration steps the relative changes of the radial averaged target plasma density and electron temperature were in the range of five to ten per cent over the whole pulse. The main characteristics of the GDT-Upgrade plasma after the 5^{th} iteration are shown in Fig. 2. The global parameters are close to the equilibrium values at 5-6 ms. Fig. 3 shows the electron temperature and the plasma density 5 ms after the start of the NBI. The computed maximum electron temperature exceeds 300 eV, the plasma density reaches 4.4×10^{13} cm^{-3}.

The influence of the β-effect on the fast ion distribution is illustrated in Fig. 4. Obviously, the β-corrected magnetic field leads to a non-adiabatic movement of a part of the fast ions near to the axis. Nevertheless, the β-effect keeps relatively small. The results of numerical simulations enable us to conclude that the electron temperature of 250-300 eV will be achieved in the GDT-Upgrade with a 10 MW, 25 keV NBI system. The maximum fast ion density in the region of their turning points is estimated to reach almost 5×10^{13} cm^{-3}.

The preparation of the ITCS modules for the application on SHIP is under way. The linear MCFIT code must be extended to account for other non-linear effects too, e.g. for collisions between the fast ions and for their interactions with the neutral beams. Moreover, in contrast to GDT-Upgrade a strong interaction between the fast ions and the fast neutral gas component must be expected.

References

[1] P. A. Bagryansky, et al.(1999), Recent experiments at the Gas Dynamic Trap, Trans. Fusion Technol., 35, 79

[2] A. V. Anikeev, et al. (2000), Fast ion relaxation and confinement in the gas dynamic trap, Nuclear Fusion, 40, 753

[3] A. V. Anikeev, et al. (2001), An integrated transport code system for the calculation og multi-component, high-ß plasmas in the gas dynamic trap, Trans. Fusion Technol., 39, 183

[4] A. N. Karpushov, et al. (2000), Integrated transport code system for multi-component high-ß plasmas in the gas dynamic trap, Proceedings of the 27^{th} EPS Conference on Controlled Fusion and Plasma Physics, Vol. 24B, 920

[5] P. A. Bagryansky, et al. (1999), Effect of fast Ti-deposition on gas recycling at the first wall and on fast ion losses in the GDT experiment, J. Nucl. Mater., 265, 124

[6] A. A. Ivanov, et al. (1999), Gas dynamic trap experiment: Status and perspectives, Trans. Fusion Technol., 35, 107

[7] K. Noack, G. Otto and S. Collatz (1999), Transport simulations of fast ion and neutral gas dynamics during GDT experiments, ibid., 218

[8] S. Collatz and K. Noack (1999), NEUSI – A code for the calculation of neutral particle densities inside the plasma region of the GDT, ibid., 375

Summaries of research activities

Thermo-fluiddynamics

M. Beyer
H. Carl
H.-M. Prasser
U. Rindelhardt
H. Rußig
A. Schaffrath
P. Schütz
M. Tamme
S. Weichelt
W. Zimmermann

Thermo hydraulic test facility TOPFLOW

TOPFLOW is a large-scale high-temperature and high-pressure test facility for generic research in the field of transient two-phase flow and for studies of safety relevant fluid-dynamic problems in components of nuclear power plants and chemical installations. The design project of the facility is completed. The new facility will be built using components of the former NOKO test facility of the Research Centre Jülich, which helped to reduce costs to 9 - 10 million DM. The parameters allow experiments with steam-water mixture at saturation pressures of up to 10 MPa. The facility disposes of an electrical heating power of 4 MW. The construction work of the building is completed, major parts of the equipment are installed. The commissioning is expected for the second half of 2002.

A. Böttger
G. Grunwald
T. Höhne
S. Kliem
H.-M. Prasser
K.-H. Richter †
U. Rohde
M. Tamme
J. Zschau

Coolant mixing in pressurised water reactors

The work aims at the measurement of temperature and boron concentration distributions at the core entrance during main steam-line break and boron dilution transients. Experiments were carried out at the mixing test facility ROCOM modelling the German KONVOI type pressurised water reactor in the scale of 1:5. The disturbance is modelled by injecting salt water as a tracer into the affected loop. A new quality of tests is achieved by using wire mesh-sensors with about 1000 measuring positions in the downcomer and at the core entrance, the high measuring frequency (up to 200 Hz), the variability of the four-loop test facility and the direct comparison to CFD calculations. In the reported period experiments on the mixing of ECC water injected into the cold leg were performed. For creating the characteristic density difference between coolant inventory and ECC water, sugar (glucose) was added to the injected plug. The results show different flow and mixing patterns for large and small Froude numbers. A flow chart with critical boundaries between momentum driven and gravity driven flow as a function of the Froude number was obtained. The results are relevant for the understanding of the pre-stressed thermal shock (PTS) phenomenon as well as for the coupling between neutron kinetics and thermo hydraulic codes.

Supported by BMWi and VGB

A. Böttger
J. Fietz
H. Futterschneider
D. Hoppe
H.-M. Prasser
J. Zschau
C. Zippe
W. Zippe

Development and calibration of two-phase flow measurement techniques

The qualification of the diversified level indication system for boiling water reactors developed by FZR was continued according to the German reactor safety regulations. The qualification procedure and the series production will be accomplished by an industrial supplier of reactor instrumentation. FZR contributes as a scientific consultant and performed finalising development tasks.

The first electrode-mesh sensor for high temperature and pressure was successfully tested during condensation experiments carried out in co-

operation with the University of Applied Sciences Zittau/Görlitz. The construction is based on a complicated sensor body with hidden cooling channels and blind holes for the fixing of the electrodes. It was manufactured by laser sintering, which is a computer-controlled rapid-prototyping technique.
For the calibration of two-phase instrumentation as well as for the contactless measuring of phase and concentration distributions with a high resolution in space and time, a pulsed X-ray tomograph was built and put into operation. The multi-purpose device is located in a lead tunnel. It consists of a source with a maximum acceleration voltage of 150 kV, a pulse length of 0.3 ms and a pulse current of about 300-500 mA.
For the investigation of transport processes in bubble columns and foam layers, a PET detector is under construction. The scanner will allow to measure the distribution of a tracer marked by a positron emitting nuclide with a time resolution of better than 1 s. It consists of 8 axial layers with 16 BGO detectors each. The spatial resolution will be in the range of a centimetre. The mechanical construction of the detector arrays and the development of the signal acquisition circuitry was finished.

Supported by DFG

A. Grahn

Thermoconvection and instabilities at the boundary layer of two non-miscible liquid reacting components

After completion of the experiments the work was concentrated on modelling. The developed 2D CFD code for the numerical investigation of the flow instabilities was extended by a model for the chemical reactions in the liquid bulks of the two reacting non-miscible components distant from the interphase boundary. Previously, the theoretical model only allowed chemical reactions at the contact boundary. In this way, the accuracy of the model was increased. This is especially important, if the reaction goes slower than the mass transfer.

D. Baldauf
D. Lucas
E. Krepper
H.-M. Prasser
C. Zippe
W. Zippe

Transient two-phase flows in pipelines

In the frame of a project sponsored by BMWi flow patterns and their evolution in a vertical tube are investigated. In the last year, the experiments on flow pattern evolution along the vertical pipe of 51.2 mm inner diameter were repeated with improved instrumentation. The wire-mesh sensor with 1200 frames per second and 16 x 16 measuring points was replaced by a second generation device consisting of two sensors with 24 x 24 points, mounted in a short distance above each other. The measuring frequency was increased to 2500 frames per second. The data base for model development was significantly extended in this way. An important new quality is given by the possibility to measure the gas phase velocity distribution over the cross section. Based on this data modelling efforts were continued to describe the evolution of bubble size specific radial gas fraction profiles.
Local void probes with integrated micro-thermocouple were used in a transient condensation experiment performed in co-operation with the University of Applied Sciences Zittau/Görlitz. A slightly inclined horizontal heat exchanger pipe of the emergency condenser for BWRs

(NOKO) was placed in a cooling basin and connected to a pressure vessel. The pipe was either evacuated or filled with a non-condensible gas (air) at a given pressure. The probes recorded the process of condensation after the steam injection from the pressure vessel into the experimental pipe. They show the fill-up of the pipe with condensate and the replacement of the non-condensible gas. For this purpose the conductivity and temperature signals of the new type of probes are correlated.

Supported by BMWi
Co-operation with University of Applied Sciences Zittau/Görlitz

Safety and effectiveness of chemical processes

G. Hessel
H. Kryk
W. Schmitt
T. Seiler
F.-P. Weiß

Environmentally safe process control and condition monitoring in chemical plants using neural networks

In this interdisciplinary project, the Fraunhofer Institute for Environmental, Safety, and Energy Technology UMSICHT, the Degussa AG Radebeul, and the Institute of Safety Research of Forschungszentrum Rossendorf have collaborated since August 1998. The project aims at the development of neural networks for the diagnostics of discontinuous chemical processes and their test application in a production plant. It is the goal to achieve an early detection of deviations from the optimum, environmentally safe operation of a chemical plant.
In the framework of the project, an online-monitoring system was developed for hydrogenation reactors working in semi-batch mode. The system was integrated in a Batch Information Management System, which was implemented in the process control system of an industrial multi-purpose reactor. The on-line capability of the new system was demonstrated in a series of 15 batches.

Supported by BMBF

G. Hessel
H. Kryk
W. Schmitt
N. Tefera
F.-P. Weiß
T. Willms

Experiments and numerical simulations of exothermic chemical reactions

The detailed knowledge of the reaction kinetics including intermediate products and side reactions with an accuracy as good as possible is a basis for a safe and environmentally compatible process control. The work is concentrated at the hydrogenation of nitro-aromatic compounds. The reaction calorimeter was equipped with a high-accuracy reaction heat measurement based on a heat carrier temperature measurement at the inlet and the outlet of the heating jacket. A Fourier-Transform Infrared Spectrometer (FTIR) was applied for in-situ and on-line concentration measurements inside the calorimeter. An High Performance Liquid Chromatograph (HPLC) unit was used for the calibration of the FTIR. A simplified HPLC analysis method was developed and transferred to the industrial partner.

Supported by industry

Accident Analysis

U. Grundmann
S. Kliem
S. Mittag
U. Rohde

Development, Validation and Application of the Code Complex DYN3D – ATHLET

New macroscopic cross section libraries generated by the 2D neutron transport codes HELIOS and CASMO for a standard loading of a German reference PWR have been connected to DYN3D. Burn-up calculations from the beginning to the end of a typical loading cycle were carried out. Control rod efficiencies and reactivity coefficients were determined to obtain reactor-physical initial conditions for transient analyses.

The validation of the coupled code DYN3D/ATHLET for BWR applications is carried out by means of an OECD/NRC Benchmark comprising a turbine trip transient at the reactor Peach Bottom 2. In the second phase of the benchmark, three-dimensional core simulation for given thermal-hydraulic boundary conditions had to be performed. The DYN3D results for steady-state reactor physical parameters (eigenvalue, power distribution) and for the power peak initiated by pressure increase due to the turbine valve closing show good agreement with the results of the other codes and measurement data.

The semi-analytical perturbation re-construction model (SAPR) for the description of the coolant mixing inside the reactor pressure vessel during pump start-up was implemented into DYN3D. The code complex SAPR-DYN3D was used to perform generic boron dilution analyses with realistic description of coolant mixing. First, the minimum volume of a slug of deborated water was determined, which can cause re-criticality of the scrammed reactor. Further, the analysis of a boron dilution scenario with a maximum slug volume of 36 m³ with a pump start-up after steam generator tube break was performed. The boron dilution in the reactor core causes a super prompt critical reactivity insertion leading to a very short power pulse with a magnitude of more than 7000 MW. The power peak is limited due to the strong Doppler feedback of the fuel temperature. The radial power distribution over the reactor core is very heterogeneous. At the location of the power maximum, coolant boiling with a maximum void fraction of up to 70 % occurs for a short time. However, no increase of fuel cladding temperatures due to the occurrence of heat transfer crisis was obtained and no safety relevant limitations are violated.

Supported by BMWi

E. Krepper
M. Kliem

Computational fluid dynamics simulations of one and two-phase flow

To identify weak points of actual CFD-codes, international benchmark problems have been solved. Calculations were performed and compared with experiments to investigate natural convection in a cube with heated and cold wall at different orientation and for different Rayleigh Numbers. Further calculations were performed experiments at the NOKO test facility modelling an emergency condenser of a BWR power plant, and for side wall heated tanks. Modelling the sub-cooled boiling

near the heated walls, the flow phenomena in the heated tank have been simulated in qualitatively good agreement with the experiments. The formation of sharp layers with different temperature has been observed, which break up suddenly if boiling becomes more intensive.

An experimental set-up (CCEF) has been constructed to validate the porous body model for rod bundles with an-isotropic friction against flow measurements. The set-up consists of a transparent test section (made from plexiglass), were an asymmetric water flow is induced (inlet at the bottom and outlet on the side of the bundle). Velocity fields are measured by LDA, the results are compared with CFD calculations.

Partially funded by BMWi

Materials and components safety

I. Stephan
B. Böhmer
J. Konheiser

Neutron dosimetry

After dismantling of the last irradiation capsules from the irradiation experiment Rheinsberg, all neutron detectors from the experiments RH 5 to 8 were available and were evaluated by gamma spectroscopic measurements. The types of the used detectors permitted to investigate the following reactions: Fe-54 (n, p) → Mn-54, Nb-93 (n, n) → $Nb\text{-}93^{m}$, Nb-93 (n, γ) → Nb-94, Co- 59 (n, γ) → Co-60, Ag-107 (n, γ) $Ag\text{-}108^{m}$. The parameters of the neutron field (thermal and fast neutron fluences, dpa) were determined from the measured reaction rates using the spectrum adjustment programme COSA and were compared with the results of the Monte Carlo neutron field calculation programme TRAMO. In this way a detailed and highly reliable assessment of the neutron fluences was achieved and, thus, an essential condition was created for the evaluation of the neutron effects on the mechanical properties.

H.-W. Viehrig
S. Schneider

Radioisotope laboratory for the machining of specimens for mechanical testing

The licence procedure for the extension of the radioisotope laboratory for material testing is underway. It is planned to reconstitute specimens from broken half Charpy V-notch specimens in order to use the available irradiated material more intensively. The technique is already developed for non-radioactive materials. It uses a stud arc welding set-up. Technology, operation conditions and handling were adapted to hot cell conditions. Therefore, new assemblies and auxiliaries were designed, built and successfully tested. The introduction of the reconstitution technique allows to execute an additional research programme on the effect of annealing using the already tested specimens from the Rheinsberg irradiation programme.

H.-W. Viehrig
J. Böhmert

Toughness characterization based on the dynamic master curve approach

The master curve approach allows to quantify the variation of fracture toughness with the temperature in the lower ductile-to-brittle transition

temperature range. The approach was recently standardised in ASTM but is only applicable for quasi-static loading conditions. The use of the instrumented Charpy impact tests has been investigated deeply for the master curve concept. A study was concerned with dynamic testing of specimens from different thickness layers of a thick rolling plate made from ASTM A 533 B cl. 1 reactor pressure vessel steel. In principle, the study proved the suitability of the master curve approach to describe the material behaviour in the lower transition region under dynamic loading conditions. The dynamically measured reference temperature T_o is clearly higher than the quasi-static one, but there is a good correlation between both parameters. However, the fracture toughness values determined under dynamic loading do not strictly follow the course of the master curve. Instead, characteristic deviations were observed. Under dynamic loading conditions special attention has to be paid to censoring of the specimens and the limitation of the measuring capacity. Eventually, the reliable measurement of the J-integral was found to be a problem at the onset of cleavage fracture using instrumented Charpy impact tests.

G.Müller
J. Böhmert

Effect of hydrogen on the toughness of reactor pressure vessels

The influence of hydrogen on the Charpy V-notch impact toughness was investigated as contribution to the BMWi project "Effect of hydrogen on toughness of reactor pressure vessels". Charpy standard specimens from different types or heats of reactor pressure vessel steel were pre-charged by hydrogen up to saturation and tested with a Charpy impact tester. The hydrogen charging condition was chosen in such way that the real condition in the PWR coolant system was simulated. The dependence of the Charpy impact energy on the temperature was compared with the temperature dependence of uncharged specimens from the same heat.
Definitely, there are no systematic deviations between both material conditions. Thus, an embrittlement effect due to hydrogen uptake is rather improbable for unirradiated materials and under dynamic loading.
Furthermore the results of irradiation experiments and of post-irradiation investigations of aged RPVs were analysed for a potential hydrogen effect. Under the condition of a flowing coolant and, thus, a low hydrogen activity no hydrogen-induced embrittlement can be observed. A stagnant coolant, however, can produce high hydrogen concentration and strong embrittlement. Under this circumstance a synergistic influence of the hydrogen content on the radiation embrittlement and vice versa cannot be excluded.

Co-operation with Institut für Festkörperphysik und Werkstoff-forschung
Supported by BMWi

J. Böhmert
A. Gokhmann
A. Ulbricht

Modelling of neutron embrittlement mechanisms

The evolution of both the vacancy clusters and copper-rich precipitates in a neutron-irradiated reactor pressure vessel steel was investigated starting at nucleation stage and ending in the coarsening stage. For this, characteristic VVER-type reactor conditions were considered. Vacancy cluster evolution in the nucleation stage was analysed by on computer simulation. During the deterministic and coarsening stage elastic

interaction between the iron matrix and vacancy clusters was taken into account and provided the stability of the peak of the size distribution function with increasing neutron fluence. That was also observed experimentally. Clusters dynamic approach was used to analyse the evolution of copper precipitates. Here, the size distribution function, mean radius, number density of copper precipitates, and the concentration of free Cu atoms were calculated in dependence on the irradiation time.

Supported by BMWi Co-operation with the RRC Kurchatov Institute and the South Ukrainian Pedagogical University Odessa

The results of the kinetic models were compared with SANS experiments which were carried out with specimens irradiated at surveillance positions of VVER reactors. There is sufficient correspondence between experiment and model. In case the evolution of the copper precipitates the correspondence is only sufficient if the evolution kinetics is assumed to be of intermediated type. This means that the kinetic is not only controlled by diffusion but also by interfacial processes.

H.-G. Willschüz, E. Altstadt

In-vessel corium retention in LWRs

Considering the hypothetical core melt down scenario for a light water reactor (LWR) the failure mode of the reactor pressure vessel (RPV) has to be investigated to determine the possible loads on the containment. The FOREVER-experiments, currently underway at the KTH Stockholm (Sweden), are simulating the thermal and pressure loads on the lower head for a corium melt pool with internal heat sources. Due to the multi-axial creep deformation of the vessel with a non-uniform temperature field these experiments are an excellent source of data for the validation of numerical creep models. Therefore, a 2D Finite Element model has been developed based on a commercial multi-purpose code ANSYS. Using the CFD module the temperature field within the vessel wall is calculated.

The transient structural mechanical calculations consider the visco-plastic material behaviour of the French pressure vessel steel 16MND5. The vessel failure prediction is based on a damage criterion which was integrated into the ANSYS code. The creeping and thereby the failure of the vessel sensitively depends on the temperature. Considering the FOREVER-EC2 experiment, a good prediction of the vessel failure time and an accurate prediction of the failure location seems to be possible. For experiments with INCONEL 600 penetrations a 3D-model was developed and the according material and creep data basis has been generated.

After analysing the calculations, it seems to be advantageous to introduce a vessel support, which can unburden the vessel from a part of the mechanical load and, so, avoid the vessel failure or at least prolong the time to failure. This can be a possible accident mitigation strategy. Additionally, it is possible to install an absolutely passive automatic control device to initiate the flooding of the reactor pit to ensure external vessel cooling in the event of a core melt down.

Supported by BMWi Co-operation with the KTH Stockholm

E. Altstadt
H. Carl
R. Weiss

Water hammers in pipelines

Water hammers can occur in case of an inflow of sub-cooled water into pipes or other parts of the equipment, which are filled with steam or steam-water mixture. They also may appear as the consequence of valve closing or opening actions or of breaks in pipelines, with single phase or two-phase flow. In the latter case, shock waves in two-phase flow must be expected. In all cases, strong dynamic stresses are induced in the wall of the piping system.

The influence of the fluid-structure interaction on the magnitude of the loads on pipe walls and support structures has not yet been completely understood. In case of a dynamic load caused by a pressure wave, the stresses in pipe walls, especially in bends, are different from the static case. On the one hand the propagating pressure wave may cause additional non-symmetric deformations that increase the equivalent stresses in comparison to the symmetric load created by a static internal pressure. On the other hand, fluid-structure interaction causes the structure to deform, which leads to a decrease of the resulting stresses. The lack of experimental data obtained at well defined geometric boundary conditions is a significant obstacle for the validation of codes which consider fluid-structure interaction. Furthermore, up to now the feedback from structural deformations to the fluid mechanics has not fully been implemented in existing codes. Therefore, at FZR a cold water hammer test facility (CWHTF) was designed and built up in 2000. An experimental programme covering pressure amplitudes up to 106 bars has been realised. The dependence of the maximum pressure on the residual air, the bouncing velocity and on the valve opening time was investigated.

Supported by EU

M. Werner
E. Altstadt

Finite Element-Modelling of crack propagation

A 3-dimensional FE-Model of a Charpy specimen is used to simulate the crack propagation. This model includes the kinematics of the roll bearings as well as the crack opening mechanism. The plastic material behaviour is considered. The crack propagation is controlled by a strain based damage criterion which was integrated into the finite element code ANSYS. The numerical stability could be improved in this way. However, the crack length achieved till the failure of the specimen is underestimated in case of very ductile materials.

Particle and radiation transport

B. Böhmer
J. Konheiser

Neutron and gamma dosimetry of reactor pressure vessels

The EU TACIS project SRR2/95/Part2 "Development of Advanced Methods for Evaluation of Irradiation Embrittlement of WWER-1000/230 Type RPV`s" was completed with several improvements of neutron data and theoretical methods for the computation of reactor pressure vessel neutron load.

Neutron data libraries frequently used in reactor pressure vessel dosimetry were compared and tested using activation measurement data from the international ex-vessel inter-comparison experiment at the VVER-1000 Balakovo-3. Besides different data for neutron transport calculations also different detector cross section data files were investigated. At simple testing models the impact of frequently used group approximations on neutron and photon fluence parameters was studied by comparison of DORT and MCNP calculation results. The fast neutron results relevant for pressure vessel embrittlement agree reasonably well for different libraries and calculation methods but the results for low energy neutrons and photons as well as for deep penetrations differ strongly in many cases.

Supported by BMWi, EU

B. Böhmer
J. Konheiser
H. Kumpf
K. Noack
I. Stephan

Increasing the accuracy of neutron and gamma fluence determination

The TRAMO code was qualified to an improved treatment of the thermal neutron region and for coupled neutron-gamma transport problems. Thermal neutron results for core and water zones of an one-dimensional reactor model were verified by comparison with MCNP results using different thermal scattering models. Measurements of neutron and gamma spectra were performed in cooperation with the Technical University Dresden and the University of Applied Sciences Zittau/Görlitz at the reactors AKR and ZLFR. Similar measurements were accomplished at the exits of the horizontal experimental channels of both reactors behind and inside different combinations of steel-, iron and water modules. To facilitate the absolute calibration of the reactor power reaction rates of activation and fission detectors were measured in the reactor cores. Calculations with the code MCNP based on a detailed model of the AKR core were used to provide calculated reaction rates needed for the AKR power calibration.

Supported by DFG

R. Küchler
K. Noack
T. Zorn

Transport of radio-nuclides in the water unsaturated zone

The verification of mathematical models of the dissolution of minerals in the unsaturated zone is underway. For that batch and column experiments are carried out and modelled by means of numerical codes. Concerning the dissolution of gypsum it turned out, that the electrolytic conductivity and pH-value measured in the equilibrium state in the batch test were in good agreement with numeric results. The solution leaking from the 1 m-column turned out to be saturated with gypsum. The calculated conductivity and the calcium and sulphate concentrations well agree with the values measured in batch tests. Comparing the dissolution of gypsum in batch and column experiments one can state that under unsaturated conditions only a very small part of the grain surface is chemically active. The model shows that the water saturation and the Darcy-velocity mainly determine the extent of this active surface part.

C. Beckert
K. Noack

Photo-neutron source at ELBE

At the radiation source ELBE a photo-neutron source for time-of-flight experiments is developed to measure neutron cross sections of construction materials of fusion and fission reactors and of radioactive waste. For the design calculations of this photo-neutron source the Monte Carlo code MCNP4C2 was used. The considered components were the beam line, the photo-neutron target and the beam dump inside the neutron laboratory, and the collimator in the concrete wall. At first, electron, photon and neutron fluxes were calculated for lead and mercury targets. The results were compared with those obtained by the code FLUKA, which is used at the Institute for Nuclear and Hadron Physics. The values for the electrons and photons showed a good agreement, but the neutron spectra distinguished remarkably regarding the form and the location of the maximum. The wide spreading of the electron beam behind the target demands to install a beam dump as near as possible to the target and to enlarge the front target surface. With a corresponding beam dump model and two different collimator configurations calculations of the time dependent neutron flux were done for the planned measuring position. The calculation results show for the standard pulse frequency of 13 MHz, that not every electron pulse can be used for neutron production because of the relatively short flight path from the source to the detector.

Supported by DFG

Liquid metal magnetohydrodynamics

G. Gerbeth
S. Eckert
V. Galindo
A. Cramer
W. Witke

Crystal Growth and Metallurgy

First GaAs crystals have been grown at the new Vertical Gradient Freeze facility of Bergakademie Freiberg. A rotating magnetic field (RMF) is applied there in order to control the heat transfer in the melt by a tailored flow structure. The RMF action on the melt flow was especially designed in order to obtain an almost flat phase boundary during the growth process. The experiments confirmed the numerical results, in particular with respect to the occurrence of wavy-shaped solid-liquid phase boundaries at intermediate aspect ratios of the molten zone. In a good agreement between theory and experiment the RMF offers a significant influence on the geometry of the phase boundary. In addition, short pulses of the RMF can be used to mark striation lines in the grown crystal.

The investigations for the metallic fibre production by melt extraction lead to the proposal of a crucible-free technology by feeding the inductor from above with a plate of the base material. The key point was to find some solution that the highest temperature develops at the lower plate end and not in the mid-plane of the inductor. This was solved by a special inductor design. For the fine-casting of aluminium calculations and model experiments with a cold eutectic melt provide sufficient evidence that the filling velocity of the melt can be reduced by the application of an external steady magnetic field.

Supported by SMWK, DFG, BMBF

T. Weier
G. Mutschke
J. Hüller
U. Fey
G. Gerbeth

Supported by BMBF-VDI

Boundary layer control in electrolytes

In order to continue the experimental programme on the electromagnetic influence of lift- and drag coefficients a large NACA 0015 profile has been equipped with surface covering electrodes and permanent magnets. Related flow measurements have been performed at HSVA Hamburg. They revealed the strong effect of the electromagnetic forces on the lift enhancement and allowed to extract the relevant scaling laws. Numerical simulations confirm the found dependencies. The obtained influences on lift and drag values are of relevance for applications at ship components like stabilising foils or rudders. However, the energetic effort for this flow control turned out to become high for velocities above 10m/s. Further studies are focused on the reduction of this energetic effort but keeping the obtained flow effects.

S. Eckert
W. Witke
Th. Gundrum
J. Hüller
F. Stefani
G. Gerbeth

Supported by EU, DFG

Measuring Techniques

The ultrasonic Doppler velocimetry (UDV) provides a full profile of the velocity field. Applications to liquid metals, however, are limited by the maximum temperature of about 150°C of the ultrasonic transducers. Therefore, ultrasonic wave-guides have been developed and tested in order to overcome the temperature limitations. Successful test have been performed for flows of sodium and lead-bismuth up to temperatures of 400°C. The integrated system of wave-guides, transducers and the Doppler system worked stable and robust. The wetting between the wave-guide and the melt turned out to be of crucial importance for the system.

The idea of a magnetic tomografie, i.e. reconstruction of the flow field out of external magnetic field measurements, has been further developed. The demonstration experiment was designed and built up. It required a series of water pre-experiments in order to design a fully three-dimensional flow structure.

F. Stefani
Th. Gundrum
G. Gerbeth

Supported by DFG, EU

Dynamo Effect

There was not yet any new measuring campaign at the Riga dynamo facility. Nevertheless, the work in this field received a major impulse by getting a European dynamo project funded from Brussels. Only this enables us to intensify these activities in the future. The theoretical analysis of the available data provided a clear evidence for a non-trivial back-reaction of the magnetic field on the flow. Besides the overall breaking of the flow rate due to the induced magnetic field, there is a significant change of the velocity profile leading to the measured differences between the magnetic field distributions in the self-excited and the saturated regimes. The available results of the Riga dynamo have been summarised as an invited review paper for the journal "Reviews of Modern Physics".

Publications

Publications in scientific and technical journals and in conference proceedings, monographs

Altstadt, E.; Willschuetz, H.-G.
Pre-test Calculations for a Core Meltdown Experiment
19. CAD-FEM Users´ Meeting, 17.-19. Oktober 2001, Berlin, Potsdam, Germany, Proceedings Vol. 1, 1.6.9

Anikeev, A.; Karpushov, A.; Collatz, S.; Noack, K.; Otto, G.; Strogalova, S.
An Integrated Transport Code System for the Calculation of Multi-Component, High-ß Plasmas in the Gas Dynamic Trap
3rd International Conference on Open Magnetic Systems for Plasma Confinement, July 3-6, 2000, Tsukuba, Japan; Proc. published in Transactions of Fusion Technology, Vol 39, p. 183 (2001)

Anikeev, A. V.; Bagryansky, P. A.; Ivanov, A. A.; Karpushov, A. N.; Noack, K.; Strogalova, S. L.
Upgrade of the Gas Dynamic Trap: Physical Concepts and Numerical Models
28th EPS Conference on Plasma Physics and Controlled Fusion, Madeira, Portugal, 18-22 June 2001, Proceedings, Poster P1.026

Beckert, C.
TransRay - ein dreidimensionaler Zellcode auf der Grundlage der Ray-Tracing Technik
Jahrestagung Kerntechnik 2001, Dresden, 15.-17. Mai 2001, Tagungsbericht S. 51-54

Beyer, M.; Carl, H.
Unterstützung der ukrainischen Aufsichtsbehörde beim Aufbau einer modernen KKW-Überwachung
Jahrestagung Kerntechnik 2001, Dresden, 15.-17. Mai 2001, Tagungsbericht, S. 463-466

Böhmer, B.; Konheiser, J.; Brodkin, E.; Egorov, A.; Vikhrov, V.; Zaritsky, S.; Polke, E.
Verification of neutron transport calculations for nonstandard pressure vessel surveillance positions in the VVER-1000 Novovoronesh-5
Jahrestagung Kerntechnik 2001, Dresden, 15.-17. Mai 2001, Proceedings pp. 37-42

Böhmert, J.; Ulbricht, A.; Kruykov, A.; Nikolaev, Y.; Dmitry, E.
Composition Effects on the Radiation Embrittlement of Iron Alloys
Effects of Radiation on Materials: 20th International Symposium, ASTM STP 1405, S.T. Rosinski, M. L. Grossbeck, T. R. Allen and A. S. Kumar, Eds., American Society for Testing and Materials, West Conshohocken, PA, 2001, pp. 383-398

Böhmert, J.; Viehrig, H.-W.; Ulbricht, A.
Irradiation effects on toughness behaviour and microstructure of VVER-type Pressure Vessel Steels
Journal of Nuclear Materials 297 (2001) 251-261

Böhmert, J.; Weiß, R.; Webersinke, W.
Anwendung eines Laserextensometers zur Ermittlung von Risswiderstandskurven
Vortrag auf 1. Anwendersymposium Laserextensometrie, Merseburg, Juni 2001, Tagungsband, S. 516-524

Cumblidge, Stephen E.; Catchen, Gary L.; Motta, Arthur T.; Brauer, G.; Böhmert, J.
Effects of Neutron Irradiation and Thermal Annealing on Model Alloys using Positron Annihilation Techniques
Effects of Radiation on Materials: 20th International Symposium, ASTM STP 1405, S. T. Rosinski, M. L. Grossbeck, T. R. Allen and A. S. Kumar (Eds.), American Society for Testing and Materials, West Conshohocken, PA, 2001, pp. 247-261

Eckert, S.; Gerbeth, G.; Witke, W.; Langenbrunner, H.
MHD Turbulence Measurements in a Sodium Channel Flow Exposed to a Transverse Magnetic Field
International Journal of Heat and Fluid Flow, Vol. 22/3, 2001, 358-364

Ezsöl, G.; Szabados, L.; Prasser, H.-M.
Local void measurements in integral-type experiments simulating nuclear power plant transients
5th World Conference on Experimental Heat Transfer, Fluid Mechanics and Thermodynamics, Thessalonoki, Greece, 24-28 September 2001, Vol. 2, pp. 1637 - 1641.

Gailitis, A.; Lielausis, O.; Platacis, E.; Dement'ev, S.; Cifersons, A.; Gerbeth, G.; Gundrum, T.; Stefani, F.; Christen, M.; Will, G.
Magnetic Field Saturation in the Riga Dynamo Experiment
Physical Review Letters 86 (2001) 3024-3027

Gailitis, A.; Lielausis, O.; Platacis, E.; Gerbeth, G.; Stefani, F.
On the results of the Riga dynamo experiments
Magnetohydrodynamics 37, No. 1/2 (2001) 71-79

Gailitis, A.; Lielausis, O.; Platacis, E.; Gerbeth, G.; Stefani, F.
Riga Dynamo Experiment
Dynamo and Dynamics, a Mathematical Challenge, NATO Science Series II: Mathematics, Physics and Chemistry, Vol. 26, Edited by P. Chossat, D. Armbruster, I. Oprea, Kluwer, Dordrecht, 2001, pp. 9-16

Grants, I.; Gerbeth, G.
Stability of axially symmetric flow driven by a rotating magnetic field in a cylindrical cavity
Journal of Fluid Mechanics (2001), Vo. 431, pp 407-426

Grundmann, U.; Kliem, S.
Analyses of the OECD - MSLB Benchmark with the Codes DYN3D and DYN3D/ATHLET
Transactions of the American Nuclear Society, June 2001, Volume 84, page 23 - 25

Hainoun, A.; Schaffrath, A.
Simulation of subcooled flow instability for high flux research reactors using the extended code ATHLET
Nuclear Engineering and Design 207 (2001) 2, 163-180

Hainoun, A.; Schaffrath, A.
Simulation of subcooled flow instability for high flux research reactors with ATHLET
Kerntechnik 66 (2001) 4,214-216

Hermann, R.; Priede, J.; Behr, G.; Gerbeth, G.; Schultz, L.
Influence of growth parameters and melt convection on the solid-liquid interface during RF-floating zone crystal growth of intermetallic compounds
Journal of Crystal Growth 223 (2001) 577-587

Hessel, G.; Hulzer, G.; Kryk, H.; Schmitt, W.
Investigation for Safer Initiation of Grignard Reactions
Proceedings of the 3rd European Congress of Chemical Engineering, Nuremberg 26-28 June 2001, on ECCE-CD / Contents / 2. Sustainable Development, 2.2 Chemical Risk Management

Hicken, Enno F.; Dreier, J.; Meseth, J.; Schaffrath, A.
Erprobung passiver Komponenten für den SWR 1000 - Ergebnisse von Experimenten an den Versuchsanlagen PANDA und NOKO
Jahrestagung Kerntechnik 2001, 15.-17. Mai 2001, Dresden, Berichtsheft der Fachsitzung "Grossversuche zur verbesserten Sicherheitsbewertung von LWR", S. 137-167

Höhne, T.; Rohde, U.; Prasser, H.-M.
Post Test CFD Calculations of Experiments at the ROCOM Mixing Test Facility related to Boron Dilution and Cold Water Transients
CFX Users Conference 2001,28-30 May 2001, Berchtesgaden

Kliem, S.; Prasser, H.-M.
A semi-analytical model for the description of coolant mixing inside the KONVOI reactor pressure vessel during pump start-up
Jahrestagung Kerntechnik 2001, Dresden, 15.-17. Mai 2001, Tagungsbericht, S. 107-112

Kliem, S.; Prasser, H.-M.; Höhne, T.; Rohde, U.
Development and Application of a Fast Running Model for the Description of Coolant Mixing Inside the Pressure Vessel of Pressurized Water Reactors
11. AER Symposium on VVER Reactor Physics and Reactor Safety, Csopak, Hungary, September 24-28, 2001, Proceedings pp. 449-463

Kliem, S.; Seidel, A.
Comparison of the Results of the 6. Dynamic AER Benchmark - Main Steam Line Break in a NPP with VVER-440
11. AER Symposium on VVER Reactor Physics and Reactor Safety, Csopak, Hungary, September, 24-28, 2001, Proceedings pp. 295-329

Kozmenkov, Y.; Orekhov, Y.; Grundmann, U.; Kliem, S.; Rohde, U.; Seidel, A.
Development and Benchmarking of the DYN3D/RELAP5 Code System
Jahrestagung Kerntechnik 2001, Dresden, 15 - 17 Mai 2001, Tagungsbericht S. 15 - 18.

Krepper, E.
CHT'01 validation exercise: Natural convection in an air filled cavity
Int. Conf. on "Advances in computational heat transfer", Palm Cove, Australien Mai 2001, Proc. Vol. 2, pp. 1351-1356

Krepper, E.; Aszodi, A.; Prasser, H.-M.
Experimental and numerical investigation of one and two phase natural convection in storage tanks
4th International Conference on Multiphase Flow, New Orleans, Lousiana, USA - May 27 to June 1, 2001, Conference-CD, Paper 515

Krepper, E.; Hicken, E. F.; Jaegers, H.
Investigation of natural convection in large pools on the example of heating up the secondary side of an emergency condenser
Int. Conf. on "Advances in computational heat transfer", Palm Cove, Australien Mai 2001, Proc. Vol. 2, pp. 835-842

Krepper, E.; Hicken, E.-F.; Jaegers, H.
Investigations of natural convection in large pools during the heating up of the secondary side of an emergency condenser
Jahrestagung Kerntechnik 2001, Dresden 15-17 Mai 2001, Tagungsband S. 99-102

Li, W.; Hicken, Enno F.; David, Paul H.; Prasser, H.-M.; Baldauf, D.; Zschau, J.
Messung der Kondensatfilmdicken in einem dampfdurchströmten horizontalen Rohr
Jahrestagung Kerntechnik 2001, Dresden, 15./17. Mai 2001, Tagungsbericht S. 103-106.

Lucas, D.; Krepper, E.; Prasser, H.-M.
Bubble Size Distributions and Radial Profiles in Vertical Pipe Flow
3rd European Congress of Chemical Engineering, Nuremberg, 26 - 28 June, 2001, Conference-CD, File 532.htm; Abstract in Chemie Ingenieur Technik 73 (2001) 640

Lucas, D.; Krepper, E.; Prasser, H.-M.
Development of bubble size distributions in vertical pipe flow by consideration of radial gas fraction profiles
4th International Conference on Multiphase Flow, New Orleans, May 27 - June 1, 2001, Conference-CD, Paper 378

Lucas, D.; Krepper, E.; Prasser, H.-M.
Model for radial gas fraction profiles in vertical pipe flow
Jahrestagung Kerntechnik 2001, Dresden, 15.-17. Mai 2001, Tagungsband, S. 83-86

Lucas, D.; Krepper, E.; Prasser, H.-M.
Modeling of radial gas fraction profiles for bubble flow in vertical pipes
Ninth International Conference On Nuclear Engineering - ICONE-9, Nice, France, April 8-12, 2001, Conference-CD, Paper 279

Lucas, D.; Krepper, E.; Prasser, H.-M.
Prediction of radial gas profiles in vertical pipe flow on basis of the bubble size distribution
International Journal of Thermal Sciences 40 (2001) 217-225

Manera, A.; Prasser, H.-M.; van der Hagen, Tim H. J. J.; Mudde, R. F.; Kruijf, Willi J. M. de
A comparison of void-fraction measurements during flashing-induced instabilities obtained with a wire-mesh sensor and a gamma-transmission set-up
4th International Conference on Multiphase Flow, New Orleans, Lousiana, USA - May 27 to June 1, 2001. Proc. CD-ROM, paper 436.

Mittag, S.; Kliem, S.; Weiß, F.-P.; Kyrki-Rajamäki, R.; Hämäläinen, A.; Langenbuch, S.; Danilin, S.; Hadek, J.; Hegyi, G.; Kuchin, A.; Panayotov, D.
Validation of Coupled Codes for VVERs by Analysis of Plant Transients
Proceedings of OECD / CSNI workshop on Advanced Thermal--hydraulic and Neutronic Codes - Current and Future Applications, Barcelona (Spain), 10-13 April, 2000, NEA/CSNI/R(2001)2/VOL1 309-324

Mittag, S.; Kliem, S.; Weiß, F.-P.; Kyrki-Rajamäki, R.; Hämäläinen, A.; Langenbuch, S.; Danilin, S.; Hadek, J.; Hegyi, G.; Kuchin, A.; Panayotov, D.
Validation of coupled neutron kinetic / thermal-hydraulic codes Part 1: Analysis of a VVER-1000 transient (Balakovo-4)
Annals of Nuclear Energy 28/9 (2001) 857-873

Mutschke, G.; Gerbeth, G.; Shatrov, V.; Tomboulides, A.
The scenario of three-dimensional instabilities of the cylinder wake in an external magnetic field. A linear stability analysis
Physics of Fluids Vol. 13, No 3, (March 2001) pp 723-734

Prasser, H.-M.; Dudlik, A.; Schönfeld, S. B. H.; Fahlenkamp, H.; Schlüter, S.
Prevention of Water Hammer in Pipelines in Case of Emergency Shut-Off by Fast Acting Valves
ECCE-3, 3rd European Congress on Chemical Engineering, Nürnberg, 26.-28. Juni 2001, Proc. on CD-ROM, Poster P2 - 60.

Prasser, H.-M.; Krepper, E.; Lucas, D.
Fast wire-mesh sensors for gas-liquid flows and decomposition of gas fraction profiles according to bubble size classes
5th World Conference on Experimental Heat Transfer, Fluid Mechanics and Thermodynamics, Thessalonoki, Greece, 24-28 September 2001, Vol. 2, pp. 1135 - 1140.

Prasser, H.-M.; Lucas, D.; Krepper, E.
Decomposition of gas fraction profiles according to bubble size classes
4th International Conference on Multiphase Flow, New Orleans, Lousiana, USA - May 27 to June 1, 2001, proc. CD-ROM, paper 159.

Prasser, H.-M.; Scholz, D.; Zippe, C.
Bubble size measurement using wire-mesh sensors
Flow Measurement and Instrumentation 12/4 (2001) 299-312

Prasser, H.-M.; Zschau, J.; Peters, D.; Pietzsch, G.; Taubert, W.; Trepte, M.
Fast Wire-Mesh Sensor for Two-Phase Flow Visualisation with 10 000 Frames per Second
ECCE-3, 3rd European Congress on Chemical Engineering, Nürnberg, 26.-28. Juni 2001, Proc. on CD-ROM, poster P16 - 1.

Richter, S.; Aritomi, M.; Prasser, H.-M.; Hampel, R.
Methods for studies on bubbly flow characteristics applying an electrode-mesh tomograph
4th International Conference on Multiphase Flow, New Orleans, Lousiana, USA - May 27 to June 1, 2001. Proc. CD-ROM, paper 848.

Rindelhardt, U.
Nutzung erneuerbarer Energien zur Stromerzeugung in den neuen Bundesländern
3. Energietechnisches Kolloquium der BTU Cottbus, 6.9.2001, in: BTU Forschungshefte Energie(Hrg. B. Schieferdecker, Ch. Fünfgeld): Energietag Brandenburg 2001, Beitrag 12

Rindelhardt, U.
Photovoltaische Stromversorgung
B. G. Teubner Stuttgart-Leipzig-Wiesbaden

Rindelhardt, U.
Stromerzeugung aus erneuerbaren Energien in Ostdeutschland
Elektrizitätswirtschaft 100, Heft 25, S.30-39

Rindelhardt, U.
Windenergie - heute und morgen
6. Symposium "Energie und Energieversorgungssysteme der Zukunft", Lauta, 18. Mai 2001, Tagungsband Beitrag 12

Rohde, U.
The Modeling of Fuel Rod Behaviour under RIA Conditions in the Code DYN3D
Jahrestagung Kerntechnik 2001, Dresden, Deutschland, 15.-17.5.2001, Tagungsband S. 339-344, Inforum Verlags- und Verwaltungsgesellschaft mbH, Bonn 2001

Schäfer, F.
Investigations of Natural Circulation Instabilities in VVER-type Reactors at LOCA Conditions
4th International Symposium on Safety and Reliability Systems of PWRs/VVER, 2001 May 14-17, Brno, Czech Republic

Schäfer, F.; Krepper, E.
Verification of the code ATHLET by post-test analysis of two experiments performed at the integral test facility CCTF
Annual Meeting on Nuclear Technology, Dresden, May 15-17 2001,Proc. p. 87-90

Schäfer, F.; Krepper, E.; Weiß, F.-P.
Post-test analysis of two accident management experiments performed at the Bethsy test facility using the code ATHLET
ICONE - Ninth International Conference on Nuclear Engineering, Nice, France, April 8-12 2001

Schaffrath, A.; Krüssenberg, A.; Weiß, F.-P.; Hicken, E.-F.; Beyer, M.; Carl, H.; Prasser, H.-M.; Schuster, J.; Schütz, P.; Tamme, M.
TOPFLOW - a new multipurpose thermalhydraulic test facility for the investigation of steady state and transient two phase flow phenomena
Kerntechnik 66 (2001) 4 209-212

Schaffrath, A.; Krüssenberg, A.-K.; Fjodorow, A.; Gocht, U.; Lischke, W.
Modeling of Condensation in Horizontal Tubes
Nuclear Engineering and Design 204 Issue 1-3 (2001) 251-265

Schaffrath, A.; Krüssenberg, A.-K.; Weiß, F.-P.; Carl, H.
TOPFLOW - eine neue Mehrzweck-Thermohydraulik-Versuchsanlage zur Untersuchung stationärer und transienter Zweiphasenströmungen
Jahrestagung Kerntechnik 2001, Dresden, 15.-17. Mai 2001, Tagungsbericht S. 125-131

Seidel, A.; Kliem, S.
Solution of the 6. Dynamic AER Benchmark Using the Coupled Code DYN3D/ATHLET
11. AER Symposium on VVER Reactor Physics and Reactor Safety, Csopak, Hungary, September 24-28, 2001, Proceedings pp. 251-267

Stefani, F.; Gerbeth, G.
A toy model for inverse dynamo theory
Physics of the Earth and Planetary Interiors 128, No. 1-4 (2001), pp. 109-124

Ulbricht, A.; Böhmert, J.; Viehrig, H.-W.
Beziehungen zwischen Mikrostruktur und Zähigkeitseigenschaften von neutronenbestrahlten WWER-Reaktordruckbehälterstählen
Jahrestagung Kerntechnik 2001, Dresden, Germany, 15.-17. Mai 2001, S. 697-700

Viehrig, H.-W.; Böhmert, J.; Dzugan, J.
Anwendung des Instrumentierten Kerbschlagbiegeversuch zur Ermittlung von Referenztemperaturen nach dem Master-Curve-Konzept
Materialwissenschaft und Werkstofftechnik, Vol. 32, No. 6, June 2001, pp. 568-573

Viehrig, H.-W.; Böhmert, J.; Dzugan, J.; Richter, H.
Master Curve Evaluation of Irradiated Russian VVER Type Reactor Pressure Vessel Steels
Effects of Radiation on Materials: 20th International Symposium, June 2000, ASTM STP 1405, S.T. Rosinski, M.L. Grossbeck, T.R. Allen, and A.S. Kumar, Eds., American Society for Testing and Materials, West Conshohocken, pp. 109-124

Werner, M.; Altstadt, E.; Perov, S.
Schwingungsmodellierung von WWER-Reaktoren zur Untersuchung von Störfallszenarien
27. MPA-Seminar, Sicherheit und Verfügbarkeit in der Energietechnik, Band 1 und 2, Stuttgart, 4 .- 5. 10. 2001, Artikel 9

Willschuetz, H.-G.; Altstadt, E.; Weiss, F.-P.; Sehgal, B. R.
Simulation of Scaled Core-Meltdown-Experiments and Investigation of a Possible Vessel Support against Failure
16th International Conference on Structural Mechanics in Reactor Technology SMiRT16, Washington, DC, USA, August 12-17, 2001, Paper No. 1145

Willschuetz, H.-G.; Sehgal, B. R.
The EC-FOREVER-2 experiment: the pre-test analysis and comparisons with the experiment
OECD LOWER HEAD FAILURE, 4th Program Committee Meeting, March 5-7, 2001, Sandia National Laboratories, Albuquerque, New Mexico, USA, Proceedings Paper No 8.6

Willschütz, H.-G.; Altstadt, E.; Sehgal, B. R.; Weiß, F.-P.
Coupled Thermal Structural Analysis of LWR Vessel Creep Failure Experiments
Nuclear Engineering and Design, Elsevier, 208 (2001)265-282

Willschütz, H.-G.; Altstadt, E.; Weiss, F.-P.; Sehgal, B. R.
Pre-Test Calculations for the EC-FOREVER-2-Experiment
Jahrestagung Kerntechnik 2001, Dresden, 15.-17. Mai, Tagungsband S. 187-192

Yeoh, G. H.; Tu, J. Y.; Krepper, E.; Prasser, H.-M.
Numerical investigation and measurement of transient two-phase boiling flow
14th Australasian Fluid Mechanics Conference, Adelaide Australia, 10-14 December 2001, Proceedings pp. 865-868

Other oral and poster presentations

Böhmer, B.; Borodkin, G.; Kumpf, H.
Dort-MCNP Discrepancies for a Simple Testing Model - Proposal of a Calculational Neutron-Gamma Benchmark.
WGRD VVER Meeting, April 23 -25, 2001, Rez, Czech Republic

Böhmer, B.; Hansen, W.; Konheiser, J.; Mehner, H.-C.; Noack, K.; Unholzer, S.
Information About a New Neutron-Gamma Reactor Experiment
WGRD VVER Meeting, April 23 -25, 2001, Rez, Czech Republic

Böhmert, J.; Müller, G.; Willschütz, H.-G.; Sehgal, B. R.
Analyse der Schädigung eines Druckbehälters in Simulationsexperimenten von nuklearen Kernschmelzunfällen
DGM-Tagung Werkstoffprüfung 2001, Bad Nauheim, 6. - 7. 12. 2001

Bojarevics, A.; Gelfgat, Yu.; Gerbeth, G.; Cramer, A.
Effect of a superimposed DC magnetic field on the melt flow in an induction furnace experimental model
Lecture at: International Scientific Colloquium "Modelling for Saving Resources" Riga, May 17-18, 2001

Eckert, S.
Behavior of gas bubbles in liquid metals
Lecture series 'Fluid Dynamics in Continous Casting', von Karman Institute for Fluid Dynamics, Brüssel, 23-27 April 2001

Gailitis, A.; Lielausis, O.; Platacis, E.; Gerbeth, G.; Stefani, F.
Riga Dynamo Experiment
Lecture at European Geophysical Society, XXVI General Assembly, Nice (France), March 25-30, 2001

Gailitis, A.; Lielausis, O.; Platacis, E.; Gerbeth, G.; Stefani, F.
The Saturation Regime of the Riga Dynamo Experiment: Observational Facts and their Interpretation
4. MHD-Tage, Ruhr-Universität Bochum, 01-02 Oktober 2001

Gerbeth, G.
Magnetofluiddynamik - Beeinflussung metallischer Schmelzen mittels elektromagnetischer Felder
Einladungsvortrag im Kolloquium "Physik amorpher und flüssiger Legierungen", TU Chemnitz, 24.04.2001

Gerbeth, G.
Tailored magnetic fields in industrial crystal growth, levitation, and melt extraction
Lecture at: Int. Seminar on "Electromagnetic Control of Liquid Metal Processes" Coventry, UK, June 27-29, 2001

Gerbeth, G.
The inverse approach to Magnetofluiddynamics
Lecture at ABB Process Industries, Västeras, Sweden, 27.03.2001

Gokhman, A.; Böhmert, J.; Ulbricht, A.
Elastic effect on the evolution of cluster ensembles in irradiated reactor pressure vessel steels
V. Research Workshop Nucleation Theory and Applications, Dubna, April 2-28, 2001

Höhne, T.
Kühlmittelvermischung in Druckwasserreaktoren
Jahrestagung Kerntechnik 15.-17. Mai 2001, Dresden, Poster

Schaffrath, A.; Hicken, E. F.; Prasser, H.-M.; Palavecino, C.
Experimental Investigation of the Emergency Condenser of the SWR1000
Centro Atomico Bariloche, Argentinien, 28.11. - 04.12.2001

Schaffrath, A.; Krüssenberg, A.-K.; Alt, S.
Modeling of Condensation inside Horizontal Tubes
Centro Atomico Bariloche, Argentinien, 28.11.-04.12.2001

Schaffrath, A.; Krüssenberg, A.-K.; Prasser, H.-M.
Investigation of Two Phase Flow in Vertical Pipes
Centro Atomico Bariloche, Argentinien, 28.11.-04.12.2001

Schaffrath, A.; Krüssenberg, A.-K.; Prasser, H.-M.; Lucas, D.
Untersuchung von Zweiphasenströmungen in vertikalen Rohren
Seminar des Lehrstuhls Nukleare und Neue Energiesysteme, Ruhr-Universität Bochum 03.07.2001

Schaffrath, A.; Krüssenberg, A.-K.; Weiß, F.-P.; Hicken, E. F.
TOPFLOW - eine neue Mehrzweckthermohydraulikversuchsanlage zur Untersuchung transienter Zweiphasenströmungen
Seminar des Lehrstuhls für Nukleare und Neue Energiesysteme, Ruhr-Universität Bochum, 03.07.2001

Schaffrath, A.; Krüssenberg, A.-K.; Weiß, F.-P.; Prasser, H.-M.
TOPFLOW - a new multipurpose test facility for the investigation of transient two phase flows
Centro Atomico Bariloche, Argentinien, 26.11. - 04.12.2001

Schmitt, W.
Fehlerermittlung mit neuronalen Netzen
DECHEMA-Kursus "Sicherheitstechnik in der chemischen Industrie", 17.09. - 21.09.2001, Universität Dortmund, in Modul II: Methoden der Schwachstellen und Risikoanalyse, S. 1-20

Stefani, F.; Gerbeth, G.; Gailitis, A.; Lielausis, O.; Platacis, E.
Das Rigaer Dynamoexperiment: Wie man ein Magnetfeld aufrührt
Vortrag im "Geophysikalischen Institutsseminar" der Uni Göttingen, 19. Juni 2001

Stefani, F.; Gerbeth, G.; Gailitis, A.; Lielausis, O.; Platacis, E.
Wie man ein Magnetfeld aufrührt: Zu den Ergebnissen des Rigaer Dynamoexperiments
Vortrag im Seminar "Nichtlinearität und Unordnung in komplexen Systemen" der Universität Magdeburg, 18. Juni 2001

Ulbricht, A.; Böhmert, J.; Strunz, P.; Dewhurst, C.; Mathon, M. H.
Structure Investigations on Russian Reactor Pressure Vessel Steels by Small Angle Neutron Scattering
International Conference on Neutron Scattering 2001, München, September 9-13, 2001

FZR-Reports and other publications

Baldauf, D.; Christen, M.; Fietz, J.; Hampel, U.; Hoppe, D.; Prasser, H.-M.; Will, G.; Zippe, C.; Zschau, J.
Tomographisches Messverfahren für die Gasverteilung in einer Axialpumpe bei Zweiphasenbetrieb
Wissenschaftlich-Technische Berichte / Forschungszentrum Rossendorf; FZR-336, November 2001

Bergmann, U.
Ultraschallverfahren zur Rissfortschrittsmessung für die Ermittlung von Risswiderstandskurven
Wissenschaftlich-Technische Berichte / Forschungszentrum Rossendorf, FZR-330, September 2001

Beyer, M.; Carl, H.
Unterstützung der ukrainischen Behörden beim Ausbau der verbesserten betrieblichen Überwachung für die KKW Rovno und Saporoshje
Wissenschaftlich-Technische Berichte / Forschungszentrum Rossendorf; FZR-332 September 2001

Gavrilas, M.; Höhne, T.
OECD/CSNI ISP NR. 43 Rapid Boron Dilution Transient Tests For Code Verification Post Test Calculation With CFX-4
Wissenschaftlich-Technische Berichte / Forschungszentrum Rossendorf; FZR-325 Juli 2001

Gerbeth, G.; Eckert, S.; Stefani, F.; Cramer, A.; Weier, T.
Innovationskolleg "Magnetofluiddynamik elektrisch leitfähiger Flüssigkeiten"
Abschlußbericht, Juli 2001 zu den FRZ-Teilprojekten A3,A4,B1,B3,C4,D3

Grundmann, U.; Kliem, S.; Mittag, S.; Rohde, U.; Seidel, A.; Panayotov, D.; Ilieva, B.
Adaption, Validierung und Anwendung fortgeschrittener Störfallanalysecodes mit 3D Neutronenkinetik - WTZ mit Bulgarien
Wissenschaftlich-Technische Berichte / Forschungszentrum Rossendorf; FZR-328 August 2001

Grunwald, G.; Höhne, T.; Prasser, H.-M.; Rohde, U.
Kühlmittelvermischung in Druckwasserreaktoren Teil 1: Möglichkeiten geschlossener analytischer Lösungen und Simulation der Vermischung mit CFX-4
Wissenschaftlich-Technische Berichte / Forschungszentrum Rossendorf; FZR-335 Oktober 2001

Höhne, T.; Grunwald, G.; Prasser, H.-M.
Geschwindigkeitsmessungen im Downcomer der ROCOM Versuchsanlage mittels Laser-Doppler Anemometrie im Vergleich mit numerischen Berechnungen
Wissenschaftlich-Technische Berichte / Forschungszentrum Rossendorf; FZR-334 Oktober 2001

Krüssenberg, A.-K.; Schaffrath, A.
Modellierung des Kernkraftwerks Stade Vorarbeiten für Rechnung mit dem Programm RALOC Mod4.0AG Teil2: Rekombinatoren, Eingabedatensatz, Rechnungen
FWS 01-2, Februar 2001

Mössner, T.; Altstadt, E.; Böhmert, J.; Weiß, R.
Erwärmung des Reaktordruckbehälters des Blocks 8 des KKW Greifswald bei der Zerlegung mittels Sägetechnik
Wissenschaftlich-Technische Berichte / Forschungszentrum Rossendorf, FZR-310, Januar 2001

Prasser, H.-M. (Editor)
4. Workshop "Measurement techniques for stationary and transient multiphase flows", Rossendorf, November 16 - 17, 2000
Wissenschaftlich-Technische Berichte / Forschungszentrum Rossendorf; FZR-320, Mai 2001

Weiß, F.-P.; Rindelhardt, U. (Editors)
Annual report 2000 Institute of Safety Research
Wissenschaftlich-Technische Berichte / Forschungszentrum Rossendorf; FZR-316 April 2001

Patents

Patents

Lielausis, O.; Eckert, S.; Gerbeth, G.
Verfahren und Anordnung zur Steuerung der Gasblasenbildung in elektrisch leitfähigen Flüssigkeiten
Patentschrift DE 199 48 879 C1

Prasser, H.-M.; Schlüter, S.; Dudlik, A.
Anordnung zur Verhinderung unerwünschter Drücke beim Absperren oder Drosseln der Flüssigkeitsförderung in einer Rohrleitung
Offenlsgungsschrift DE 199 40 096 A1
Patentschrift DE 199 40 096 C2
Europäische Patentanmeldung EP 1079161 A2

Awards

Awards

Andreas Schaffrath:

Karl-Wirtz-Preis der Deutschen Kerntechnischen Gesellschaft

für Arbeiten zu "Innovativen Reaktorkonzepten, passiven Sicherheitssystemen sowie Zweiphasenströmungen im Allgemeinen"

Gunther Gerbeth, Frank Stefani, Thomas Gundrum:

Forschungspreis des FZR 2001

für ihre Beiträge zum Rigaer Dynamo-Experiment

Guests

Guests

Prof. Dr. Gailitis, Agris
Institute of Physics Riga, Latvia
08.01.2001 - 07.04.2001

Dr. Priede, Janis
Institute of Physics Riga, Latvia
23.04.2001 – 26.05.2001

Dr. Karpuchov, Alexandre
Budker-Institute Novosibirsk, Russia
05.05.2001 – 26.05.2001

Borodkin, Gennadi
SEC NRS of GOSATOMNADZOR Moskau, Russia
06.05.2001 – 17.06.2001
04.11.2001 – 25.11.2001

Davidovsky, Oleg
Umweltministerium der Ukraine, Ukraina
08.05.2001 – 11.05.2001

Tkach, Anatoliy
Kernkraftwerk Saporoshje, Uikrainia
08.05.2001 – 11.05.2001

Lebedyev, Andriy
Kernkraftwerk Saporoshje, Uikrainia
08.05.2001 – 11.05.2001

Chornousova, Lyubov
Umweltministerium der Ukraine, Ukraina
08.05.2001 – 11.05.2001

Dr. Anikeev, Andrey
Budker Institut Novosibirsk, Russia
20.05.2001 – 17.06.2001

Prof. Alian, Atif
Emeritus Professor, Kairo, Egypt
28.05.2001 – 07.06.2001

Prof. Martemianov, Sergei
ESIP University of Poitiers, France
11.06.2001 – 16.06.2001

Dr. Chrainer, Karl
Budker Institut Novosibirsk, Russia
01.07.2001 – 15.07.2001

Prof. Melnikov, Vladimirov
Center of Scientific and Technical Services NUKLID Ltd., Russia
10.09.2001 – 21.09.2001

Dr. Dountzev, Andrei
Novgorod Technical University, Russia
10.09.2001 – 21.09.2001

Dr. Ivanov, Alexandre
Budker Institut Novosibirsk, Russia
28.09.2001 – 12.10.2001

Dr. Bagryansky, Petr
Budker Institut Novosibirsk, Russia
01.10.2001 – 13.10.2001

Dr. Khalimonchuk, Vladimir
Scientific-Technical Centre for Nuclear and Radiation Safety of the Ukraine, Kiew, Ukrainia
18.11.2001 – 01.12.2001

Kuchin, Alexander
Scientific-Technical Centre for Nuclear and Radiation Safety of the Ukraine, Kiew, Ukrainia, Kiew, Ukrainia
18.11.2001 – 01.12.2001

Prof. Slavtchev, Slavcho
Institut of Mechanics Sofia, Bulgaria
19.01.2001 – 24.01.2001

Dr. Feynberg, Olga
Kurchatov Institut Moskau, Russia
17.02.2001 – 21.02.2001

Dr. Ignatiev, Viktor
Kurchatov Institut Moskau, Russia
17.02.2001 – 21.02.2001

Dr. van Outsel, Kristel
Nuclear Research Institute, Studie Centrum voor Kernenergie Mol, Belgium
22.02.2001 – 25.02.2001

Dr. Kozmenkov, Yaroslav
Institute of Physics and Power Engineering Obninsk, Russia
14.05.2001 – 02.06.2001

Prof. Gokhman, Alexander
South Ukrainian Pedagocical University K.D. Ushinski Odessa, Ukrainia
07.07.2001 – 03.09.2001

Dr. Dahlkild, Anders
KTH Stockholm, Schweden
12.07.2001 – 14.07.2001

Prof. Hicken, Enno-Frerich
Forchungszentrum Jülich
15.07.2001 – 03.08.2001
26.09.2001 – 04.10.2001

Myasnikov, Andrey
Kurchatov Institute Moskau, Russia
01.09.2001 – 30.11.2001

Prof. Melnikov, Vladimirov
Novgorod Technical University, Russia
10.09.2001 – 21.09.2001

Dr. Lavrentev, Olga
Chemical Engineering Technion Haifa, Israel
16.09.2001 – 20.09.2001

Peinberg, Janis
Institute of Physics Riga, Latvia
12.10.2001 – 20.10.2001

Dr. Shisko, Andrey
Institute of Physics Riga, Latvia
12.10.2001 – 20.10.2001

Dr. Perov, Sergey
ETC Orgtechdiagnostika, Russia
05.11.2001 – 02.12.2001

D. Bezrukov, Yuri
Engineering and design organisation GIDROPRESS Podolsk, Russia
17.11.2001 – 21.11.2001

Meetings und Workshops

Meetings und Workshops

3. Sitzung des Kompetenzverbundes Kerntechnik
Rossendorf, 23. - 24.01.2001

Workshop „Prozessführung und Zustandserkennung in Chemieanlagen“
Rossendorf, 01.02.2001

Arbeitstreffen „Molten Salt Reactor“
Rossendorf, 17. – 21. 02.2001

Meeting des Sub-Committees „On Dynamic Testing at Intermediate Strain Rates (TC5) der European Structural Integrity Society (ESIS)“
Rossendorf, 30.03.2001

Workshop „Betriebliche Überwachung ukrainischer KKW“
Rossendorf, 08. – 11.05.2001

Abschlußkonferenz des Innovationskollegs "Magnetofluiddynamik elektrisch leitfähiger Flüssigkeiten"
Rossendorf, 17.08.2001

Meeting zum EU-Projekt „Ultraschallmessungen an flüssigen Metallen (HITUV)“
Rossendorf, 23.08.-24.08.2001

Workshop zum EU-Projekt „WAHALoads“
Rossendorf, 04. – 05.10.2001

Kick-off-Meeting zum EU-Projekt FLOMIX
Rossendorf, 19. –20.11.2001

Seminars

SEMINARS

Dr. U. Fischer (FZ Karlsruhe)
Fusionsneutronik – Methoden und Anwendungen
18.01.2001

Dr. A. Cramer
Magnetfeldbeeinflussung der Schmelzeextraktion metallischer Fasern
01.02.2001

Dr. E. Krepper
CFD-Simulation der Naturkonvektion in lokal beheizten Behältern
15.02.2001

Dr. H.-M. Prasser
Bewertung der Genauigkeit von Blasengrößenmessungen mit Gittersensoren
01.03.2001

Dr. M. Werner
Modellierung des Risswachstums in 3-Punktbiegeproben mit einem Finite-Elemente-Code
15.03.2001

Dr. U. Rohde
Modellierung des transienten Brennstabverhaltens bei reaktivitätsinduzierten Störfällen
05.04.2001

T. Seiler, Dr. H. Kryk
Online-Monitoring stark exothermer Reaktionen mit adaptiven Wärmebilanzen
19.04.2001

Dr. E. Altstadt
Modelle für die Werkstoffschädigung bei viskoplastischer Verformung
03.05.2001

Dr. Uhlemann (IFW Dresden)
Wasserstoff als potentielle Versprödungsursache von Reaktordruckbehältern
31.05.2001

Dr. R. Küchler, Dr. T. Zorn
Batch- und Säulenexperimente zur Chemie in der ungesättigten Zone
07.06.2001

Dr. F. Lapicque (Institut National Polytechniue de Lorraine)
Investigation routes for the improvement of Gas-evolving electrochemical cells
29.06.2001

M. Kliem
Strömungssimulation im Reaktorkern in der Näherung eines porösen Körpers
05.07.2001
Dr. A. Dahlkild (KTH Stockholm)
Elektrochemistry and fluid mechnics at Faxén Laboratoriet
13.07.2001

Prof. M. Hinze (TU Dresden)
Mathematische Optimierung für Strömungsprobleme
07.08.2001

Dr. C. Zippe
Visualisierung von periodisch veränderlichen Gasgehaltsfeldern in einer Axialpumpe mit Gamma-Tomografie
30.08.2001

J. Krepel (TU Prag)
Neutron kinetics of reactors with fluid fuel
13.09.2001

Prof. E. Hicken (FZ Jülich)
Sicherheitsphilosophien neuer Reaktorkonzepte I
27.09.2001

Prof. E. Hicken (FZ Jülich)
Sicherheitsphilosophien neuer Reaktorkonzepte II
04.10.2001

S. Kliem
Ein semi-analytisches Modell zur Kühlmittelvermischung und seine Anwendung für die Analyse von Borverdünnungsstörfällen mit DYN3D
11.10.2001

Prof. S. Grossmann (Philipps Universität Marburg)
Scherströmungs-Turbulenz trotz laminarer Stabilität
25.10.2001

Dr. H.-M. Prasser
Experimente zur transienten Kondensation von Dampf bei hohen Wärmeströmen und bei Vorhandensein von nichtkondensierbarem Gas
08.11.2001

Prof. Lischke (Hochschule Zittau/Görlitz)
Reaktorsicherheitsforschung an der Hochschule Zittau/Görlitz
22.11.2001

Dr. R. Voskoboinikov (KI Moskau)
Potential Microstructural Mechanisms of the Radiation Embrittlement of Reactor Pressure Vessel Steels
07.12.2001

B. Böhmer
Reaktordosimetrie – Übersicht über aktuelle Ergebnisse und Probleme
19.12. 2001

Lecture courses

Lectures

Frank-Peter Weiß
Zuverlässigkeit und Sicherheit technischer Systeme
TU Dresden, Fakultät Maschinenwesen
SS 2000 und WS 2000

Udo Rindelhardt
Erneuerbare Energien I und II
Universität Leipzig, Fakultät für Physik und Geowissenschaften
SS 2000 und WS 2000

Departments of the Institute

Institute of Safety Research

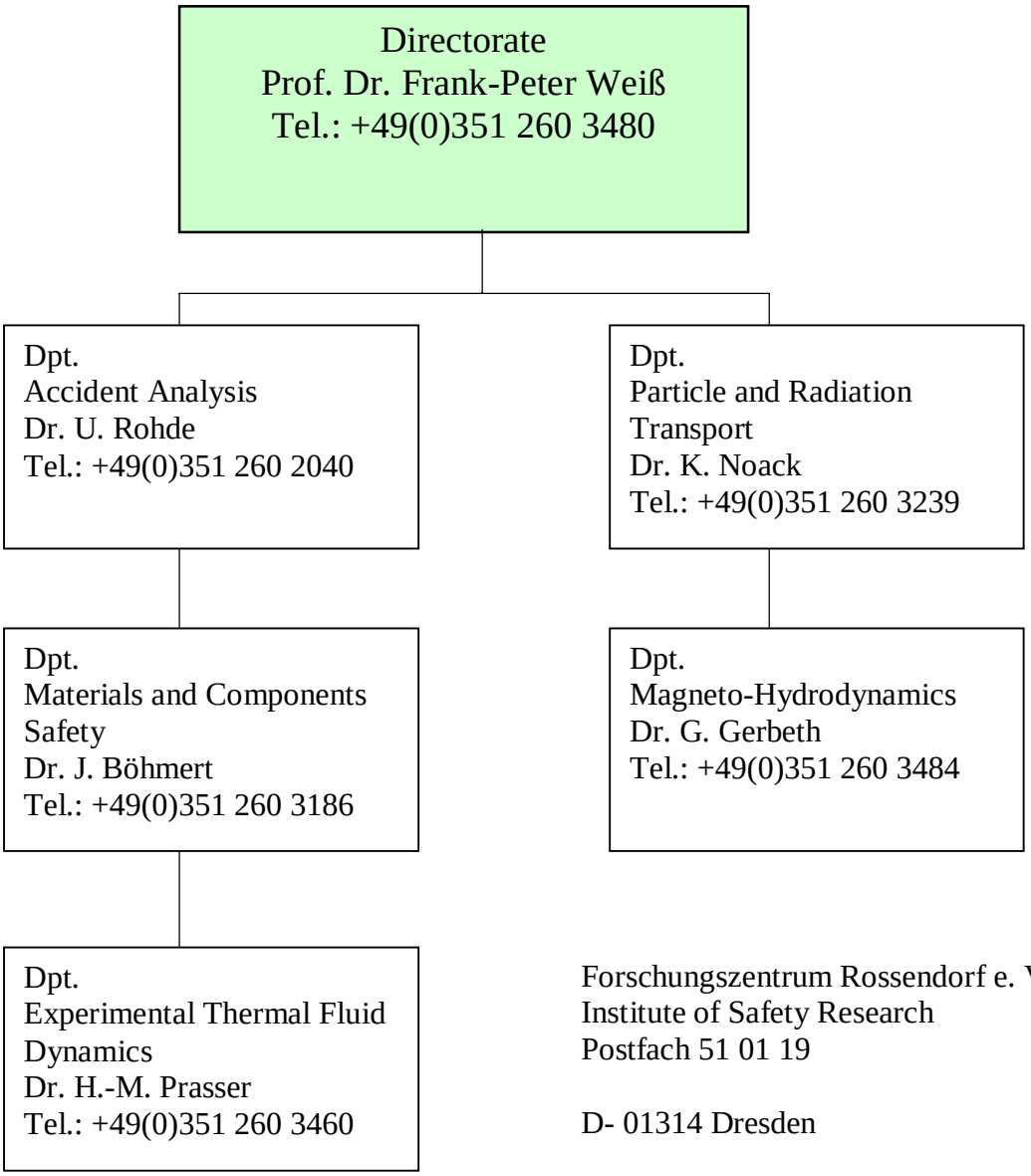

Forschungszentrum Rossendorf e. V.
Institute of Safety Research
Postfach 51 01 19

D- 01314 Dresden

Organigram / 30.01.2002

Personnel

Director: Prof. Dr. F.-P. Weiß

Scientific Staff

Altstadt, Eberhard Dr.
Beyer, Matthias
Böhmer, Bertram
Böhmert, Jürgen Dr.
Böttger, Arnd
Carl, Helmar Dr.
Cramer, Andreas Dr.
Eckert, Sven Dr.
Erlebach, Stephan
Fey, Uwe, Dr.
Fietz, Jürgen Dr.
Galindo, Vladimir Dr.
Gerbeth, Günter Dr.
Grants, Ilmars Dr.
Grundmann, Ulrich Dr.
Grunwald, Gerhard Dr.
Günther, Uwe Dr.
Hessel, Günter
Hoppe, Dietrich Dr.
Hüller, Jürgen Dr.
Kliem, Sören
Koch, Reinhard Dr.
Konheiser, Jörg
Krepper, Eckhard Dr.
Krüssenberg, Anne-Kathrin Dr.
Kryk, Holger Dr.
Küchler, Roland Dr.
Lindau, Bernd Dr.
Lucas, Dirk Dr.
Mittag, Siegfried Dr.
Müller, Gudrun, Dr.
Mutschke, Gerd
Neumann, Hartmut Dr.
Noack, Klaus Dr.
Prasser, Horst-Michael Dr.
Rindelhardt, Udo PD Dr.
Rohde, Ulrich Dr.
Schaffrath, Andreas Dr.
Schäfer, Frank Dr.
Schmitt, Wilfried Dr.
Schütz, Peter
Seidel, André
Stefani, Frank Dr
Stephan, Ingrid Dr.
Viehrig, Hans-Werner Dr.
Werner, Matthias Dr.
Willschütz, Hans-Georg
Witke, Willy
Zschau, Jochen Dr.
Zippe, Cornelius Dr.
Zippe, Winfried Dr.

PhD Students

Beckert, Carsten
Grahn, Alexander
Höhne, Thomas
Kern, Tommy
Kliem, Margarita
Ulbricht, Andreas
Weier, Tom

Technical Staff

Baldauf, Dieter
Behrens, Sieglinde
Bombis, Doris
Eichhorn, Christine
Forker, Klaus
Futterschneider, Hein
Gundrum, Thomas
Kunadt, Heiko
Leonhardt, Wolf-Dietrich
Leuner, Bernd
Losinski, Claudia
Mansel, Catrin
Nowak, Bernd
Opitz, Ruth
Otto, Gerlind
Pietzsch, Jens
Richter, Annett
Richter, Henry
Richter, Joachim
Richter, Petra
Rott, Sonja
Russig, Heiko
Schleßiger, Heike
Schneider, Gisela
Seidler, Christa
Seiler, Torsten
Skorupa, Ulrich
Tamme, Günther
Tamme, Marko
Webersinke, Steffen
Weiß, Rainer
Zimmermann, Wilfried